UNIVERSITY OF SOUTHAMPTON

Faculty of Engineering and Physical Sciences
Optoelectronics Research Centre

Development of PPLN waveguides for IR upconversion detection and imaging

DOI: https://doi.org/10.5258/SOTON/D3567

by

Noelia Palomar Davidson

MPhys with Nanotechnology

ORCiD: 0000-0002-6413-5858

A thesis for the degree of
Doctor of Philosophy

June 2025

University of Southampton

Abstract

Faculty of Engineering and Physical Sciences
Optoelectronics Research Centre

Doctor of Philosophy

Development of PPLN waveguides for IR upconversion detection and imaging

by Noelia Palomar Davidson

This thesis contains a series of experimental and numerical simulation work carried out for development of zinc-indiffused PPLN ridge waveguides at a range of wavelengths, spanning UV, visible and infrared light. First, the methodology for the characterisation and modelling of PPLN ridge waveguides is presented. The waveguides are fabricated via indiffusion of zinc into the crystal structure and ductile dicing, thus to create a good numerical model which will allow us to predict waveguide parameters for new wavelengths, an investigation of fabrication parameters is carried out.

Results for fabricated frequency doubling PPLN waveguides into the green/UV range are also presented. Preliminary results of the most efficient waveguides fabricated yielded a maximum conversion efficiency of 100.1%/W in a 20mm-long device, generating 532nm light, and in a different 20mm-long device, generating 378.3nm light with a 3.65%/W conversion efficiency. Experimental phasematching spectra and mode profile measurements are compared to those generated by the model. Numerical modelling of the effect of width variation along the length of the waveguide is carried out, as it is known to reduce efficiency.

Initial work towards building the existing model for MIR waveguides is presented. In optical experiments the fabricated MIR PPLN waveguides showed guidance up to 3.5µm in a 45µm wide ridge, and upconversion detection of pulsed 3.3µm light is achieved, generating 805nm light with a conversion efficiency of 0.11%.

An upconversion imaging system is built to demonstrate an application use for long wavelength zinc-indiffused PPLN waveguides developed during this thesis. The configuration uses Galvo mirrors to scan over an illuminated area, the collected light is coupled into a waveguide and upconverted to visible wavelengths for detection.

Contents

List of Figures

List of Tables

Declaration of Authorship

I declare that this thesis and the work presented in it is my own and has been generated by me as the result of my own original research.

I confirm that:

1. This work was done wholly or mainly while in candidature for a research degree at this University;
2. Where any part of this thesis has previously been submitted for a degree or any other qualification at this University or any other institution, this has been clearly stated;
3. Where I have consulted the published work of others, this is always clearly attributed;
4. Where I have quoted from the work of others, the source is always given. With the exception of such quotations, this thesis is entirely my own work;
5. I have acknowledged all main sources of help;
6. Where the thesis is based on work done by myself jointly with others, I have made clear exactly what was done by others and what I have contributed myself;
7. None of this work has been published before submission

Signed:..... Date:.....

Acknowledgements

Firstly, I would like to thank Prof. Peter Smith and Prof. Corin Gawith for offering me a position in this group and supporting me in this endeavour, I have thoroughly enjoyed working in the ORC. Meetings with Peter to talk about the project were always extensive but without exception you would leave with an invigorated love for science, having learned at least five new things. I could not have asked for a better supervisor than Corin, always making the time no matter how busy he was, and always knowing what to say to motivate me, his constant support has been invaluable in getting me here, I will be forever grateful.

To Dr. Alan Gray who mentored me when I first started, and while starting a PhD during a global pandemic was no easy feat, he provided an excellent example of what a researcher should be, which I still strive for to this day. I would also like to thank Dr. Paolo Mennea and Dr. Goronwy Tawy for their help in procuring results for this thesis. Specially to Paolo, who without his seemingly unending source of know-how and willingness to assist, the work within might've taken twice as long to complete.

I would also like to thank Covesion for providing the materials for experimentation, and Glenn Churchill for dicing all the waveguides. Thank you to our collaborators outside of the University, to DSTL for funding this project and organising excursions with my PhD cohort, after being a student, nothing is as exciting as your first paid-for trip. And Fraunhofer CAP, for being so welcoming and letting me join them in the lab to take important measurements for this work.

Thanks to my family, for always pushing and supporting me, and to my partner Tom, for always being there when I needed it.

"With age comes wisdom, but sometimes age comes alone"
- Oscar Wilde

Chapter 1

Introduction

Due to advancements in silicon sensor technology, imaging in the visible and near-infrared (NIR) region has become mainstream and commercially successful, driven by its use in mobile phone cameras and low light imaging systems. Exemplified by complementary metal-oxide semiconductor (CMOS) cameras, which now offer multi-megapixel resolutions at speeds up to 500fps with low read noise of $< 10e^{-}$. Beyond the range covered by mature CMOS technology, multiple sectors work in the eye-safe mid-infrared (MIR) wavelength range (2-8 µm), where they can benefit from low-loss atmospheric transmission windows for imaging, and location of fundamental absorption bands of many gas molecules for spectroscopy [1]. This results in a wide scope of applications; identification and quantization of gas and chemicals; non-invasive and non-destructive diagnostics tools [2]; environmental monitoring, such as gas leak detection; astronomy [3]; thermal imaging; and military defense applications [4]. Despite availability of direct detection across the infrared (IR) range, limitations posed by costly IR sensor technology, and lack of sensitive MIR detectors and imaging devices [5], means that the advantages of systems operating directly in these bands have not been fully exploited. Table 1.1 displays the approximate pricing of FLIR high-speed high-definition cameras with detection range between 1.5µm and 5µm.

TABLE 1.1: Guide pricing for FLIR InSb cameras for the MIR.

Resolution	Speed	Price
640x512 px	60 Hz	£55,000
	1 kHz	£95,000
1280x1024 px	60 Hz	£85,000
	1 kHz	£130,000

Upconversion is a nonlinear optical process that provides a method to parametrically convert photons to shorter wavelengths [6], where the photon energies are related as shown in Figure 1.1. These shorter wavelength photons can be detected directly with standard sensitive silicon detectors, circumventing drawbacks of MIR detectors. This approach has been around since the discovery of the first laser by Maiman in 1960 [7], the first demonstration being second harmonic generation (SHG) by Franken et al. in 1961 [8], although the term upconversion wasn't coined until the following year [9]. Parametric upconversion imaging was first demonstrated by Midwinter in 1968 [10], who was followed by several other research groups in producing an up-converted image from the IR to the vis/NIR range, as well as theoretical studies about the imaging technique [11, 12]. However, due to limiting factors such as available laser source quality and nonlinear crystals with poor upconversion efficiency, interest in the subject petered out until recently.

FIGURE 1.1: Geometry of frequency upconversion, a phenomena whereby a nonlinear material can convert input light with frequencies ω_1 and ω_2 to a different frequency ω_3, defined by $\omega_1 + \omega_2 = \omega_3$.

The key development that has led to a resurgence of interest in upconversion detection was the development of periodically poled materials by using electric field poling [13], where the increased conversion efficiency of the crystal has opened up the field to advancement. The University of Southampton is among the world leaders in

developing periodically poled materials for commercial applications, with the objective of further increasing the conversion efficiency by using a waveguide structure. Other academic research has worked towards improvements in spatial resolution, reduction of noise and lowering cost of operation, as well as imaging with undetected photons [14, 15, 16].

A primary use case for upconversion is to combine the advantages of MIR remote sensing with the availability and maturity of silicon detectors, offering a novel method for detection of IR signals and viewing of IR images. In particular, upconversion detection can provide advantages in applications that may require un-cooled detector operation, lower price, better signal-to-noise ratio, higher speed, or better resolution than that provided by IR sensors. Thus far it has been shown that detection of 3.2µm light using a nonlinear periodically poled lithium niobate (PPLN) crystal and un-cooled Si detector obtained an enhancement factor of 64 in the signal-to-noise ratio with respect to direct detection with InSb photodiodes [17].

1.1 Upconversion Imaging with Nonlinear Crystals

High quality imaging is a popular focus of upconversion research. In 2010 the first high-resolution (200×1000px) image was upconverted from the IR by Dam *et al.* [15] of DTU Fotonik using a PPKTP nonlinear optical crystal in an intracavity design. In their experiment incoherent 766 nm light was mixed with the intracavity 1342 nm Gaussian mode, generating 488 nm with an estimated quantum efficiency of $2{\cdot}10^{-4}$, defined as the product of conversion efficiency, detector quantum efficiency and filter transmission, which is approximately 3 orders of magnitude larger than earlier results with non-poled crystals [18], and suitable for detection with a cooled silicon CCD camera. They also theoretically demonstrated spatial resolution in upconverted images illuminated with incoherent light was better than for coherent [19], as high spatial frequency components of the images are upconverted more efficiently in the incoherent case.

The same group improved on this by building a field-deployable system for continuous wave (CW) image upconversion using a PPLN crystal in a low-loss cavity design, with a 20% conversion efficiency, attached directly to a charge-coupled device (CCD) camera [20]. The nonlinear crystal can be tuned to spectrally resolve images between 2.85 and 5µm, which are upconverted and captured by the CCD camera at ∼800nm, with a 200×100 resolution, seen in Figure 1.2a. These are multispectral images since the upconverted wavelength is dependent on the propagation angle inside the crystal. It can be thought as the image being formed of concentric rings, each upconverting a different wavelength. This is better seen by their demonstration of a monochromatic upconverted image, illuminated with a narrowband 3µm laser. The crystal is temperature tuned to upconvert 3µm at all propagation angles, and then stitched together to produce a full image, reproduced in Figure 1.2b. These experiments demonstrated the usefulness of nonlinear crystal for spectral imaging in the MIR, showing spectral decomposition of an image, as well as the ability to extract monochromatic image information, with the prospect of achieving hyper-spectral MIR imaging with high-quality visible light cameras.

In upconversion imaging, the field of view (FOV) of a system is limited by the length and aperture of the crystal. While increased interaction length in nonlinear crystals will lead to an increase in nonlinear conversion efficiency, it will also decrease the angular and spectral acceptance bandwidth [21] and, for imaging, these bandwidth dictate the FOV. In 2022, a chirped poled lithium niobate (CPLN) crystal was used in an upconversion imaging system by Huang *et al.* to enhance the field of view tenfold compared to a linear periodically poled crystal, giving a FOV of 28.2°, the largest to date without the need for post-processing [22], almost 3 times higher than previous FOV [23]. This approach facilitates high-speed imaging which is in demand for many applications. Broadband illumination sources have also been used to improve FOV [24], but offer worse conversion efficiency than using CPLN. The FOV when imaging with CPLN was found to be largely insensitive to temperature, and therefore robust, covering the MIR range of 2.7 to 5 µm without the need for

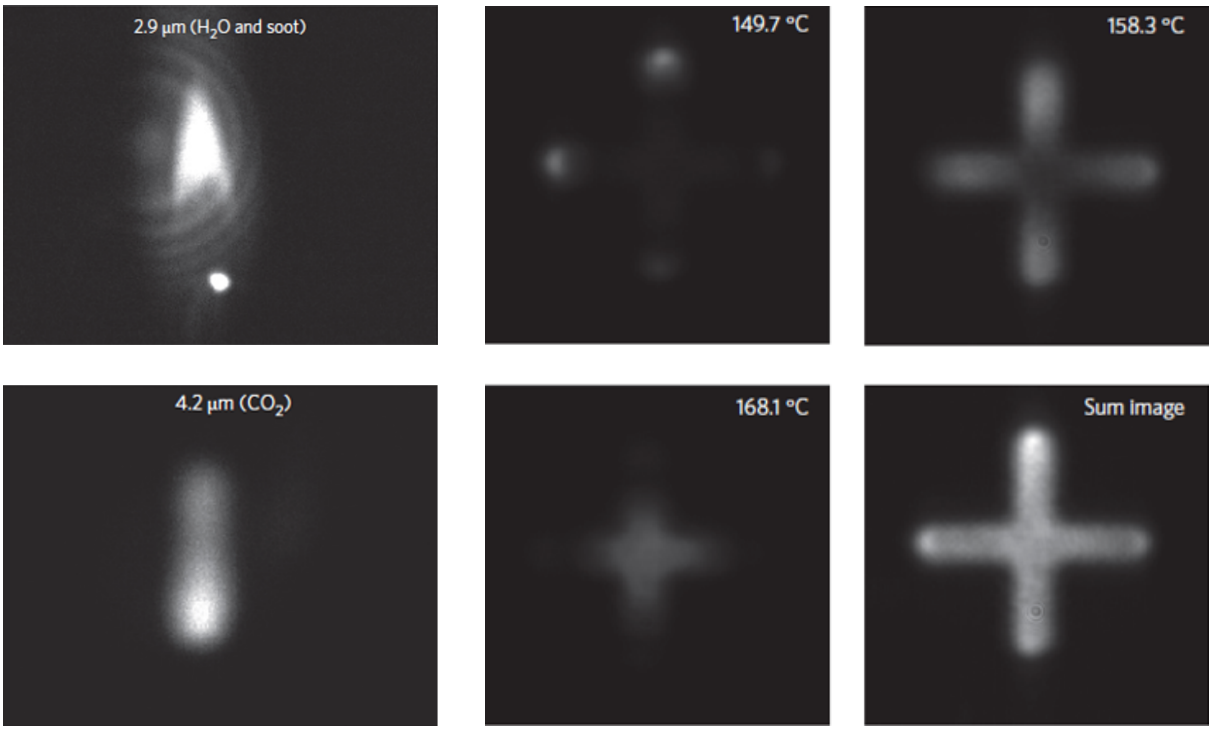

(A) (B)

FIGURE 1.2: Images reproduced from [20], (a) Spectral image of a candle at 800nm, upconverted from 2.9µm and 4.2µm using a PPLN nonlinear crystal, (b) a monochromatic image reconstructed by adding images at different temperatures, where the cross was illuminated by 3µm laser

tuning. The following year this wide FOV imaging configuration demonstrated a high-resolution (1024×1024 px) 3D MIR imaging system [25], where a 3D scene illuminated with 3.07µm pulsed light was upconverted to 771nm using a CPLN crystal, and recorded with an electron multiplying charge-coupled devices (EMCCD), able to discern a depth difference of 30 µm with a short 50ms exposure time, and achieving a 60µm spatial resolution. Extending the integration time to 2s allowed single-photon sensitivity, as well as for hyperspectral imaging at speeds of up to 10kHz [26].

In 2020 other implementations of upconversion imaging by Torregrosa *et al.* [27] introduced spatially modulated upconversion imaging with unpoled KTP in the context of freespace optical communications. This approach coded information in the 2D structure of an NIR beam, as shown in Figure 1.3. The 2D structure provides increased security against eavesdropping when compared to 1D modulation and in cases where

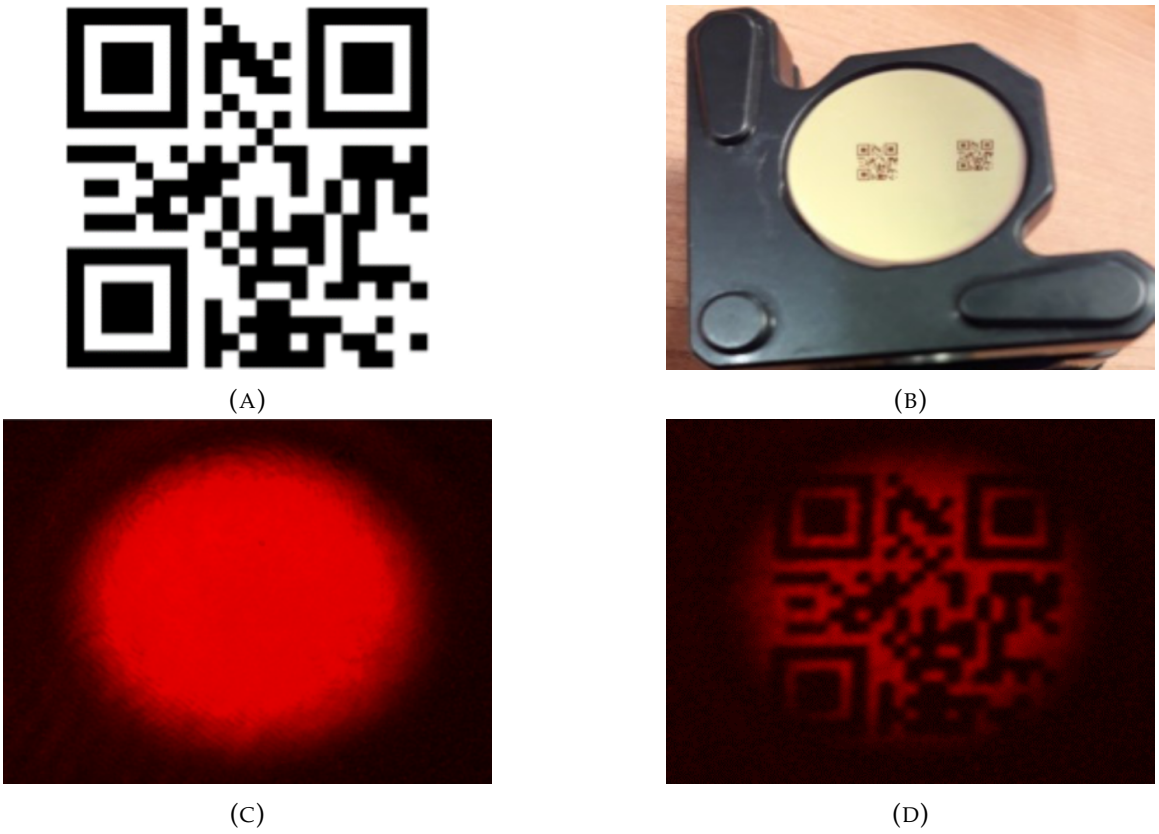

(A) (B)

(C) (D)

FIGURE 1.3: Images reproduced from [27], (a) QR data pattern used for spatial modulation, and (b) reflecting surface with printed 2D data. Upconverted beam images, (c) unmodulated, and (d) modulated and read out.

the speed of transmission is limited by the speed of the digital light modulator. Upconversion is not only useful for 2D spatial imaging, the fundamental process of the imaging technique involves nonlinear parametric frequency conversion, so the imaging is sensitive to both the temporal and spectral response of the object. Thus upconversion-based multi-dimensional imaging, where the other dimension could be wavelength, depth, phase or time becomes possible [4, 28, 29].

1.2 Single Photon Upconversion Detection

Parametric processes such as nonlinear frequency conversion involve interactions in which the spatial, temporal and spectral information of a signal can be conserved [4]. This means the process is inherently quantum in nature, and so the generated photons preserve quantum information such as photon statistics or coherence [30], making it an

ideal detector for quantum and low-light applications. Developing an upconversion approach that combines the benefits of parametric processes with high efficiency Si detectors for single photons will constitute an improvement over commercial MIR detectors, which suffer from relatively low detection efficiency (typically 20%) and high noise count rate of 10^4Hz [31].

The needs of quantum information science have pushed for frequency upconverted single photon detectors (SPDs) in the telecoms band. Waveguides offer a solution to scaling down increasingly complex systems and the requisite of integrating devices into fibre systems, this places nonlinear waveguides as a key platform in enabling quantum technologies [32]. Reverse-proton-exchanged (RPE) PPLN waveguides have been used as a means to increase the sensitivity of upconversion detectors [33, 34, 35]. One such PPLN-based detection system utilised a fiber taper for optimal mode-matching/coupling efficiency and demonstrated a system detection efficiency of 36% and noise count rate of 90 counts per second (cps), outperforming all reported 1550 nm band SPDs, other than superconducting based SPDs. These detectors can be used in a quantum key distribution (QKD) system to improve its performance, and extend the distance it can be transmitted over [36]. There is a significant impulse to move quantum optics to the MIR due to the possibilities opened up for quantum sensing, quantum communication and quantum imaging. In 2012 Dam *et al.* used PPLN in a low-loss cavity design to confirm the expected low upconversion noise levels and make the first non-cryogenic single photon mid-infrared camera, with a conversion efficiency of 20%, where the camera chip was cooled to -85°C. They show that upconversion is a low noise process, at 3 µm the dark noise added by the upconversion process was 0.2 photons/spatial element/second, which is well bellow cryogenically cooled InSb cameras, and is therefore comparable to high quality imaging devices for visible light [20]. Most recently, Huang *et al.* demonstrated a high-performance MIR photon counting and resolving frequency upconversion detector, based on a coincidence pumping configuration, using PPLN as their nonlinear crystal. They resolve photons at 3 µm with an overall conversion efficiency of 37% and a low noise equivalent power

(NEP) of $1.8{\cdot}10^{-17}$ W/Hz$^{1/2}$ thus representing the highest sensitivity among reported MIR detectors [37]. Using PPLN bonded on a silicon substrate in a ridge waveguide format for high index contrast, Lehmann et al. demonstrate a single-pass frequency upconversion system in the MIR for single-photon detection around 3.5µm. They obtain a detection efficiency of 0.4% and a NEP of $3.0{\cdot}10^{-15}$ W/Hz$^{1/2}$ [38]. This is the first instance of using PPLN waveguides for MIR single photon detection, they show a lower conversion efficiency than the resonant cavity and pulsed pump configurations above, but a similar NEP to the coincidence pumping configuration.

1.3 Nonlinear Waveguides as a Route to Upconversion of MIR Radiation

Nonlinear effects are inherently weaker than linear processes, prompting researchers to explore a variety of techniques for enhancing the efficiency of these interactions, such as using periodically poled crystals [39]. Researchers have exploited waveguide configurations in nonlinear crystals to maximize the nonlinear interaction for spectroscopic applications [40] and low-noise single-photon level detection [33]. The University of Southampton recently developed Zn-indiffused diced ridge waveguides for 1560nm and 780nm frequency doubling, with Watt-level power handling capabilities and high coupling and conversion efficiencies demonstrated for 1560nm SHG [41, 42, 43]. This is one of the highest reported in a waveguide of this type to date, with a crystal conversion efficiency of 74% and overall device efficiency of 58%. Taiwanese company HCP Photonics followed this with a similar PPLN waveguide format offering a crystal conversion efficiency of 73% and the overall conversion efficiency of 58%. Also at Southampton, Gray *et al.* demonstrated fast data transmission rates of an MIR wavelength using bulk PPLN and a silicon avalanche photodiode to detect the upconverted signal [44], which can be combined with our recent results with waveguides to increase conversion efficiency and can be applied to our areas of interest.

High laser intensities are essential for efficient frequency conversion, thus resistance to optical damage is an important factor when designing nonlinear waveguides. The foremost damage mechanism in nonlinear materials is photorefractive damage, where sufficiently high optical intensities cause charge accumulation in the crystal, distorting its refractive index and consequently the wavefront of the beam propagating in the material [45], limiting the optical power density it can handle. PPLN waveguides developed by our group offer low loss, can be optimised to give high coupling efficiencies and show improved resistance to photorefractive damage over other manufacturing methods, an effect by which the local refractive index of the crystal is modified by charge accumulation, distorting the wavefront of the propagating beam. Our links to Covesion, a University of Southampton spin-out company which makes PPLN waveguides, allow for the creation of PPLN that are spectrally matched to targets of interest, giving us flexibility to match the PPLN structure to wavelengths needed for given applications. Upconversion imaging in the MIR is one such application not previously done in the literature using waveguides. This topic provides an application context for most of the development in this thesis. In addition to that, swapping from continuous wave to pulsed sources would allow for time or range gated upconversion detection, to build up low-light level detection imaging systems. Other non-imaging applications would be for Raman specroscopy, quantum computing and ion trapping, are providing a push to develop our PPLN waveguides for their specific light-matter interactions.

The main focus of this work has been on building and developing a numerical model which aids in the design of Zn-indiffused PPLN waveguides optimised for different wavelength ranges. Prior literature describes the use of interference microscopy and prism coupling techniques in conjunction with inverse Wentzel–Kramers–Brillouin (IWKB) analysis to characterise refractive index profiles [46, 47]. This thesis lays out a more extended characterisation process, where the systematic investigation of parameters offers increased information about optimisation of waveguide structures. Previously at the University of Southampton conversion efficiency optimisation was carried

out by minimising mode field diameters of modes [43, 48], the model offers more insight into the effect of different parameters and allows to optimise for fibre overlaps as well as nonlinear overlap, and can help identify limitations in the waveguide fabrication process.

1.4 Summary

The contents of this thesis are laid out as follows; Chapter 2 will present the theory of nonlinear processes, with an explanation of the phasematching and choice of nonlinear crystal. Following the initial background theory, Chapter 3 will briefly outline the reasoning for choosing a waveguide structure, and fabrication process of our devices. This is followed by the methodology of different techniques used to characterise PPLN waveguides throughout this thesis.

Chapter 4 discusses numerical modelling of zinc-indiffused PPLN waveguides. The waveguide model is used to link the refractive index profile to the fabrication process. It is also utilised to study mode size and shape, to maximise coupling efficiency and nonlinear conversion efficiency. The results are employed throughout this thesis to tailor fabrication parameters for new nonlinear conversion waveguides.

Chapter 5 describes developing upconversion waveguides in the visible regime for 1^{st}-order 1064nm SHG and 3^{rd}-order 780nm SHG. Modelling results for the effect of the refractive index profile on the nonlinear overlap integral, single-mode operation and coupling efficiency to fibre are presented. Experimental results of the phasematching spectrum are compared to the modelled spectrum, and results for a reduction in ridge width variation are discussed. The power scaling operation of these waveguides are tested.

Chapter 6 introduces numerical modelling for MIR-supporting waveguides, alongside characterisation of the fabricated waveguides. Guidance up to 3.5 µm is found, upconversion results from MIR PPLN waveguides is presented. How to further increase the guidance of MIR waveguides with good conversion efficiencies is discussed.

Chapter 7 discusses the current state of MIR detectors, and presents a system for upconversion imaging using PPLN waveguides. The work contains the design and characterisation of an experimental scheme for upconversion from telecom to visible wavelengths in waveguides, as well as 1950nm to visible. A summary of the work presented and discussed in this thesis, and directions for future work are laid out in Chapter 8. This thesis provides the initial work undertaken to develop low SWAP (size, weight and power) MIR upconversion detectors, for applications such as imaging and Raman spectroscopy. This project is a CASE studentship sponsored by DSTL.

Chapter 2

Nonlinear Optics

2.1 Introduction to Nonlinear Optics

Nonlinear optics describes the optical properties of a material in the presence of sufficiently intense light. The nonlinear response of the material results in a broad range of effects, which have found applications in nearly all areas of science, from ultra fast switches for signal processing using materials with intensity-dependent refractive index [49], to molecular fingerprinting spectroscopy utilising frequency mixing processes to extend the range of a broadband coherent source [50]. This Chapter will focus on frequency conversion processes, these interactions allow for the generation of new wavelengths not previously available or difficult to achieve with existing laser media. The aim of this work is to enable high quality, established optical components for telecommunications to be exploited more widely towards MIR wavelengths and applications, by means of nonlinear optical materials.

2.2 Processes of Nonlinear Generation

In this section, the fundamental concepts of nonlinear interactions will be outlined, using the approach taken by Boyd [6] as a basis. Before defining the interactions between the input and generated wavelengths from a nonlinear interaction, we must look at how the spontaneous polarization of a material depends on the applied electric field strength, as defined in Equation 2.1,

$$P(t) = \epsilon_0[\chi^{(1)}E(t) + \chi^{(2)}E^2(t) + \chi^{(3)}E^3(t) + ...] \tag{2.1}$$

where ϵ_0 is the permittivity of free space, $\chi^{(1)}$ is the first-order nonlinear optical susceptibility, and $\chi^{(2)}$ and $\chi^{(3)}$ are the second- and third-order susceptibilities, respectively. It bears mention that this equation assumes polarisation at time t depends only on the instantaneous value of the electric field strength. This assumption implies that the medium is lossless and dispersionless. In general, the nonlinear susceptibilities depend on the frequencies of the applied fields, but for the purpose of outlining the nonlinear processes, under the present assumption of instantaneous response we can take them to be constants.

The physical processes that occur as a result of second-order polarization, $P^{(2)} = \epsilon_0\chi^{(2)}E^2(t)$, can only occur in non-centrosymmetric crystals, since the even power term prevents this relation holding true for crystals with inversion symmetry. Different processes arise as a result of third-order polarization, $P^{(3)} = \epsilon_0\chi^{(3)}E^3(t)$, which can occur both in centrosymmetric and non-centrosymmetric crystals. The work in this project, and therefore further analysis, is focused on second-order nonlinear processes.

If we consider an optical field made up of two distinct frequencies, ω_1 and ω_2, represented by the electric field shown in Equation 2.2 below, incident upon a second-order nonlinear optical medium, with an induced polarization response $P^{(2)} = \epsilon_0\chi^{(2)}E^2(t)$,

the nonlinear polarization will then be given by Equation 2.3.

$$E(t) = E_1 e^{-i\omega_1 t} + E_1^* e^{i\omega_1 t} + E_2 e^{-i\omega_2 t} + E_2^* e^{i\omega_2 t} \tag{2.2}$$

$$P^{(2)} = \epsilon_0 \chi^{(2)} [E_1^2 e^{-i2\omega_1 t} + E_2^2 e^{-i2\omega_2 t} + 2E_1 E_2 e^{-i(\omega_1+\omega_2)t} + 2E_1 E_2 e^{-i(\omega_1-\omega_2)t} + c.c.] + 2\epsilon_0 \chi^{(2)} [E_1 E_1^* + E_2 E_2^*] \tag{2.3}$$

where the expanded terms represent; second harmonic generation (SHG) for the first two terms, sum frequency generation (SFG) and difference frequency generation (DFG), for the third and fourth terms of Equation 2.3 respectively, and optical rectification (OR) for the last term. Each frequency term in the exponential coefficient corresponds to the output frequency of the respective nonlinear process, also shown schematically in the Figure 2.1 energy diagrams.

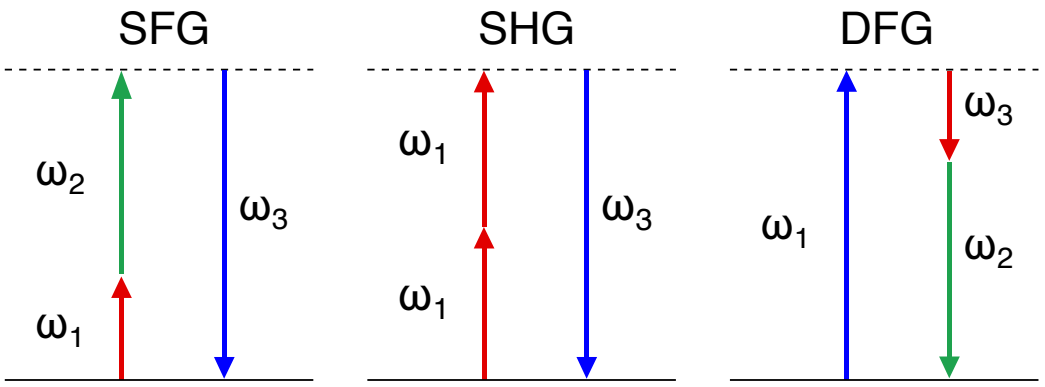

FIGURE 2.1: Energy conservation diagram of the SFG, SHG, DFG and OPA nonlinear processes. The upper dashed line represents a virtual energy level, which is not to be confused with an electronic transition of the photons. The photons are displayed to show the difference between DFG and an optical parametric amplification process.

In the literature it is common to see references to the nonlinear coefficient, d, when defining the strength of nonlinear processes. This is a third rank tensor with a relationship to susceptibility tensor $\chi^{(2)}_{ijk}$, as shown in Equation 2.4, where the indices represent Cartesian coordinates of the electric fields.

$$d_{ijk} = \frac{1}{2}\chi^{(2)}_{ijk} \tag{2.4}$$

It is possible to simplify this notation further by assuming that d_{ijk} is symmetric in its last two indices, giving d_{il} in Equation 2.5. This notation is used when the Kleinman symmetry condition is valid [51], which happens with interactions that involve frequencies much smaller than the lowest resonance frequency of the material, meaning the nonlinear susceptibility can be taken to be independent of frequency, and the interacting frequencies have permutation symmetry, as long as indices and frequencies are be permuted simultaneously.

$$d_{il} = \begin{bmatrix} d_{11} & d_{12} & d_{13} & d_{14} & d_{15} & d_{16} \\ d_{21} & d_{22} & d_{23} & d_{24} & d_{25} & d_{26} \\ d_{31} & d_{32} & d_{33} & d_{34} & d_{35} & d_{36} \end{bmatrix} \tag{2.5}$$

The magnitude of each d coefficient defines the strength of a nonlinear interaction, where the value depends on the material properties of the specific crystal used and its symmetries. The polarisation of the interacting and generated electric fields dictates which d coefficient can be accessed. This will be discussed in more detail in section 2.3, in regards to the specific crystal used for this project.

Returning to Equation 2.3, there are four different frequency components present, however, no more than one of these frequency components will usually be generated with any appreciable intensity by the nonlinear optical interaction. The reason for this behavior is that energy and momentum must be conserved in the optical field, meaning the nonlinear polarization can only efficiently produce an output signal if a certain phasematching condition is satisfied. Phasematching involves arranging the input and generated wavelengths to stay in phase as they travel through the crystal, enabling energy transfer. Operationally, one often chooses which frequency component will be radiated by selecting the polarization of the input radiation and, generally, the orientation of the nonlinear crystal [6], ensuring proper phase relationship between interacting waves.

The output signal of a nonlinear interaction is most efficiently produced if the phase-matching condition, the momentum difference between the photons, Δk = 0, is satisfied. Taking SFG ($\omega_3 = \omega_1 + \omega_2$) as an example, the momentum difference would be Equation 2.6, where the photon momentum vector is defined as in Equation 2.7, and refractive index can be calculated using the corresponding Sellmeier equation and coefficients.

$$\Delta k = k_1 + k_2 - k_3 \tag{2.6}$$

$$k_i = \frac{2\pi n_i}{\lambda_i} \tag{2.7}$$

If the $\Delta k = 0$ condition is met, the generated wave will maintain a fixed phase relation with respect to the pump signal, the individual atomic dipoles that constitute the material system will be in phase so that the field emitted by each dipole adds coherently in the forward direction. When $\Delta k = 0$ is not satisfied, the intensity of the emitted radiation is smaller than for the case of $\Delta k = 0$. The distance in the crystal over which this condition is met, or more explicitly, the distance for which the nonlinear process does not begin to transfer energy back into the input beam wavelength, is known as the coherence length.

$$L_{coh} = \frac{\pi}{\Delta k} \tag{2.8}$$

Longer coherence lengths will result in a higher generated intensity, as more energy has been transferred to the generated frequency. There are two widely known routes to phasematching the nonlinear process; critical and noncritical phasematching, based on the anisotropy and birefringence of a material. The differences will be addressed in the following sections of birefringence phasematching and quasi-phasematching (QPM).

2.2.1 Birefringent Phasematching

Birefringent phasematching is a type of critical phasematching, it requires careful angle tuning and beam propagation along multiple crystal axes. Birefringence refers to

the dependence of the refractive index on the polarisation of the beam, and its direction of propagation with respect to the principal crystal axis, as shown schematically in Figure 2.2. Not all crystals exhibit birefringence, this method can only be achieved by using extraordinary and ordinary polarized light as the input frequencies, which limits the types of interactions and the d coefficients it can access, affecting the conversion efficiency of the process and limiting the choices of crystal. Phasematching is accomplished by choosing a propagation direction at an angle to the principal axis of the material, such that the refractive indices encountered by the respective propagating beams mean they remain in phase as they propagate along the crystal.

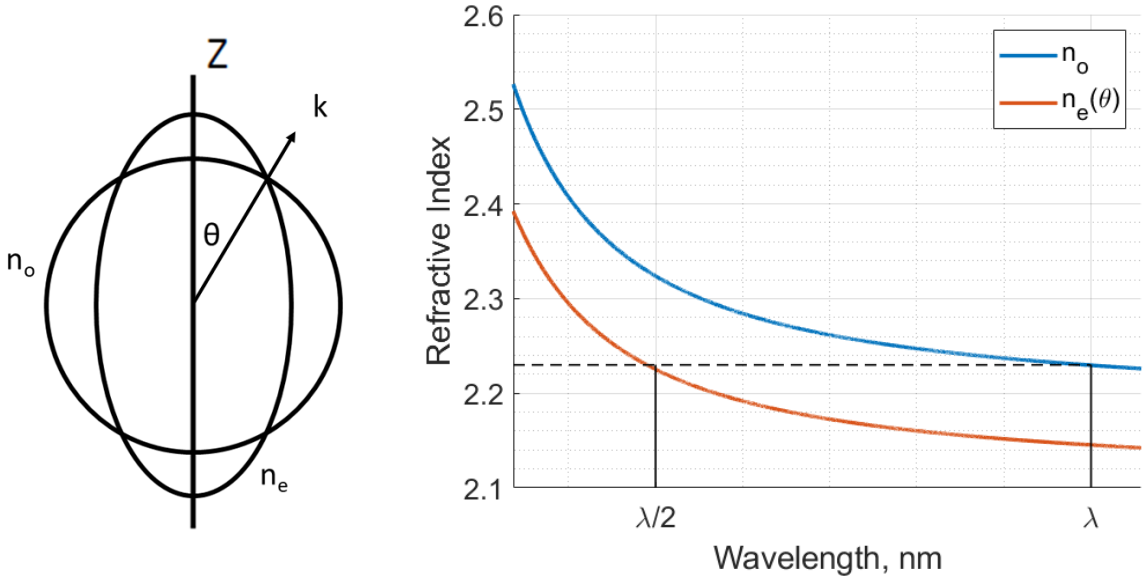

(A) (B)

FIGURE 2.2: a) Simplified refractive index birefringence ellipse, showing the dependence of the extraordinary index on angle to the principal crystal axis, b) dispersion diagram illustrating how a birefringent crystal can be phasematched for SHG, n_o=$n_e(\theta)$, where the θ is the angle to the principal axis of the crystal.

The resulting intensities from a phasematched and non-phasematched interaction are compared in Figure 2.3. Propagation along multiple axis means that the generated beam suffers from a phenomenon known as spatial walk-off; where the pump and upconverted beams propagate at different angles in the crystal, losing their spatial overlap. This phenomenon limits the length of crystal that can be used and also results in a higher M^2 of the generated beam. So while perfect phasematching for high nonlinear

intensities can be achieved, there can be drawbacks to using birefringent phasematching. Comparatively, in non-critical phasematching, input waves propagate along the principal axis of the nonlinear material, so spatial walk-off is avoided.

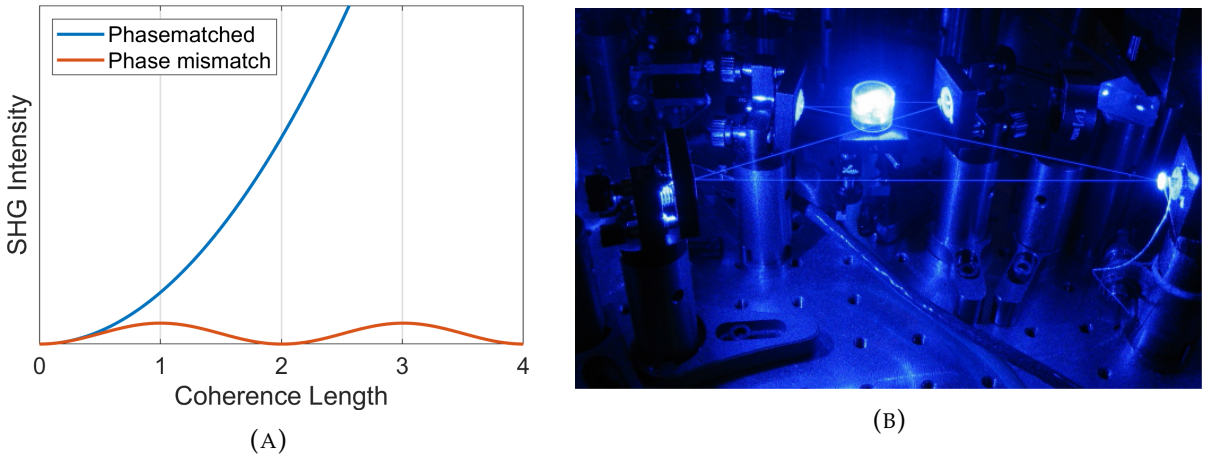

(A) (B)

FIGURE 2.3: a) Comparison of intensities of generated waves in a birefringent crystal, using the coupled-mode equations from Roussev *et al.* [33], b) photograph of a BBO crystal frequency doubling 461 nm blue light into the ultraviolet, reproduced from [52].

2.2.2 Quasi-phasematching

Quasi-phasematching (QPM) is a popular non-critical phasematching method that enables crystals with low birefringence to be tailored for wavelength conversion between specific wavelengths by periodic reversal of the crystal structure, and is less sensitive to angle alignment. The work in this thesis focuses on interactions in $\chi^{(2)}$ materials, a similar approach can be taken for $\chi^{(3)}$, etc.

Perfect phasematching does not occur with QPM, this method instead relies on correcting the momentum mismatch, Δk, between the two interacting beams. After the beams have travelled a certain distance within the crystal, known as the coherence length, they accumulate a π phase shift relative to one another. If there is no crystal domain reversal, the generated frequency must back-convert to the original input frequency due to energy conservation. The domain inversion period of the material is

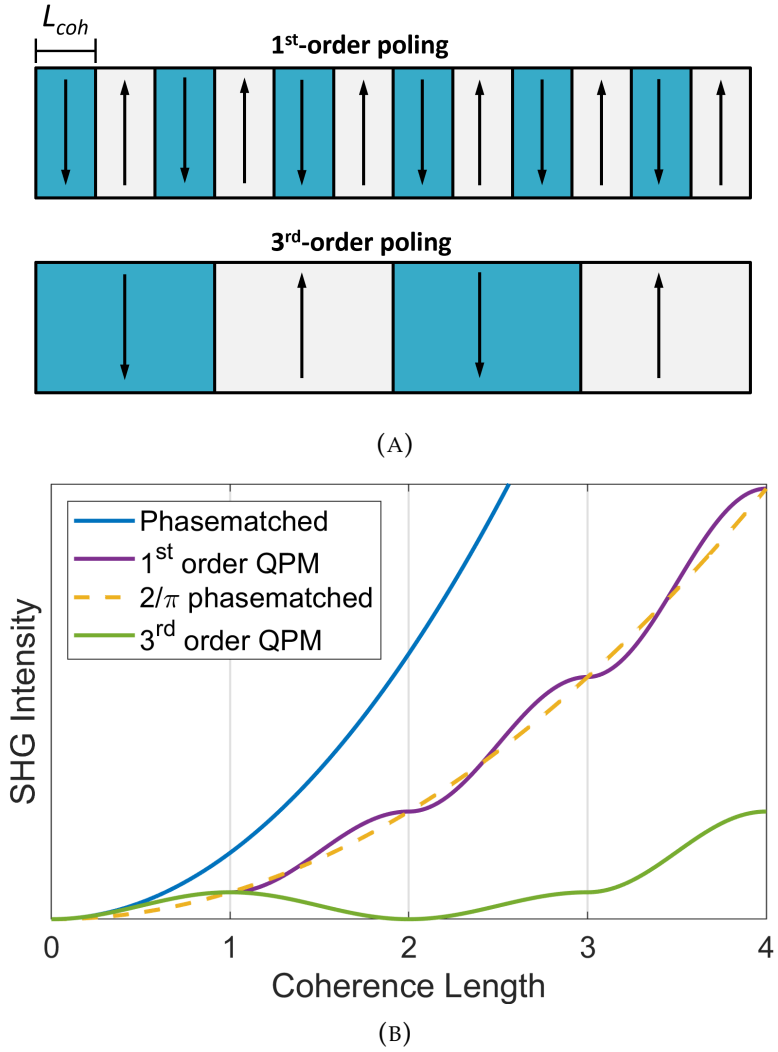

FIGURE 2.4: a) Periodic poling structures of a 1st-order and 3rd-order QPM grating, where the arrows represent the direction of the spontaneous polarisation of the crystal, b) comparison of generated wave intensities in a QPM nonlinear optical interaction, using the coupled-mode equations from Roussev *et al.* [33], for different order gratings.

proportional to the coherence length, and can be derived as Equation 2.9.

$$\Lambda = 2L_{\text{coh}} = 2\pi/(k_1 + k_2 - k_3) \tag{2.9}$$

Due to the noncentrosymmetric nature of $\chi^{(2)}$ materials, an inversion of the crystal structure will result in a change of the sign of the nonlinear coefficient, d. This periodically inversion of the crystal domain corrects the accumulated phase mismatch between the induced polarization and the propagating generated signal. Figure 2.4

shows different poling orders that used for QPM, and their corresponding relationship to SHG power generation, compared to perfect phasematching. The $2/\pi$ factor originates from the spatial modulation of the nonlinear coefficient.

Now the expected spectral curve for an SHG interaction in a QPM material will be calculated, using the same format as Boyd [6]. When solving the wave equation with the electric fields that describe a specific nonlinear optical interaction we get a set of coupled amplitude equations (Equation 2.10). Solving these coupled amplitude equations for low power, and knowing that intensity is directly proportional to amplitude, we get Equation 2.11, which is the characteristic SHG output sinc^2 curve of intensity against wavelength, as seen in Figure 2.5.

$$\begin{aligned}
\frac{dA_1}{dz} &= \frac{2i\, d_{\text{eff}}\, \omega_3^2}{k_1 c^2} A_3 A_2^* \exp\{-i\Delta k z\} \\
\frac{dA_2}{dz} &= \frac{2i\, d_{\text{eff}}\, \omega_3^2}{k_2 c^2} A_3 A_1^* \exp\{-i\Delta k z\} \\
\frac{dA_3}{dz} &= \frac{2i\, d_{\text{eff}}\, \omega_3^2}{k_3 c^2} A_1 A_2 \exp\{-i\Delta k z\}
\end{aligned} \tag{2.10}$$

$$I_3 \propto |A_3|^2 \propto L^2 \text{sinc}^2\left(\frac{\Delta k L}{2}\right) \tag{2.11}$$

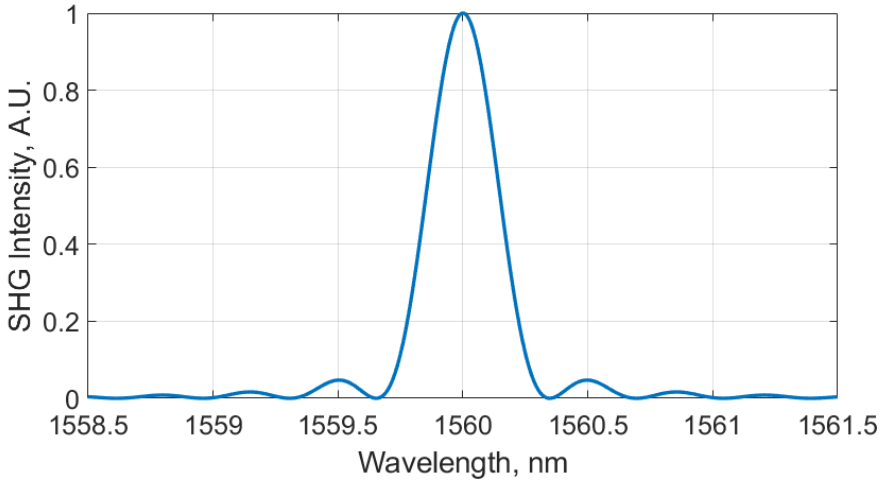

FIGURE 2.5: Characteristic sinc^2 curve in the vicinity of the optimal phasematching wavelength

Using QPM as a phasematching method gives a choice from a wider range of nonlinear crystals, as it is not dependent on birefringent properties of the crystal. The possible interaction polarizations are no longer limited for the input wavelengths, giving access to previously unavailable nonlinear coefficients, enabling a higher conversion efficiencies. The types of interactions based on the polarizations are displayed in Table 2.1. Furthermore, the phasematching period can be tailored to a chosen frequency conversion, and a convenient phasematching temperature, and the length is no longer limited by spatial walk off, as propagation direction is along crystal axis. Longer crystals will result in a larger output power but a narrower bandwidth, making it harder to phasematch experimentally. A comparison of several commonly used QPM materials is shown in Table 2.2.

	input	output
Type 0	ee	e
Type I	ee	o
Type II	eo	o

TABLE 2.1: Nomenclature for interaction types based on the phasematching polarizations for negative uniaxial crystals, such as PPLN

Type	λ range, nm	max d_{il}, pm/V	Pros & Cons
5% MgO:PPLN	350 - 5000	d_{33} = 25.0	Wide transmission window and high nonlinear coefficient, but requires doping to lower PRD
PPKTP	350 - 4500	d_{33} = 14.6	High power handling and good for large apertures, but lower nonlinear coefficient
PPLT	280 - 5000	d_{33} = 13.8	Transparent at lower wavelengths, but lower nonlinear coefficient
OP-GaAs	900 - 17000	d_{14}=170.0	Doesn't overlap with visible, but very high nonlinear coefficient and far-infrared transmission

TABLE 2.2: Comparison of popular QPM materials, and their nonlinear coefficients at 1064nm [53, 54].

For a thorough overview of QPM devices and historical progression, Hum and Fejer published a review paper [55], providing preliminary details on all aspects from other choice materials and the applications of different grating designs.

2.3 Periodically Poled Lithium Niobate

There are several factors to take into account when developing parametric devices for upconversion detection. PPLN is highly transparent from 350nm to 5µm [56], which is the range of interest for many molecule emission fingerprints, making it highly desirable for upconversion detection as it can be phasematched to required wavelengths in that range. Various teams around the world conduct research on the effect of doping LN crystals, investigating different methods and dopants that will yield favourable optical characteristics such as increasing photorefractive damage (PRD) resitance and an increased transparency region [57].

The transmission window of PPLN at low wavelengths can be lowered from approximately 350 nm to 320 nm by the introduction of magnesium into the crystal lattice. Magnesium has been shown to reduce PRD in the crystal by increasing the photoconductivity of the crystal [58], enabling higher power handling at visible wavelengths and reducing the temperature at which the crystal has to be operated at; undoped PPLN should be operated at $> 90^{\circ}$C to avoid photorefractive damage, which is considered too high for most commercial applications. All PPLN structures presented in this thesis are based on 5% magnesium doped lithium niobate (MgO:LN), whose dispersion profile is shown in Figure 2.6.

It's been shown by Xue *et al*. [60] that the optical properties of LN are determined by the Li-O and Nb-O bonds, with the long Li-O bond making up the greater contribution to the $\chi^{(2)}$ value. When introducing dopants, such as magnesium , they occupy the Li vacancy position in the lattice, changing the effective ionic charge and the lengths of the corresponding bonds. Second order nonlinear susceptibility decreases with increasing number of Li vacancies, in congruent lithium niobate as is used here, the concentration of Li vacancies is approximately constant for Mg doping levels up to 5%, resulting in an only slightly larger $\chi^{(2)}$ coefficient in Mg-doped lithium niobate.

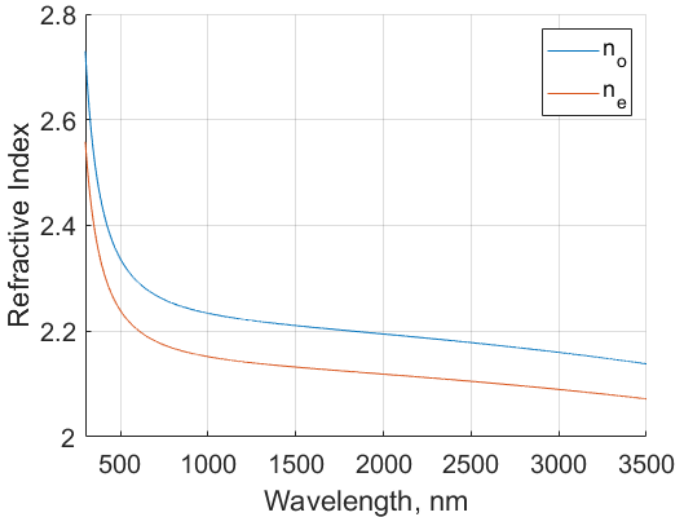

FIGURE 2.6: Calculated dispersion profiles of the extraordinary and ordinary refractive indices for 5% MgO:LN using Sellmeier coefficients from Gayer et al. [59]. As it is negative uniaxial crystal, $n_e < n_o$.

Taking what's been discussed in the previous section, the periods of several example SHG processes have been calculated for bulk crystals, using the Sellmeier equation and the coefficient values from Gayer [59], in Table 2.3.

$$n_{e/o} = a_1 b_1 f + \frac{a_2 + b_2 f}{\lambda^2 - (a_3 + b_3 f)} + \frac{a_4 + b_4 f}{\lambda^2 - a_5^2} - a_6 \lambda^2 \qquad (2.12)$$
$$f = (T - 24.5°\mathrm{C})(T + 570.82)$$

Pump Wavelength, nm	Λ, μm
3500	32.78
1560	19.67
1122	8.21
1064	6.97
780	2.44

TABLE 2.3: Calculated poling periods for phasematching Type-0 SHG, at several pump wavelengths of interest, for 5%MgO:PPLN crystals at room temperature, based on the Sellmeier coefficients from Gayer et al. [59] and Equation 2.9

For greater conversion efficiency in an interaction, a large nonlinear coefficient is ideal. In PPLN the largest nonlinear coefficient is d_{33}, which can be accessed when the polarisation of all 3 fields involved in the interaction are 'e' polarised. This corresponds to

vertically polarised light propagating along the length of a z-cut LN wafer. The nonlinear susceptibility matrix of lithium niobate is shown in Equation 2.13, where d_{22}=2.59 pV/m, d_{31}=4.4pV/m and d_{33}=25.0pV/m [54].

$$d_{il} = \begin{bmatrix} 0 & 0 & 0 & 0 & d_{31} & -d_{22} \\ -d_{22} & d_{22} & 0 & d_{31} & 0 & 0 \\ d_{31} & d_{31} & d_{33} & 0 & 0 & 0 \end{bmatrix} \tag{2.13}$$

$$P(\omega_3) = 4\epsilon_0 \, d_{\text{eff}} \, E(\omega_1) E(\omega_2) \tag{2.14}$$

For fixed propagation and polarization directions of the interacting electric fields, the nonlinear polarization's given by Equation 2.14, an expansion of the nonlinear susceptibility with respect to Equation 2.1. It can be seen that the value used to calculate the strength of an interaction is d_{eff} instead, which for QPM is equal to $\frac{2}{\pi} d_{il}$. The value has to be experimentally determined for the specific interaction, and has been previously been presented as d_{eff} = 14 pV/m for a 1560-780 nm Type-0 high power interaction in a PPLN waveguide via previous experiments at Southampton [61].

2.4 Waveguide Modes

An optical waveguide is a structure that confines the propagation direction of light in one or more dimensions. Light which is confined within the waveguide core is said to be guided, while there are different methods to achieve this, the most common technique which is used for the work contained herein, is to fabricate a structure consisting of a core and surrounding cladding such that $n_{core} > n_{clad}$. So long as light enters the core within a solid angle defined by the numerical aperture of the waveguide, when it reaches the core-cladding boundary layer its propagation will be restricted to the core through a process of total internal reflection.

The propagation of light within a medium is governed by Maxwells equations, the solutions of which relay information about the distribution of the electro-magnetic fields inside the waveguide structure. A solution to Maxwells equations is known as a mode and can be split into two groups, transverse-electric (TE) and transverse-magnetic (TM), corresponding to solutions in which either the electric or magnetic component of the wave is travelling perpendicular to the direction of wave propagation [62]. In reality a mode is rarely purely TE or TM, leading to the formulation of quasi-TE and quasi-TM modes, however typically the prefix is dropped for convenience. In particular we are interested in the wavevector, k_z, which for a wave propagating in the z direction, describes the propagation of light parallel to the direction of motion. This vector is most referred to as β whereby,

$$\beta = n_{eff}\mathbf{k}_0 \tag{2.15}$$

here $\mathbf{k}_o$ represents the free space wavevector $\mathbf{k} = 2\pi/\lambda$ and n_{eff} is the effective index of a mode. This parameter describes the equivalent index of refraction which would be required to match the propagation characteristics for a wave travelling purely in the z direction. Details on solutions of propagating modes in waveguides can be found in Ghatak [63] only a few specific cases exist where solutions can be found analytically. In the case of graded index waveguides, the complexity of the structure means numerical differential equation solvers must be used to find dispersion, group delay, or number of modes.

β may now substitute the photon momentum vector in the QPM equations when referring to waveguides. Including this in the mathematical derivation of nonlinear power generated in a waveguide in the low conversion efficiency regime and assuming negligible propagation loss, Equation 2.16 is obtained [39]

$$P(\omega_3) = \frac{8\pi^2 d_{eff}^2 \zeta_{OV}^2}{\lambda_1 \lambda_2 \epsilon_0 c n_{eff}^3} E(\omega_1) E(\omega_2) \tag{2.16}$$

where λ_i are the pump wavelengths, ϵ_0 is the permittivity of free space, c is the speed of light, n_{eff} is the effective index of each of the interacting wavelengths, d_{eff} is the effective nonlinear coefficient, and ζ_{OV} is the nonlinear overlap integral as given by Equation 2.17 [39],

$$\zeta_{OV} = \frac{\int\int_{-\infty}^{\infty} E_s(x,y)E_p^2(x,y)\,dx\,dy}{\left[\int\int_{-\infty}^{\infty} E_s^2(x,y)\,dx\,dy\right]^{\frac{1}{2}} \int\int_{-\infty}^{\infty} E_p^2(x,y)\,dx\,dy} \tag{2.17}$$

where E_s and E_p are the electric field distributions of the SHG and pump waveguide modes respectively, and is discussed more in depth in Chapter 5.

2.5 Summary

Chapter 2 delves into the physics of nonlinear optics, outlining different processes induced by second-order nonlinear polarization in materials. The chapter explains the role of phase matching in achieving efficient nonlinear interactions, comparing birefringent phase matching and QPM. While birefringent phase matching involves angle tuning within anisotropic crystals, QPM leverages periodically poled structures to align phases over extended interaction lengths, enhancing efficiency. PPLN is presented as our choice of material due to its high d_{33} coefficient and resistance to photorefractive damage. Waveguide modes are briefly discussed. This theoretical framework forms the basis for understanding the waveguide designs and applications discussed in later chapters.

Chapter 3

Periodically-Poled Lithium Niobate Waveguides

3.1 Why waveguides?

Expanding on Chapter 2, waveguide mode analysis tells us that better modal confinement will result in an improved overlap integral between two wavelength modes. Comparing focused bulk interactions to waveguide interactions, the latter overlap for a longer length, thus they have increased longitudinal spatial confinement, resulting in better conversion efficiencies and greater upconverted intensity [39]. In a waveguiding regime, propagating light will have an effective refractive index, or modal index, which differs from the bulk crystal index such that $n_{core} < n_{eff} < n_{clad}$, therefore the poling period required to meet phasematching conditions in waveguides will differ from the bulk crystal phasematching condition. The effective index depends primarily on wavelength, the mode in which the light propagates, waveguide architecture and the temperature of the crystal. This makes it impractical to solve an effective index analytically, relying instead on numerical simulations. A primary aim of this work is to populate a theoretical model of Zn-indiffused PPLN ridge waveguides and poling periods optimised for specific interactions from short visible wavelengths up to the MIR, by

(A) (B) (C) (D)

FIGURE 3.1: An illustration of approximate mode area for different structures typically found in PPLN, from weakest to strongest modal confinement, (a) bulk PPLN, $\sim$1mm^2, (b) metal indiffused PPLN, $\sim$100µm^2, (c) PPLN ridge waveguide, $\sim$10µm^2, and (d) thin film lithium niobate on insulator, $<$1µm^2

methodical investigation of the link between fabrication parameters and refractive index profiles. This work uses mode profiling in addition to prism coupling techniques, which are the standard in prior literature, to characterise refractive index profiles. Furthermore, comparison between optical characterisation and modelled phasematching spectra are used to corroborate these findings, and identify discrepancies which will enable us to further refine the waveguide model.

There are several types of waveguide structures, shown in Figure 3.1, one of the first demonstrated PPLN three-dimensional waveguides was titanium indiffusion in the 1970's [64]. The diffusion of Ti into LN from a deposited metal layer was thoroughly studied in early days [65, 66, 67]. Titanium replaces vacant Li and Nb sites in the crystal matrix, which results in increased sensitivity to photorefractive damage for wavelengths up to 900nm, and damage to the periodic poling, offering low efficiencies of $\sim$1%W^{-1} [68, 69].

In the 1980's proton-exchange (PE) was proposed as another method to introduce a refractive index change for LN waveguides [70]. This involved the substitution of lithium ions with H^+, a proton, by bringing the surface of LN into contact with a molten acid. This resulted in a high index change at the surface of the material in the extraordinary polarisation, and a small refractive index decrease in the ordinary polarisation, and an improved immunity to optical damage when compared with Ti:$LiNbO_3$ waveguides [71]. However, when using highly acidic melts the nonlinear coefficient decreased and the poling domains degraded. Waveguides can be annealed to diffuse

the proton layer further into the LN and recover the nonlinear coefficient, but the poling degradation cannot be reversed by this method [72]. To circumvent this, a so called 'soft proton exchange' approach was adopted, which involves a low-acidic melt, with planar waveguides showing an efficiency of 210%W^{-1} for DFG of ∼1.6µm [73]. Even greater efficiencies have been shown using reverse-proton exchange (RPE) waveguides, where lithium is re-introduced to the upper surface of the LN, gradually reducing the refractive index change there. This pushes the guided modes away from the damaged poling region, as well as improving the overlap between modes because of the more symmetrical Gaussian-like refractive index profile. Ultraprecision machining for ridge-type waveguides was first proposed and presented by Kawaguchi [74, 75] to counteract the limitations on efficiency imposed by RPE waveguides caused by dispersion in the crystal. Such RPE ridge waveguides have achieved an efficiency of 510%W^{-1} in 1550nm SHG for pump powers below 100mW [76].

When co-doping, each impurity entering the lattice will contribute to the structural state of the crystal. The method of doping affects the distortions that occur in the structure, which can either increase the efficiency of the second-order nonlinear coefficient or reduce it [77]. Zinc indiffusion creates a positive refractive index change for both extraordinary and ordinary polarised light [78], allowing for Type 0, 1 and 2 interactions in the crystal presented in Chapter 2, as opposed to using annealed proton-exchanged (APE) waveguides which only support TM modes and are therefore limited to Type-0 interactions. Zinc is chosen for the waveguide indiffusion process as it increases the resistance of PPLN to photorefractive damage [78], and indiffuses at a lower temperature than titanium, reducing degradation of the poling periods. The magnitude of the refractive index change achieved via zinc indiffusion has been measured to be smaller in TE than in TM in waveguides [79]. Ridge waveguides typically offer an even better overlapping of the confined fields for different wavelengths and a better stability at high pump power compared to Ti-indiffused or reverse proton exchange waveguides, as well as channel waveguides [38, 80, 43].

The methods outlined so far form gradient-index waveguides, to achieve higher index contrast a lithium niobate crystal can be bonded to a lower index substrate, such as lithium tantale (LN) or silica (SiO_2), to form a waveguide which retains the properties of bulk LN. This method, known as lithium niobate on insulator (LNOI), paired with ridges offers very high confinement. In the last few years thin-film lithim niobate (TFLN) has become commercially available, where the thickness of LN is typically under 1µm, offering high conversion efficiencies of $416\%W^{-1}$ in a 4mm long device [81], useful for on-chip integrated photonics platforms for single-photon detection.

Zinc-indiffused PPLN ridge waveguides are a recently developed technology from the University of Southampton [43, 41, 82]. We have demonstrated world-leading watt-level efficiency performance, and licensed PPLN waveguides to the Southampton spin-out company, Covesion Ltd., to commercialise this work. To date, the main focus of PPLN waveguide development has been 1560 to 780nm SHG for quantum applications with Rb atom traps [83]. This is now been a well established market with reliable devices produced by Covesion in a ruggedized package format. Thus, a major goal of this PhD was to explore new wavelength ranges and applications for PPLN waveguides, aiming to cover the transparency range of lithium niobate. PPLN waveguides for SHG of common wavelengths around 1µm (1064nm, 1122nm) and 780nm are currently of interest as a route to addressing atom- and ion-specific interaction wavelengths in the visible, and the groundwork of developing waveguides for this application will be laid out in this Chapter. The development of MIR supporting waveguides for use in upconversion imaging systems will build upon the work carried out in this Chapter, and the feedback from optical characterisation.

Part of the work performed in this project was to test the performance and operating parameters of prototype PPLN waveguides, such as operating wavelength, temperature bandwidth, mode profiles and conversion efficiency, and use this as a basis for designing novel light sources for use in experiments. This Chapter introduces the optical test approaches used throughout this thesis for the analysis of different stages of

Zn-indiffused PPLN ridge waveguide fabrication and optimisation. It highlights the advantages of waveguides for enhancing nonlinear interactions and details the fabrication process to create the waveguides used in this work.

3.2 Fabrication of PPLN waveguides

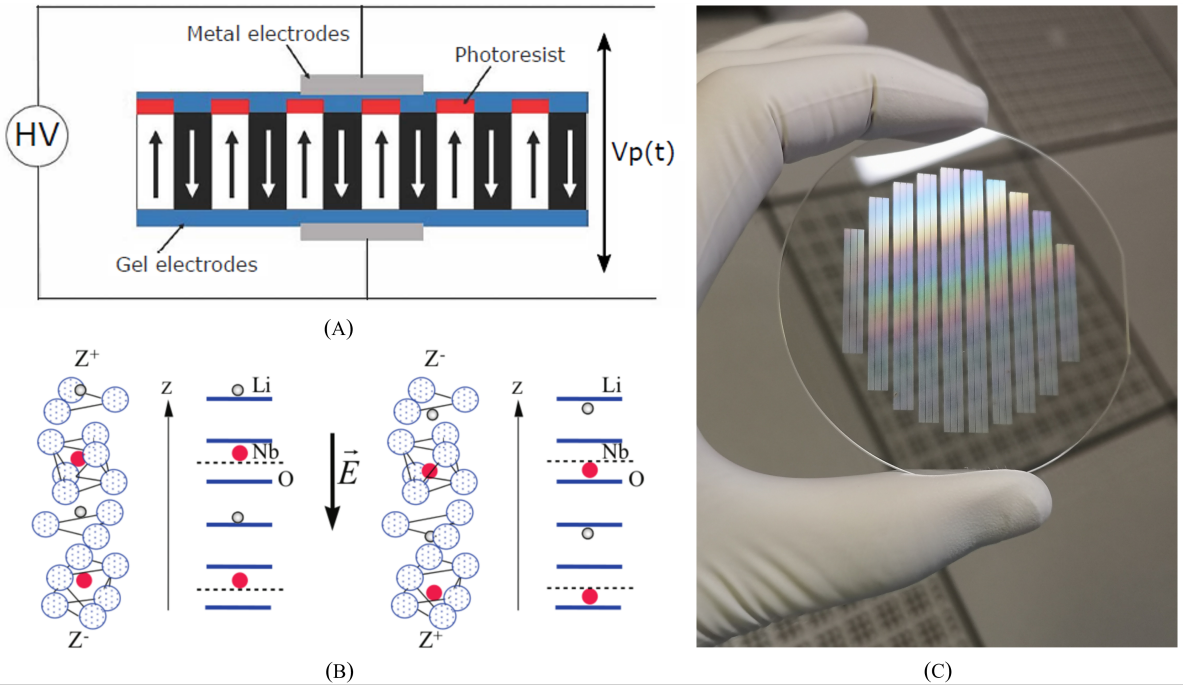

FIGURE 3.2: (a) Poling technique developed at Southampton for the patterning and domain inversion of the PPLN devices used in this work. (b) Crystalline structure of lithium niobate, displaying the locations of the Li and Nb atoms before (left) and after (right) an electric field is applied to invert the direction of the spontaneous polarisation. Image reproduced from [32]. (c) Photograph of a LN wafer, with periods in the 4µm range, after the periodic poling process.

Fabrication of the periodically poled lithium niobate devices used in this work is performed in several steps, as detailed in [84]. In summary, to create a periodic grating in the crystal a patterned photoresist is applied to the wafer, conductive gel and metal electrodes are then added to create a circuit, as detailed in Figure 3.2a. A series of high voltage pulses are then applied to induce nucleation, followed by a steady voltage to grow the inverted domains, such that they are oriented with respect to the applied electric field, resulting in the crystal structure seen in Figure 3.2b. After this step, the

photoresist is removed and the QPM crystal wafer is ready for the waveguide fabrication process.

The waveguide fabrication process used for devices described in this thesis is based on zinc indiffusion and ultra-precision dicing of ridge waveguides, as outlined in [43]. The PPLN wafer is cleaned and metallic zinc is deposited with an OPT Plasmalab 400 Sputtering Machine to a desired thickness. The wafers are then transferred to a furnace and indiffused in an oxygen environment at high temperatures between 900^{o}C and 1000^{o}C for an hour to create a planar guiding layer. Ridge waveguides and end facets are diced into the crystal with a Disco DAD3430 machine, with ultra-precision ductile dicing enabling waveguide and facet definition [85]. The steps of the process and an image of example waveguides are provided in Figure 3.3.

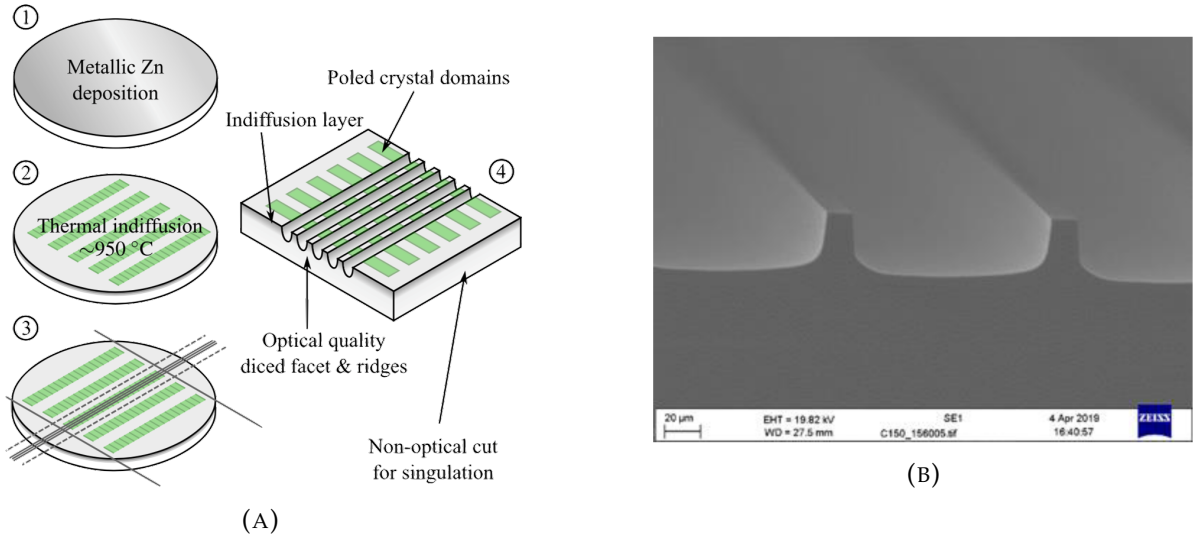

FIGURE 3.3: a) Fabrication process for the diced ridge PPLN waveguides, developed at the University of Southampton, reproduced from [42] b) SEM image of a ridge waveguide structure and facet, after dicing, in 5%MgO:PPLN. Image courtesy of Dr. Alan Gray.

3.3 Optical Characterisation

This section presents the methodology of optical measurements for characterisation of PPLN waveguides in this thesis. Through analysis at different stages of fabrication,

we enable feedback and optimisation of waveguide outcome. These results will be used to build a theoretical model predicting the modal propagation and phasematching characteristics of zinc-indiffused PPLN waveguides under different wavelengths and modes of operation, introduced in the next Chapter, to corroborate findings with theory and design future waveguides. With the exception of the bulk phasematching, the methodologies outlined here will use a standard 1560nm SHG device, already optimised for upconversion.

3.3.1 Bulk PPLN Phasematching

In order to test the optical characteristics of bulk and waveguide PPLN devices against the theory presented in the previous Chapter, a basic SHG phasematching characterisation setup was used, as illustrated in Figure 3.4.

For initial experiments, a 1064nm SHG PPLN crystal (MSHG1064-1.0-10) from Covesion was chosen, as it is off-the-shelf and generates green light, making it easy to operate and characterise by new users. The PPLN crystal is held in a fixed oven whose temperature can be controlled, ranging from 20 to 200^{o}C. An IPG Photonics 1064.5 nm laser beam was focused into the 6.9 µm period grating of the 10 mm long PPLN crystal. To maximise SHG output, the focusing conditions laid out by Boyd and Kleinman [86] were followed; the focus should be at the middle of the crystal, and the value of the focusing parameter, $\xi = l/b = 2.84$. The focusing parameter is the ratio of the optical path length of the crystal and the confocal parameter b, where

$$b/2 = z_R = \frac{n\pi w_o^2}{\lambda}$$

and z_R is the Rayleigh length of a beam, the distance from the focus at which the beam's waist increases by a factor of $\sqrt{2}$. Optimal spot radius was calculated to be w_0 = 16.7 µm, however, a 200 mm focal length lens was chosen due to availability, giving a spot size of 30µm.

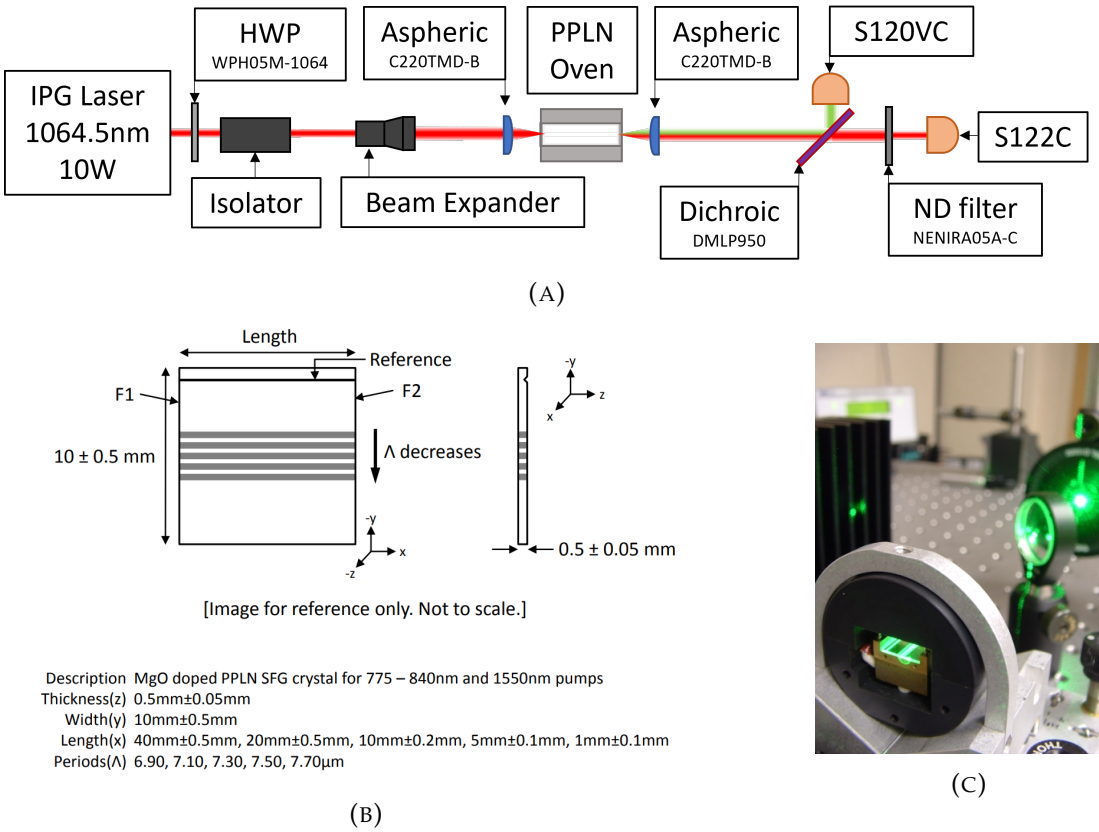

FIGURE 3.4: Optical characterisation of 1064nm SHG in a bulk PPLN crystal; a) experimental setup for measuring SHG of 1064nm in a bulk PPLN crystal, b) schematic and specifications of Covesion standard bulk PPLN crystals phasematched for 1064nm SHG, and c) photograph of green light generation in a PPLN crystal, image courtesy of Covesion.

The temperature of the oven containing the PPLN crystal is varied, scanned over a range set by the previously developed theoretical equations of the phasematching conditions, Equation 2.11. The pump and SHG output are collimated by a secondary lens. The temperature sweep was carried out for a range of increasing pump powers, and both the throughput pump power at 1064.5 nm and SHG output power at 532 nm were recorded. From the results presented in Figure 3.5, the phasematching curve follows a sinc^2 shape as expected, with smaller side lobes which are indicative of a focused interaction, as shown by Boyd and Kleinman [86]. From the recorded data the device efficiency, η, was calculated to be 3% W^{-1}, and a normalised conversion efficiency of 3% $W^{-1}cm^{-2}$, where $\eta = \dfrac{P_{shg}}{P_{pump}^2 L^2}$ and P_{pump} is measured after the crystal. This is in the order of magnitude that bulk nonlinear interactions are expected.

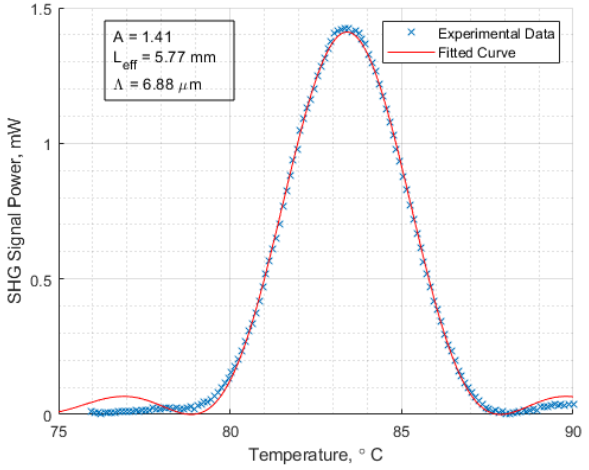

(A)

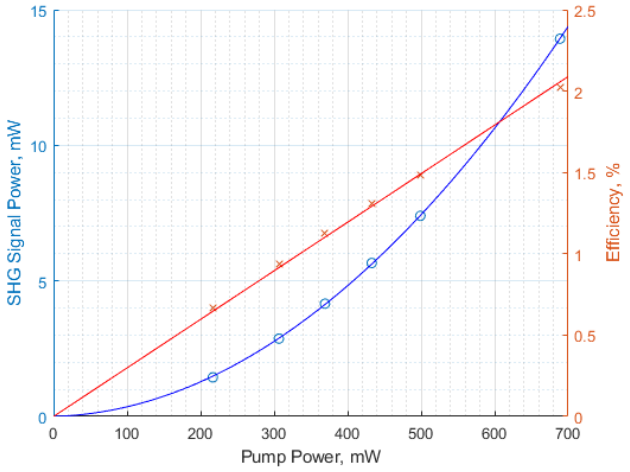

(B)

FIGURE 3.5: Bulk PPLN crystal result plots; a) phasematching spectra fitted with a sinc^2 function, and b) second harmonic generation, and efficiency of the interaction, as a function of pump power.

3.3.2 Secondary-Ion Mass Spectrometry

Secondary-ion mass spectrometry (SIMS) is a powerful tool that has been used extensively to study the diffusion behaviour of titanium into $LiNbO_3$ [67]. Early studies of zinc diffusion into $LiNbO_3$ were mainly worked on by Lifante *et al.* [87, 88, 79] using similar techniques to the ones presented here. SIMS analysis works by focusing an ion beam onto the surface of the sample in high vacuum, and then collecting and analysing the composition of ejected secondary ions. The ejected secondary ions undergo mass-to-charge ratio analysis, resulting in a mass spectrum containing detailed

surface chemical information. Resolution of SIMS analysis decreases for increasingly larger depths due to the higher beam energies needed to reach depths in the 10µm+ region, resulting in ion mixing, as well as uneveness in the crater depth, both which will affect decrease the resolution from angstroms to tens on nanometres.

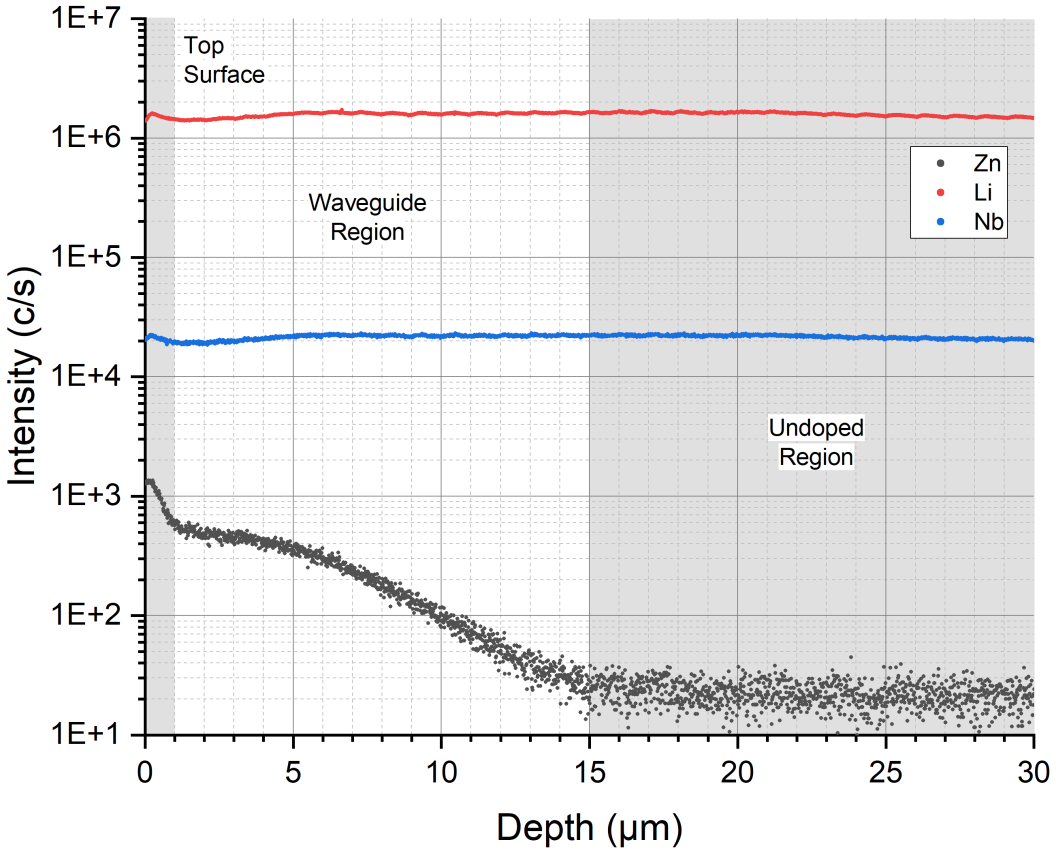

FIGURE 3.6: Depth profiles for Zn, Li and Nb ions obtained by SIMS from a standard Zn indiffused 5%MgO:LN wafer for 1560nm SHG, as measured by Fraunhofer IPM.

Figure 3.6 shows the yield of Zn, Li and Nb ions detected by SIMS of a sample prepared using the approach described in Section 3.2 from a 1560nm SHG Zn-indiffused waveguide, 100nm of zinc indiffused at 950°C. A clear peak in the Zn concentration can be observed in the top 1µm of the sample, along with smaller peaks in the Li and Nb concentration. A similar peak was observed by Lifante in Zn-vapour diffused LN [87], and by Caccavale in Ti diffused LN [89], which indicates a small amount of outdiffusion from the crystal surface, a common phenomenon when heating the crystal.

To produce low-loss waveguides it is crucial that the surface quality not be degraded by the diffusion process. Depending on the fabrication conditions, Li-Zn-O compounds can form on the surface region, if its formation is energetically preferable to vaporization of ZnO [79]. The peak could also indicate that the initially deposited layer of Zn might not have been fully depleted. However, the shape of the indiffusion depth profile is best fit with a Gaussian, which implies a completely exhausted source, rather than an error function-like shape from an undepleted source [90]. This suggests that zinc diffusion works under different diffusive regimes. Based on this information, a Gaussian shape was chosen for the numerical modelling of the refractive index profile and numerical simulation of waveguide modes presented in the following Chapters.

Studies on the effect of zinc concentration on the refractive index of LN and MgO:LN have demonstrated that there is an index increase in both polarisations, where the change is greater for the extraordinary polarisation [78, 88]. The aim of indiffusing zinc into 5% MgO:PPLN is to produce low-loss optical waveguides that will guide both polarizations and display high resistance to photorefractive damage. Cation dopants with valence states $\leq$2, such as Mg^{+2}, reduce the photorefractive damage, while cation dopants with valence states $\geq$3, such as Nd^{+3} and Ti^{+4}, increase the photorefractive damage. Doping LN with both Zn^{+2} and Mg^{+2} showed higher resistance to photorefractive damage than PE and Ti-indiffused waveguides [46].

3.3.3 Prism Coupling

Prism coupling is a method employed to calculate refractive indices of bulk materials and thin films, as well as film thickness, with a high accuracy and resolution over a large range of wavelengths. Its ability in linking refractive index change to known dopant concentrations making it a useful tool for constructing refractive index profiles. Figure 3.7 shows the basis for how light is coupled into the sample. A rotating stage scans through the well-defined angles at which the laser beam impinges on the prism-sample boundary. When the total internal reflection criterion is violated, there is a

resulting intensity drop on the photodetector, indicating that the beam has coupled into the optical propagation modes of the sample. The effective index of the mode, β = n·sin(θ), is then retrieved by Snell's law $n_1 \sin(\theta_1) = n_2 \sin(\theta_2)$, as both the index of the prism and the incident angle are well known, and the β value is preserved when a ray of light is refracted at the boundary of two media.

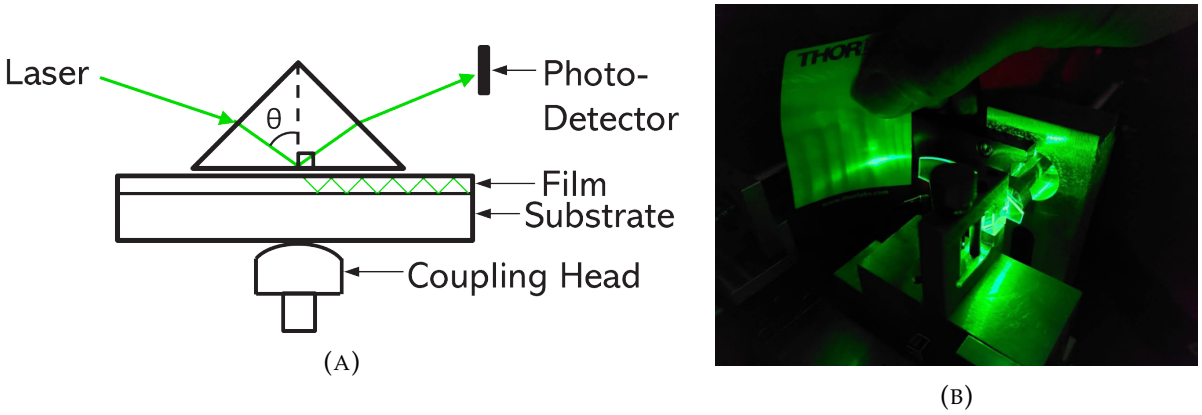

(A) (B)

FIGURE 3.7: (a) Prism coupling technique, used by the Metricon Model 2010, to measure the effective refractive index of a mode, (b) picture of the Metricon system with a supported mode.

A MgO:PPLN wafer refractive index was measured before indiffusion, and compared to the theoretical values of Sellmeier equations by Zelmon [91], shown in Figure 3.8. While the percentage difference in values is seemingly small, it has to be taken into consideration that the absolute error is in the order of $\pm 1 \cdot 10^{-4}$, which is the same order of magnitude as the refractive index difference being investigated. This error is proportionally larger for TM modes since they have a lower refractive index. Due to this, and a known variation in the bulk refractive index value of MgO:PPLN wafers arising via standard growth conditions, in the order of 10^{-3}, affecting the effective index and phasematching wavelength of the starting material, an effort was made to measure the bulk refractive index of each wafer for comparison with any zinc indiffusion related change.

The Metricon Model 2010 system used for this work has the capability to calculate the profile for a graded index waveguide [92], but will be avoided in favour of using FIMMWAVE (Photon Design Ltd.), introduced in the next Chapter, to create a profile

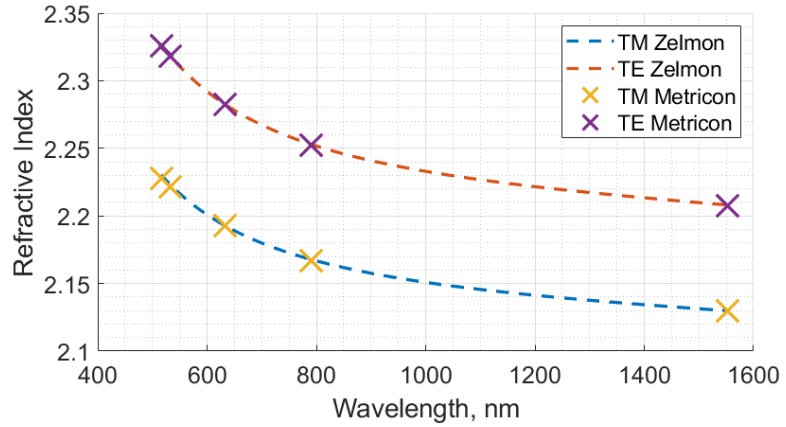

(A)

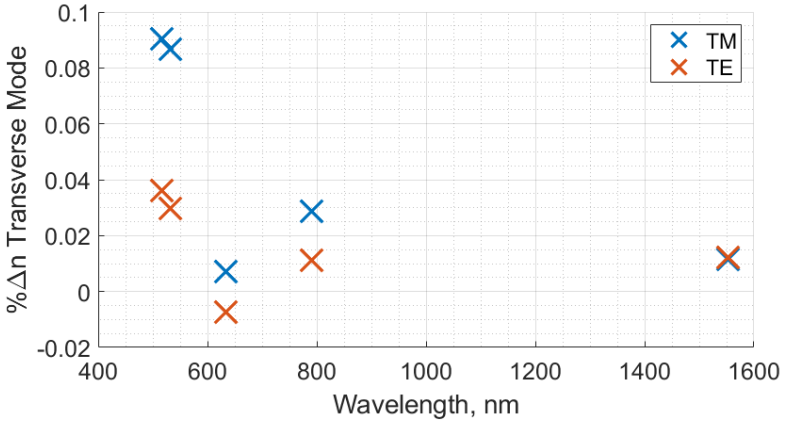

(B)

FIGURE 3.8: a) Dispersion profile based on Sellmeier equation and coefficients from Zelmon et al. [91], compared the refractive index measured by the Metricon, both for 5%MgO:LN, and b) the percentage difference between the Zelmon model and measured refractive index values.

which will match the effective index values measured, as it gives more consistent results by choosing the refractive index profile shape. Prism coupling measurements are taken using un-diced pieces of Zn indiffused wafers. After the chip singulation process, the wafer tops are polished to remove any ZnO residue from the surface, and ensure good contact between the wafer and prism surfaces. To measure the refractive index change arising from the zinc-indiffusion process, the effective indices at 532nm of the three supported planar modes found for each wafer are measured for several different Zn thicknesses, and plotted in Figure 3.9. The purpose of this is to monitor process reproducibility, analyse how different fabrication parameters of zinc thickness, deposition power and indiffusion temperature affect the planar modes, and

consequently how we can change these to achieve a desired refractive index change. In general, increasing Zn thickness has shown to increase the effective refractive index of the modes.

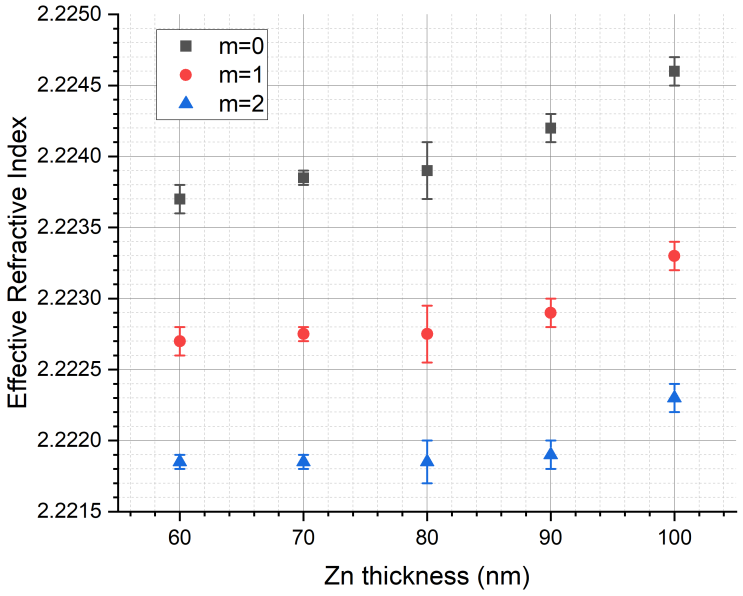

FIGURE 3.9: Effective indices for the three TM modes measured at 532nm with the Metricon, for a wafer with several different Zn thicknesses, indiffused at 950°C.

3.3.4 Mode Profiling

Optimising the size and shape of propagating modes is an important step in the development of PPLN waveguides, both when maximising coupling efficiency to a fibre for packaging and commercialisation purposes, and for maximising model overlap to increase efficiency of the frequency conversion processes. The mode shape is defined by the refractive index profile and width of the ridge waveguide, and was investigated by measuring mode field diameters (MFD) at pump wavelengths. This enables comparison to a numerical model to tailor the desired optical waveguides. The MFD in this work are measured with an optical characterisation setup developed by Dr. Rex Bannerman [93], presented in Figure 3.10. The system uses fibre butt-couple launch and a high resolution InGaAs CCD camera (Raptor, Owl 640) to capture the intensity profile

of a beam for a series of calibrated steps from the waveguide facet. The profiles of the beam are fitted via second-moment analysis [94] to evaluate the vertical and horizontal MFD at each step. Further analysis of the diverging beam enables the calculation of a waveguide's numerical aperture (NA).

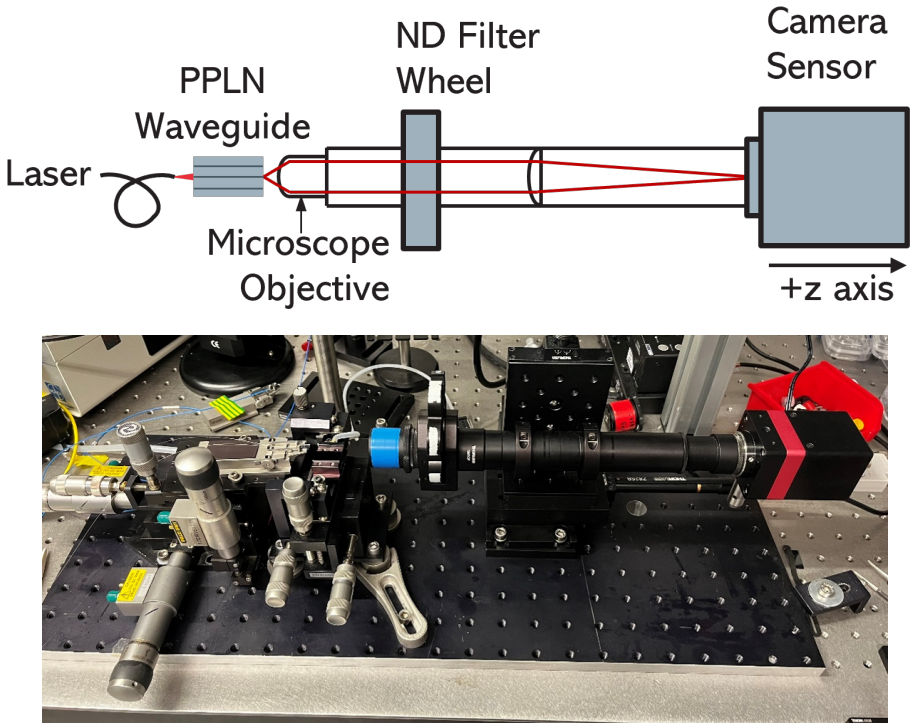

FIGURE 3.10: Schematic diagram and photo of the optical system used for measuring mode profiles of the zinc-indiffused PPLN waveguides presented in this work.

Figure 3.11 displays mode profiling measurements for the fundamental TM mode in a typical 1560nm SHG Zn-indiffused waveguide made at Southampton as discussed in [43], and fitting done by the software to calculate NA and MFD values. The vertical and horizontal MFD values are displayed for several nominal waveguide widths. Nominal ridge widths are those programmed into the dicing saw, which can deviate slightly from the resulting actual ridge widths that are cut into the substrate, as implied by the larger X MFD value for the nominally 12µm wide waveguide when compared to the 12.5µm wide waveguide. When fabricating waveguides for a particular nonlinear interaction, several ridges for varying widths are typically prepared in each device to account for this small (<0.5 µm) dicing saw step deviation. Horizontal MFD increases with waveguide ridge width and shows little dependence on refractive index change

or diffusion depth, whereas vertical MFD is mainly determined by the refractive index profile parameters, increasing slightly as ridges become narrow enough to make the waveguide single mode. This beam profiling method yields MFD standard deviations in the order of 10^{-4}.

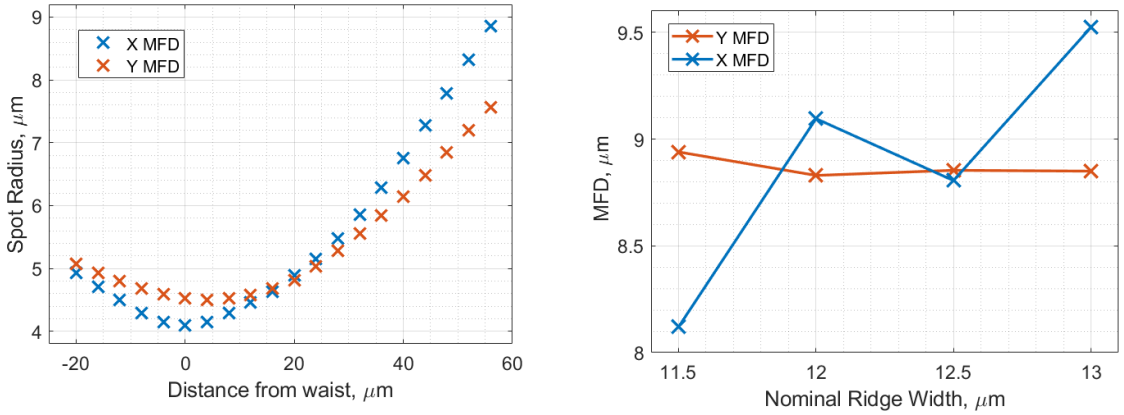

(A) (B)

FIGURE 3.11: (a) Spot size of the beam measured by the optical characterisation system at a series of steps from the waveguide facet, and (b) vertical and horizontal mode profile measurements at 1550nm for waveguides with nominal ridge widths of 11.5 to 13µm, indiffused with 100nm of Zn at 950^{o}C.

3.3.5 PPLN Waveguide Characterisation

In order to test the nonlinear characteristics of the Zn-indiffused PPLN waveguides, a test setup was built with a similar configuration to that performed in Section 3.3.1, using a PPLN waveguide designed for 1560-780 nm SHG, supplied by Covesion Ltd. This will form the basis for optimising waveguide design and tailoring waveguide properties for different wavelength ranges, requiring experimental validation of simulations, as well as demonstrating functionality for targeted applications.

A free-space fibre-launch system is used for characterisation, as it allows for careful optimisation of launch position and spot size adjustment, offering flexibility to maximise coupling efficiency into different waveguides. For 1560nm operation an Agilent tunable seed laser was injected into an erbium-doped fibre amplifier (EDFA) to pump 1550-1560 nm light into the Zn-indiffused ridge waveguide. The laser was coupled into

a 12µm wide 40 mm long waveguide ridge, with an 18.3 µm period grating, located in an oven, as shown in Figure 3.12. The input beam was shaped via a fibre zoom collimator and C-coated ashperic lens, to give a 9µm spot size to the waveguide mode and maximise coupling efficiency. Rather than the middle of the crystal, like in bulk crystal phasematching, the spot is focused to the input facet of the waveguide. The pump and SHG output are collimated by a secondary lens, where both the pump launch and collimating lens are mounted on six-axis manual stages for fine control. The temperature and wavelength ranges were chosen based on earlier published work on PPLN waveguides [41, 42, 43].

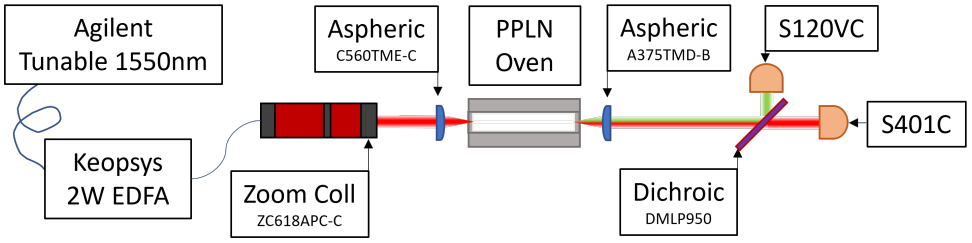

(A)

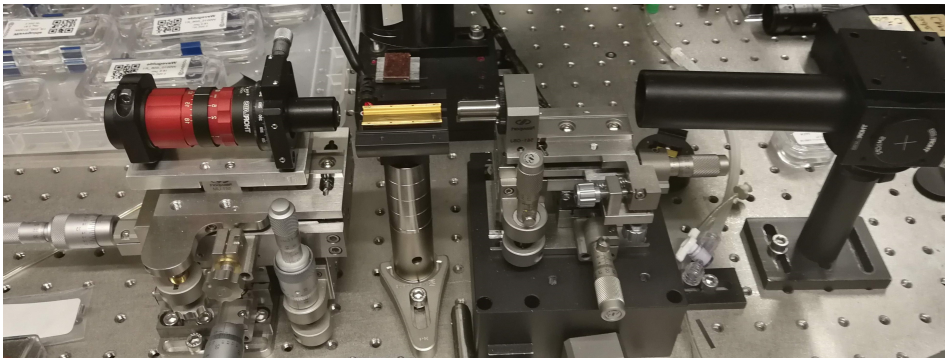

(B)

FIGURE 3.12: Optical characterisation setup for measuring SHG of 1550nm in a PPLN waveguide; (a) scheme of the experimental setup, (b) photograph of waveguide characterisation setup

The phasematching spectrum of the waveguide was recorded at different temperatures, Figure 3.13 shows how phasematching wavelength increases with temperature, following the expected trend. Comparatively, the phasematching temperature of a bulk crystal corresponding to a period of 18.3 µm, calculated using the Sellmeier equations in Gayer [59], would be $\sim$ 340°C. Then SHG was recorded at a constant temperature for increasing pump power, shown in Figure 3.13, and giving a calculated

device efficiency η of 1.5% W^{-1} cm^{-2}, where $\eta = \frac{P_{shg}}{P_{pump}^2 L^2}$ and a normalised conversion efficiency of 24% W^{-1}, where P_{pump} is measured after the crystal. This is an order of magnitude larger than the calculated normalised conversion efficiency for a bulk interaction.

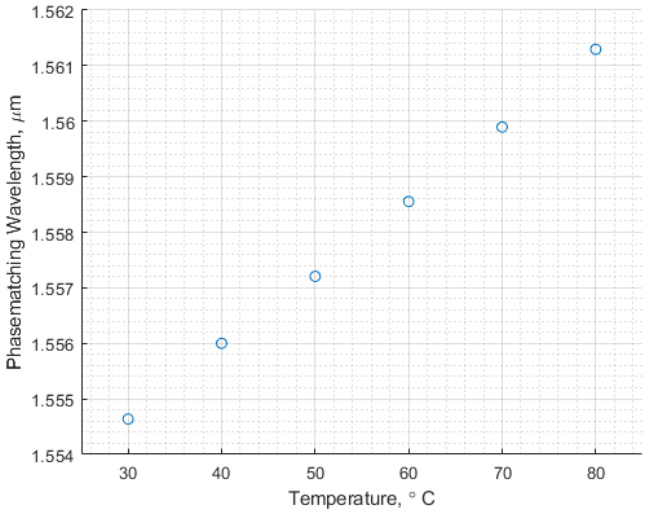

(A)

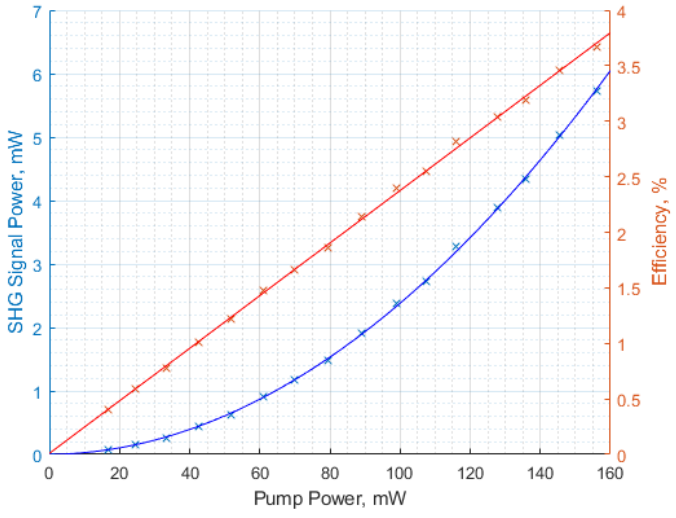

(B)

FIGURE 3.13: Characterisation data plots of a Zn-indiffused 12µm ridge PPLN waveguide for 1560nm SHG; a) graph showing the effect of temperature on the phasematching condition, and b) SHG power and efficiency of the interaction, as a function of pump power.

This result is smaller than the one presented by Berry [42] using a similar regime, likely due to less well optimised coupling efficiency, and no anti-reflection (AR) coating on the waveguide facets. The efficiency of SHG in a waveguide is defined as in Equation

3.1, where ζ_{OV} is the overlap integral between the input and generated modes.

$$P_3 = \frac{8\pi d_{eff}^2 \zeta_{OV}^2}{\lambda_1^2 \epsilon_0 c n_{eff}^3} P_1^2(z=0) L^2 = \eta P_1^2 L^2 \tag{3.1}$$

Following these results, pump power was increased to 2W, the maximum allowed by the EDFA, and a wavelength and temperature sweep were carried out in this regime, as shown in Figure 3.14.

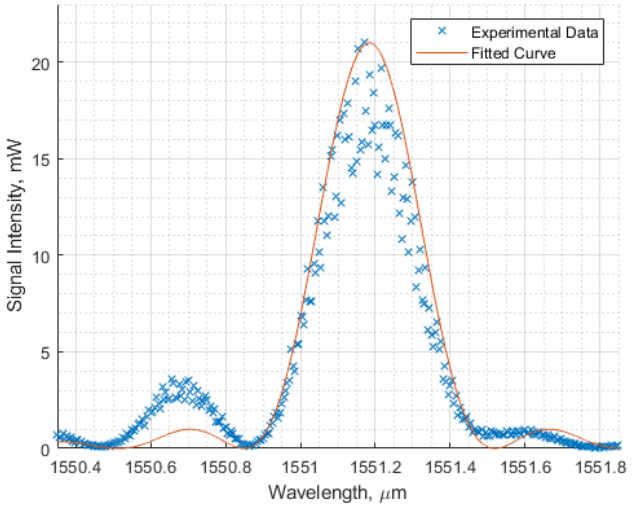

(A)

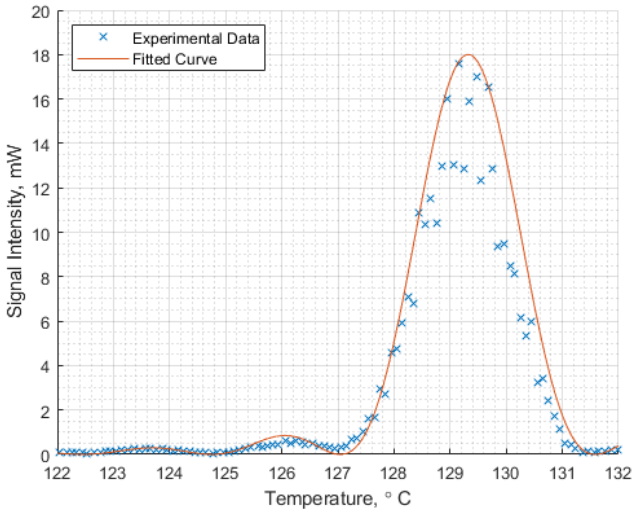

(B)

FIGURE 3.14: Characterisation data plots of Zn-indiffused 12μm ridge PPLN waveguide for 1560nm SHG; a) wavelength tuned phasematching spectra fitted with a sinc^2 function, b) temperature tuned phasematching spectra fitted with a sinc^2 function.

The noise in the data is attributed to the formation of a Fabry-Pérot cavity inside the waveguide, due to the lack of an anti-reflective coating and angle-cut facets of the waveguide with reduce Fresnel reflections. The data has been fitted using bulk refractive indices, alongside a suitable period to centre the data. Comparing the performance of bulk crystals against waveguides, the latter have been demonstrated to be better in terms of conversion efficiency, however they are more difficult to fabricate, with many addition steps that need to be optimised. The focus of the following work in this thesis is developing a model and simulations that will enable PPLN waveguides to be designed and fabricated for a wider range of wavelength interactions, and experimental characterisation of these novel waveguides to verify and iteratively develop the model through various generations. Discussion of the model design and features is included in Chapter 4.

3.4 Summary

Chapter 3 focuses on the development of PPLN waveguides, highlighting their ability to enhance nonlinear conversion efficiency versus standard bulk crystals. The fabrication process used for the PPLN waveguides designed and investigated in this thesis is described, snd key characterization techniques, such as secondary-ion mass spectrometry (SIMS), prism coupling, and mode profiling, are introduced to evaluate the refractive index profiles, effective indices, and mode confinement of the waveguides. These insights provide a foundation for optimizing waveguide design and performance in subsequent chapters.

Chapter 4

Modelling of Zn-indiffused PPLN Waveguides

As stated previously, for a few simple, specific structures like step-index waveguides or fibres, application of Maxwell's equation has produced rigorous solutions to the wave equation in the waveguide. For waveguides with graded indices the equations become complicated to solve, so one must resort to solving using numerical techniques. Nowadays, with the widespread availability of powerful computers and advanced numerical software, direct numerical solution of the wave equation is possible. Numerical methods such as finite-elements (FEM) or finite-differences (FDM) can be used to find a robust numeric solution of the wave equation which can accurately map out dispersion, power confinement, mode shape, and other relevant parameters of a waveguide.

The work in this thesis focuses on the design, simulation and testing of PPLN ridge waveguides for applications across the UV to MIR (350-4500nm) range of optical wavelengths. In order to improve understanding of how the fabrication processes outlined in Section 3.2 affects supported modes in waveguides, the waveguide model shown in Figure 4.1 was constructed. Numerical modelling of PPLN waveguides was performed using FIMMWAVE, a commercial finite difference mode-solving package by

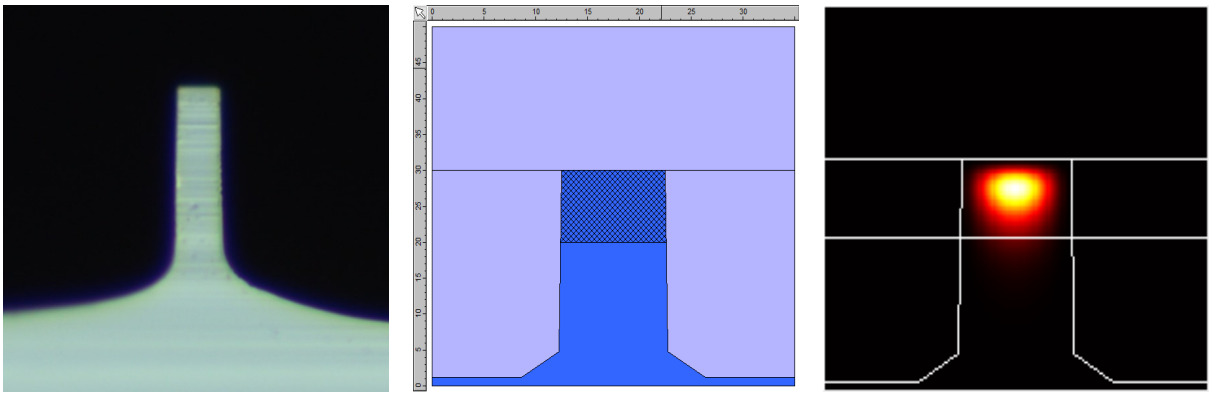

(A) (B) (C)

FIGURE 4.1: (a) Microscope image of a Zn-indiffused MgO:PPLN ridge waveguide facet used as a basis for the ridge waveguide shape in numerical model, (b) geometrical waveguide structure built in FIMMWAVE software to represent Zn-indiffused MgO:PPLN waveguides, and (c) intensity plot of a fundamental mode solution at 1560nm in a 12 µm wide ridge.

Photon Design Ltd. This model will allow for simulation of experimental results and the design of waveguides at new wavelengths for novel applications. Earlier work at Southampton investigated the effect of the Zn thickness to minimise mode field diameter, with the aim of maximising potential modal overlap [43]. Building on this work, a target of this thesis is to further decode the effect of fabrication parameters, in conjunction with mode solving software to extract a theoretical refractive index profile, with the objective of producing a matrix of refractive index profile values which correspond to standardised fabrication parameters. This model will enable us to tailor size and shape of waveguide modes, calculate an effective refractive index, n_{eff}, for a specific set of input and generated wavelengths, and calculate the PPLN period required to support a target conversion interaction.

4.1 Building the Waveguide Model

The parameters that define the model of Zn-indiffused MgO:PPLN waveguides developed at Southampton can be seen in Figure 4.2; the diced ridge width, which is well defined to $\pm$0.5µm by the machining process; and the refractive index profile, defined

by the refractive index change, δn, and diffusion depth, sometimes labelled as σ, referring to the peak amplitude value and standard deviation of a Gaussian respectively, which is the assumed shape of the profile. Together these parameters dictate which wavelengths can be supported in the waveguide, and their associated mode shape. As part of the investigation in this thesis, a bespoke code was prepared (Appendix B) to interface with FIMMWAVE, iterate over several index profile parameters, and extract data from the waveguide model, such as the effective index of TM modes, the X and Y MFD values based on a reduction of $1/e^2$ of the intensity, and a matrix array of the intensity and electric field values of the mode solutions.

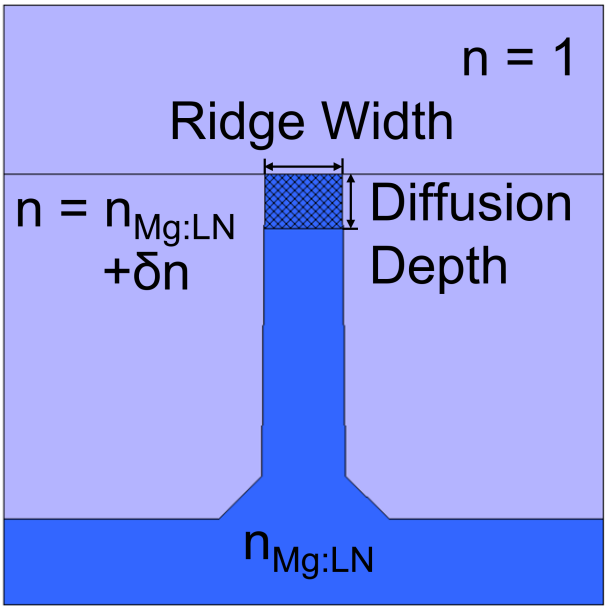

FIGURE 4.2: Parameters that define waveguide structure and guidance in the FIMMWAVE numerical model, where diffusion depth corresponds to the standard deviation of the Gaussian curve used for the diffusion profile. For planar modes it is solved in 2D, independently of the ridge width.

As a starting condition for the PPLN ridge waveguide model, a Gaussian diffusion is assumed for the refractive index profile. This is based on the zinc concentration shape in the SIMS data provided by Fraunhofer IPM for a standard 1560nm SHG waveguide, shown in Figure 3.6, and other work on charaterising zinc-indiffused lithium niobate by Nevado in [79, 87]. Fitting of the SIMS data was done with the Gaussian equation 4.1, where the standard deviation, ω, was then converted to the diffusion depth, σ =

$\sqrt{2}\omega$, from the Gaussian equation 4.2 used by the FIMMWAVE software, obtaining the value σ = 7.46 µm.

$$y = y_0 + A\,exp\left(-\frac{1}{2}\left(\frac{x - x_c}{w}\right)^2\right) \tag{4.1}$$

$$y = exp\left(-\frac{x^2}{\sigma^2}\right) \tag{4.2}$$

Optimising refractive index parameters to maximise overlap of the waveguide modes is important to achieve efficient frequency conversion. For SHG the highest overlap typically occurs between the fundamental pump and fundamental SHG modes, thus we want to couple the maximum amount of power into the fundamental pump mode. For this purpose single-mode waveguides at the highest operating wavelength are preferable, as no launched power will be coupled into modes that will not contribute to the upconversion efficiency. Matching the waveguide pump mode to the expected input laser beam size is also an aim of this work, to improve launch efficiency into the waveguide in a typical use case, without the need of complex launch optics, this is addressed in Section 4.1.3.1. In Chapter 5 it will become clear that single-mode operation does not necessarily coincide with the highest overlap integral, so a balance between the two must be found.

4.1.1 Refractive Index Profile Modelling

In order to extend the operating range of Zn indiffused PPLN waveguides to new wavelengths, an understanding is needed of how the various fabrication parameters affect the indiffusion profile. Testing was performed across an array of MgO:LN samples, by varying the deposited Zn thickness, deposition power, and temperature during the indiffusion step. These are parameters that were initially investigated to optimise MFD for fibre to waveguide coupling in [43], but had not been used to analyse the

indiffusion profile. The effective refractive index of supported planar modes was measured with the Metricon system, which uses a prism coupling technique (see Section 3.3.3).

The Metricon varies the input angle of a laser beam aimed at a prism to couple into different modes supported in the sample, and calculates an effective index value, n_{Met}, for each of the modes found, shown in in Figure 4.3. To retrieve the refractive index profile, this data is then compared to a matrix of modelled planar effective indices, n_{FW}, from the waveguide structure built in FIMMWAVE, where the indiffusion profile parameters, δn and σ, have been iterated. The indiffusion profile is established by finding which combination of refractive index change and indiffusion depths parameters give effective indices equal to effective indices measured by the Metricon for all the supported modes in that wafer simultaneously.

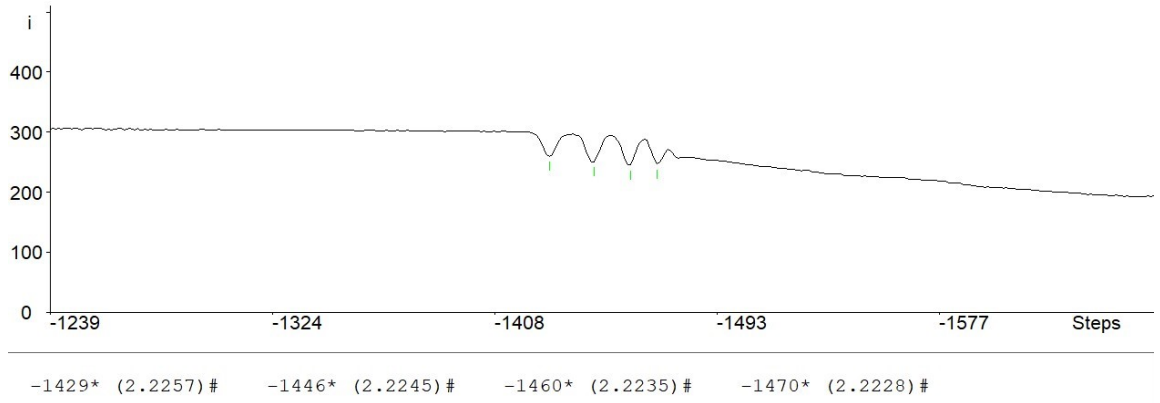

FIGURE 4.3: Reflected intensity of the 532nm TM mode recorded by the Metricon system for a Zn-indiffused lithium niobate wafer, as a function of steps, which relate to the incident angle of the laser beam. The dips denote supported modes, where their corresponding effective indices, n_{Met}, are listed next to their step position.

To calculate the refractive index parameters for a zinc indiffused LN wafer from prism coupling n_{eff} values, a Gaussian refractive index profile is used in the FIMMWAVE waveguide model, using Equation 4.2, with the peak aligned to the top of the waveguide. For planar layers formed by diffusion solving modes is performed independent of x-axis confinement; the optical propagation mode excited with the Metricon is a planar mode. An example of what the vertical cross-section of the refractive index

profile, labelled with refractive index change δn and indiffusion depth σ, and the first four modelled mode solutions in a planar waveguide can be seen in Figure 4.4.

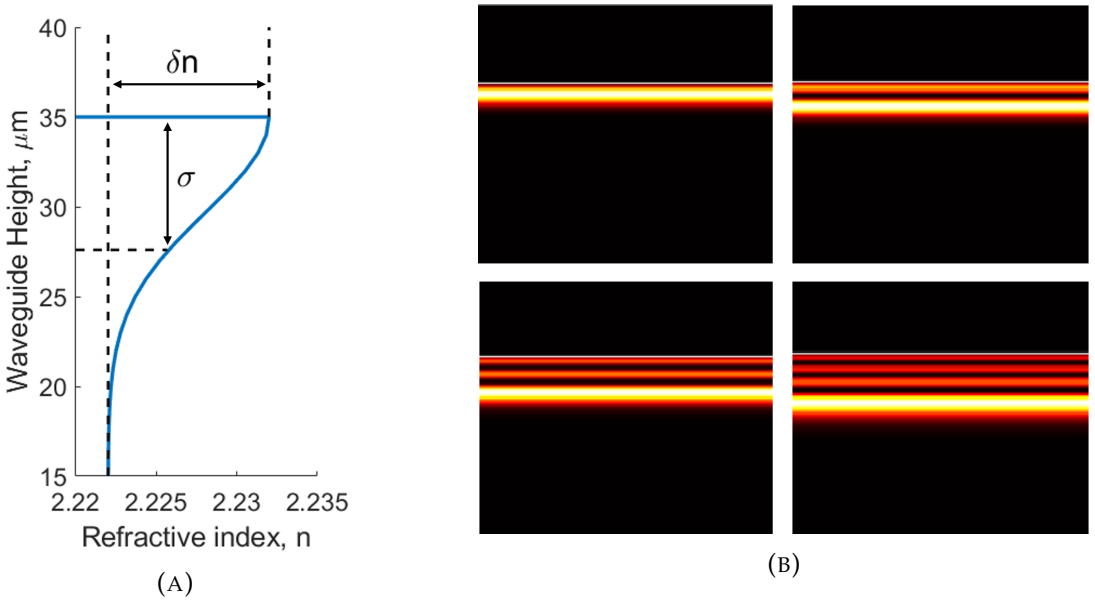

FIGURE 4.4: (a) Refractive index profile, and (b) intensity plots of the first four TM planar mode solutions found for a Zn- indiffused MgO:PPLN waveguide modelled in FIMMWAVE, with parameters; refractive index change, δn=0.0041; indiffusion depth, σ = 7.5µm.

For a wafer fabricated with standard 1560nm SHG waveguide parameters, the same as the SIMS analysis in Section 3.3.2, using the measured bulk index of the wafer at 532nm as $n_{Mg:LN}$ in the model, n_{eff} values of the first 12 TM planar mode solutions are recorded for a range of refractive index difference and indiffusion depths. These FIMMWAVE model effective indices, n_{FW}, are compared to the measured effective index, n_{Met}, for each of the modes found, establishing combinations of δn and σ where they match, as displayed in Table 4.1. Solutions are then further narrowed down by applying the assumption that refractive index parameters, δn and σ, must be the same for all measured modes. This gives possible refractive index profile parameters of δn = 0.0041 and σ = 7.40-7.50µm. Comparing this diffusion depth value to the fitting done to the SIMS profile, where σ = 7.46 µm, good agreement has been shown between the SIMS analysis and the Metricon measurements.

δ n	σ			
	m = 0	m = 1	m = 2	m = 3
0.0035				7.50-7.60
0.0036				7.50-7.60
0.0037				7.50-7.60
0.0038				7.50-7.60
0.0039		7.60	7.55-7.60	7.50-7.60
0.0040		7.40-7.60	7.40-7.60	7.50-7.60
0.0041	7.40-7.60	7.40-7.60	7.40-7.60	7.40-7.50
0.0042	7.40-7.60	7.40-7.53	7.40-7.60	
0.0043			7.40-7.48	

TABLE 4.1: Refractive index profile parameters for which the effective indices satisfied the following relation $n_{FW} = n_{Met} \pm 0.0001$, where n_{FW} is the planar mode index modelled with FIMMWAVE, and n_{Met} is the value measured with the Metricon at 532nm.

It is worth mentioning that initially, no TE modes were able to be measured with the Metricon. It was assumed there was a high loss mechanism inherent to the waveguide design, theorized to be high ZnO concentration at the top surface of the waveguide, enough to suppress the TE mode. Polishing of the top layer of the wafer eventually did yield measurable TE modes. The measurement and use of TE modes is not within the scope of this thesis.

Next, to corroborate the refractive index profile produced by SIMS and Metricon measurements was accurate, the vertical MFD at 1560nm was calculated for a range of δn and diffusion depths in the FIMMWAVE model, and the MFD value from published paper [41], 8.8µm, was plotted as the red line in Figure 4.5.

For an indiffusion depth of 7.46µm, the corresponding refractive index change that will yield an MFD of 8.8µm is approximately 0.0041. Comparing FIMMWAVE model values for refractive index change and diffusion depth retrieved from Metricon data, to those obtained by SIMS, it is seen they overlap. The modelled MFD for those refractive index profile parameters also overlaps with the measured MFD, giving confidence to the refractive index profile model for the 1560nm SHG waveguides, and to the methodology that produced the model, which can now be extended to other wavelengths.

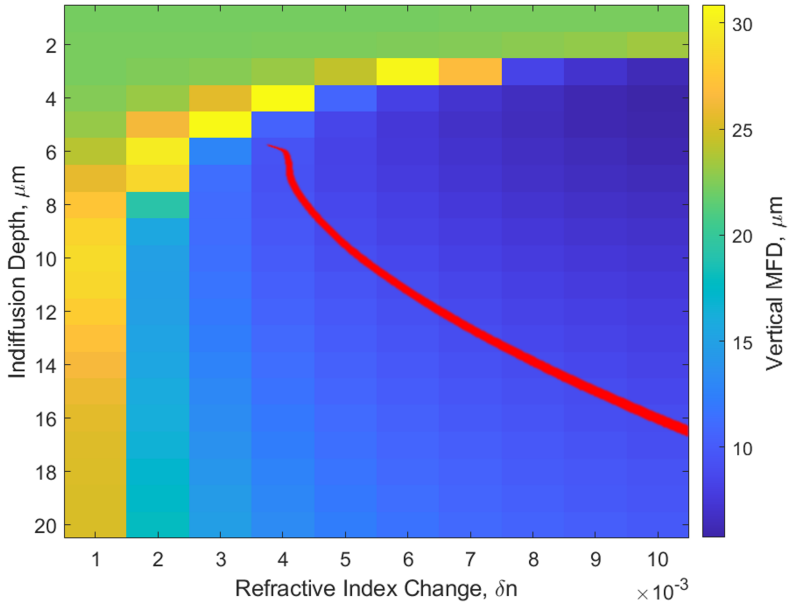

FIGURE 4.5: FIMMWAVE model values for the vertical MFD of the 1560nm mode, at a ridge width of 12µm, when varying refractive index difference, the red line represents the vertical MFD = 8.8 µm measured in [41].

4.1.2 Fabrication Parameter Characterisation

To study the effect of fabrication variables on the indiffusion profile parameters for MgO:LN wafers, several wafers were fabricated with 50-110nm thick zinc depositions, deposited at powers of 300W and 500W, and indiffused at 925°C and 950°C. Refractive index change and indiffusion depth are shown in Figure 4.6, defined via the method outlined above, and effective refractive indices measured via prism coupling at 532nm. The error bars correspond to the range of δn and σ values for which the n_{FW}=$n_{Met}$$\pm$0.00012 condition is true.

Analysis of this data shows a clear trend of increasing refractive index change with increasing zinc thickness, with a drop off below 50nm of zinc, where optical testing showed weak guidance. This reflects the trend seen for a similar zinc indiffusion process in early work by Young, where increasing the zinc thickness increases the refractive index [46], although it us unclear if they observed a similar drop for thin depositions. Decreasing the indiffusion temperature resulted in both increasing the refractive index change, and decreasing the indiffusion depth, implying there to be a

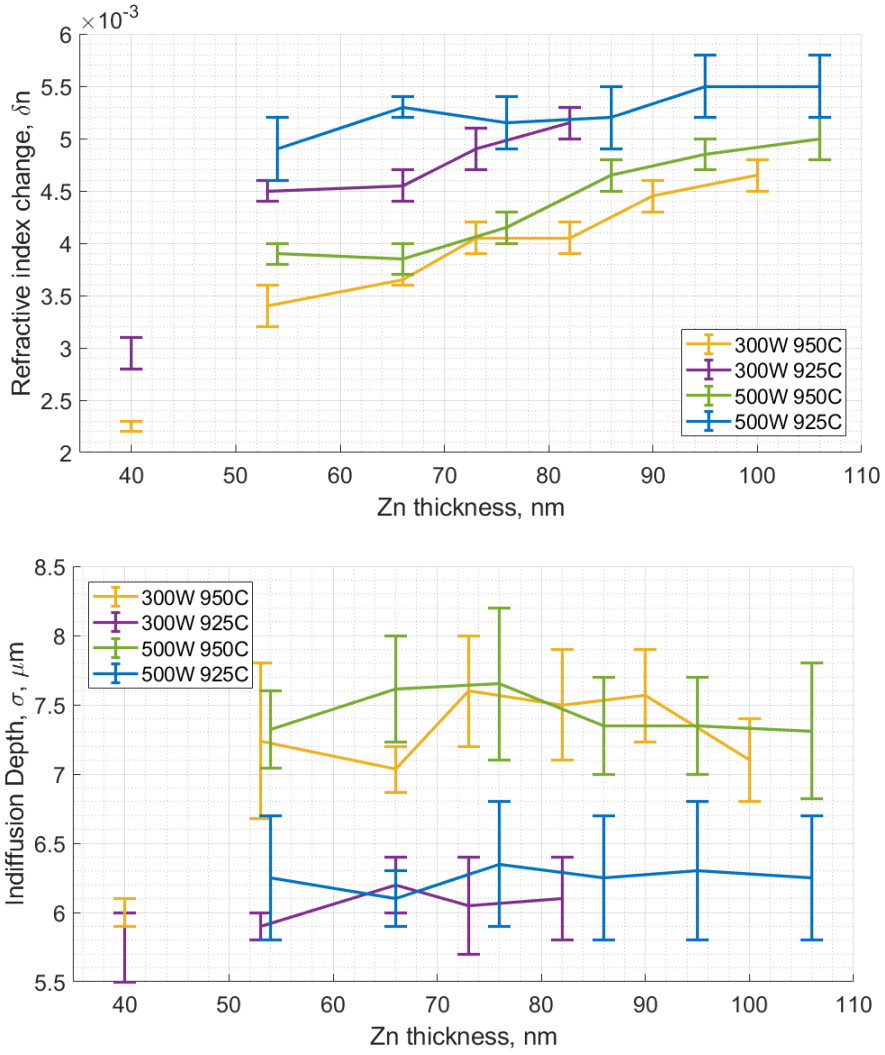

FIGURE 4.6: Calculated refractive index profile for different fabrication parameters of indiffusion temperature, deposition power, and zinc thickness, as measured using a Metricon prism coupler at 532nm. Profile parameters plotted are; (top) refractive index change, δn, and (bottom) indiffusion depth, σ.

similar amount of zinc indiffused but in different distributions. This will affect the modal shape, which is an important consideration for optical coupling. It can also be seen that a higher sputter deposition power can slightly increase the refractive index change, but seems to have no discernible effect on indiffusion depth. These findings are corroborated by the behaviour of titanium indiffused in LN slab waveguides observed by Caccavale [89], where thickness of the dopant film and the diffusion temperature determined the depth-diffusion shape.

As a starting point for designing a Zn-indiffused MgO:PPLN ridge waveguide for a 1064-532nm SHG process, the effective indices were also measured at 1064nm, with

the calculated refractive index change and indiffusion depth shown in Figure 4.7. Since there are fewer modes at this wavelength, the errors are larger, and the refractive index change trends are less clear, the 925°C indiffusion appears flat. However, the indiffusion depth shows good agreement with the 532nm values. The refractive index difference δn achieved is dependent on wavelength and decreases slightly for longer wavelengths, whereas the indiffusion depth remains the same, as there is a linear dependence between zinc concentration and refractive index change [78], which means the Gaussian shape isn't distorted. The above gives a good guide for starting characteristics for waveguide design, to be discussed in Section 4.1.4.

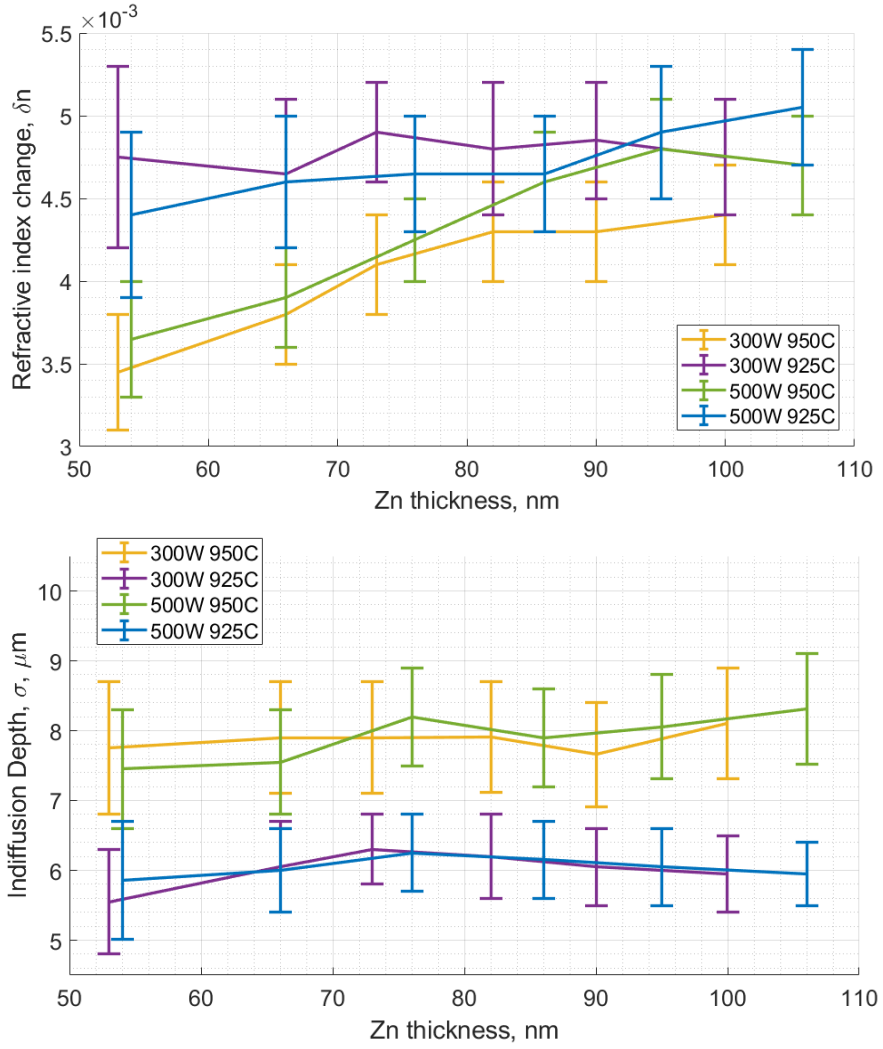

FIGURE 4.7: Calculated refractive index profile for different fabrication parameters of indiffusion temperature, deposition power, and zinc thickness, as measured using a Metricon prism coupler at 1064nm. Profile parameters plotted are; (top) refractive index change, δn, and (bottom) indiffusion depth, σ.

4.1.3 Waveguide Modes

In order to analyse the modal structure of waveguides deposited under different fabrication conditions, waveguide ridges were diced into the test wafers characterised in the previous section, to enable X and Y mode field diameters to be measured at 1560nm, using the MFD technique described in Section 3.3.4.

To measure vertical MFD, the laser spot was coupled into the planar layer of a diced wafer, at several points along the planar section to test uniformity of guiding layer along each wafer, shown in Figure 4.8. The vertical MFD is measured at ∼9µm for all the measured wafers, with the exception of the 60nm of Zn indiffused at 950°C, which according to the refractive index parameter data in Section 4.1.1 has the lowest δn and highest indiffusion depth, resulting in the mode not being as tightly confined.

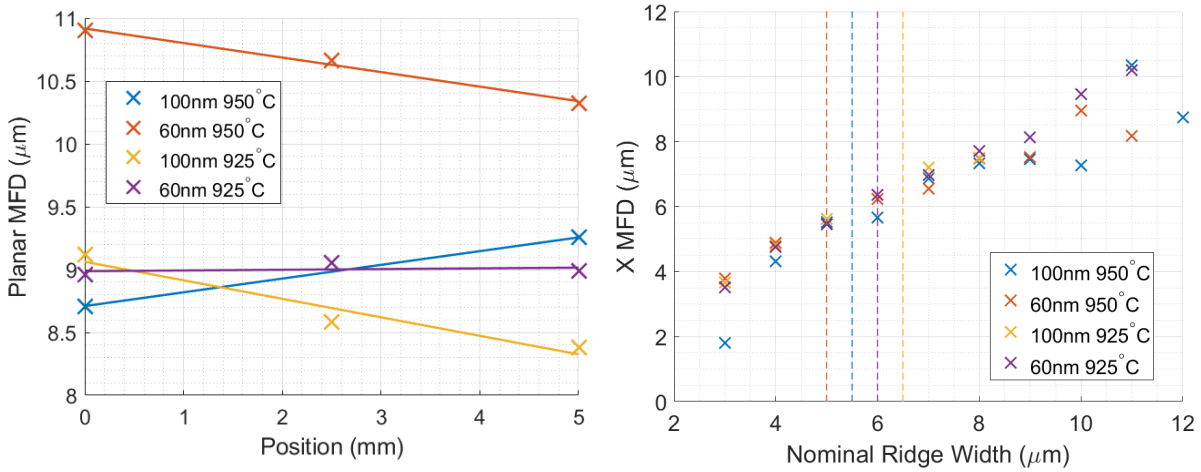

FIGURE 4.8: Measured MFD at 1560nm of waveguides in test wafers with 60nm and 100nm of zinc deposited, and indifused at 950°C and 925°C, (left) vertical MFD measured in a planar layer, and (right) horizontal MFD measured in ridge waveguides, where the dotted lines indicate where the waveguide becomes multi-mode. Data taken by Dr. Paolo Mennea.

The horizontal MFD is plotted against the nominal width of the waveguide ridge, where the dotted lines indicate where the waveguides become multi-mode for each of the different wafers at a 1560nm wavelength. It can be seen that all of the measured waveguides become multi-mode at ridge widths between 5 and 6µm, with the wafers

indiffused at a lower temperatures supporting single modes for higher nominal ridge widths.

4.1.3.1 Modelling Fibre Overlap

With the free-space coupling setup described in Section 3.3.5, the zoom collimator can be used to adjust the size of the focus, allowing us to maximise pump throughput and generated SHG power. However, for commercial optical waveguide packaging, ideally we want to mode-match with standard fibres to maximise input coupling. Modelling allows us to find what refractive index profile parameters would give the best overlap with these standard optical fibre types, but that could potentially decrease the overlap integral and conversion efficiency inside the waveguides, so there's a trade-off between the two. An example of the electric field mode profile for the fundamental mode in zinc-indiffused waveguides is shown in Figure 4.9, where the dashed grey line indicates the 1/e point to calculate the MFD for the mode, and the dashed green line shows the shape of a Gaussian. Unlike in optical fibres, the distribution of the refractive index profile means the waveguide mode is not Gaussian.

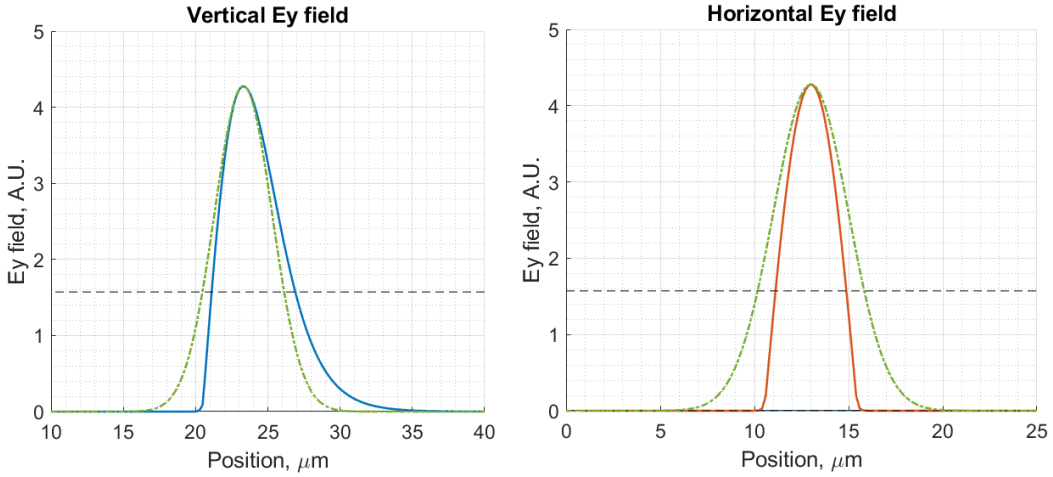

FIGURE 4.9: FIMMWAVE model image of the Ey field profile, and its vertical and horizontal cross-section, of a 1064nm fundamental mode in a 5µm wide waveguide, with refractive index profile parameters δn=0.0046 and σ=6µm. The dashed green line denotes a Gaussian centred on the peak.

Initially, we've looked at what Gaussian MFD would be optimal for the refractive index profile parameters measured. Figure 4.10 displays the dependence of the overlap integral, calculated as in Equation (5.1), on the MFD of a Gaussian mode, for the 3 modes supported in the waveguides. Each time the Gaussian mode is centred on the peak of the electric field to maximise overlap. This Figure shows that maximum overlap is achieved with the fundamental, closely followed by the bottom lobe of the 1st-st order vertical mode. Also, larger ridges slightly increase the maximum overlap achieved.

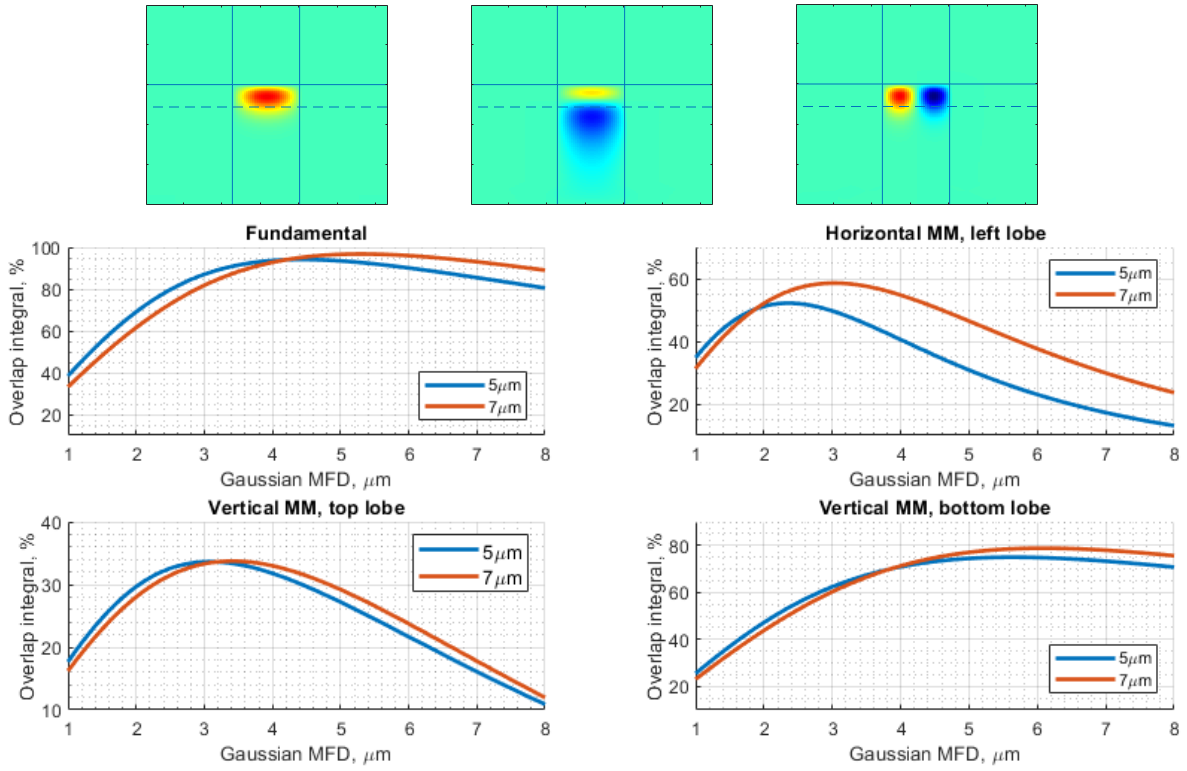

FIGURE 4.10: (Top) Images of TM modes supported in a 7µm wide waveguide, with refractive index profile parameters; refractive index change δn=0.0046 and indiffusion depth σ=6.0µm, marked by the dashed line. (Bottom) Overlap integral values for a Gaussian mode with each waveguide mode above, centred on the peak of their electric field profile.

The intensity profile of a theoretical, launched Gaussian beam [95] is

$$I(x,y) = A\exp\left(\frac{-2r(x,y)^2}{w^2}\right) \tag{4.3}$$

Future projects and commercial prospects rely on efficiently fibre-coupling these waveguides for field deployment and long-term stability in the launch alignment.

4.1.4 Towards Other Wavelengths

Early development of Zn indiffused MgO:PPLN ridge waveguides at Southampton focused on optimising 1560nm SHG waveguides to maximise conversion efficiency and multi-Watt power handling. The focus of this thesis is on establishing an understanding of the fabrication process of these waveguides, based on a novel combination of characterisation processes, and applying this to numerical modelling which defines the parameters to achieve an optimise other wavelength interactions, and extending the range of wavelengths which can be supported. Having developed a model for the waveguide refractive index profile at 1560nm, an investigation was performed to adapt waveguides to short visible wavelengths, the simplest step being altering only the ridge widths. Wavelengths at 1064 and 780nm were chosen for SHG to green and blue, as there is an interest in them for quantum computing applications, and these match readily available pump sources. These first examples were chosen to prove the FIMMWAVE model before advancing to the more complex problem of refractive index profile required for SFG and DFG interactions with MIR wavelengths, as they involve very different wavelengths.

A range of ridge widths were modelled to find the ones which would support the wavelengths of interest at single mode. The suitability of the ridge widths was quantified with the normalised guide index, b, which is calculated as in Equation 4.4, giving a range of possible values. The same process was carried out for finding the 780nm SHG and 1064nm SHG waveguide ridge widths. The design parameters based on a 100nm thick layer of sputtered zinc were; for 780nm SHG, 4-7μm ridge widths and periods Λ = 2.35-2.37 μm, and for 1064SHG 5-11μm ridge widths and periods Λ = 6.8-6.9

µm, as show in Figure 4.11.

$$b = \frac{n_{eff}^2 - n_{MgO:LN}^2}{n_{MgO:LN+\delta n}^2 - n_{MgO:LN}^2} \tag{4.4}$$

Building an understanding of the behaviour of the mode when varying the model pa-

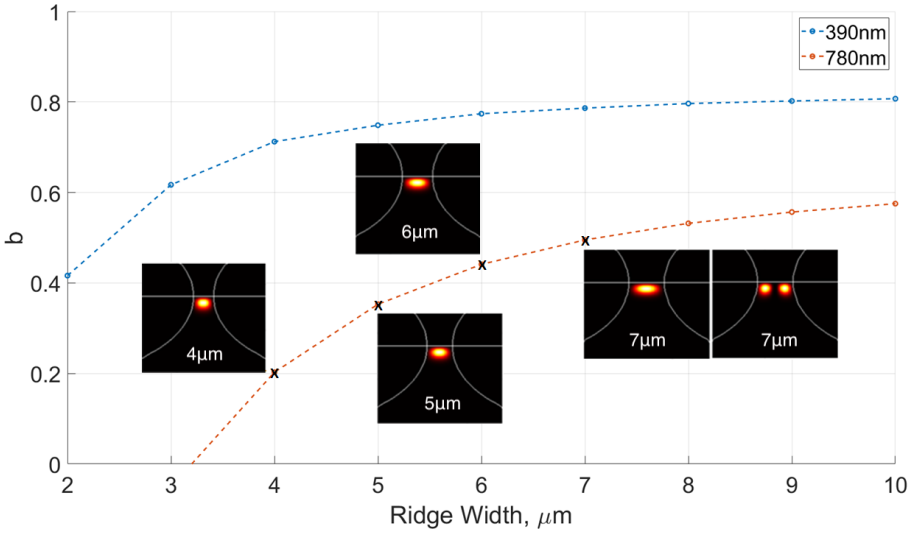

(A)

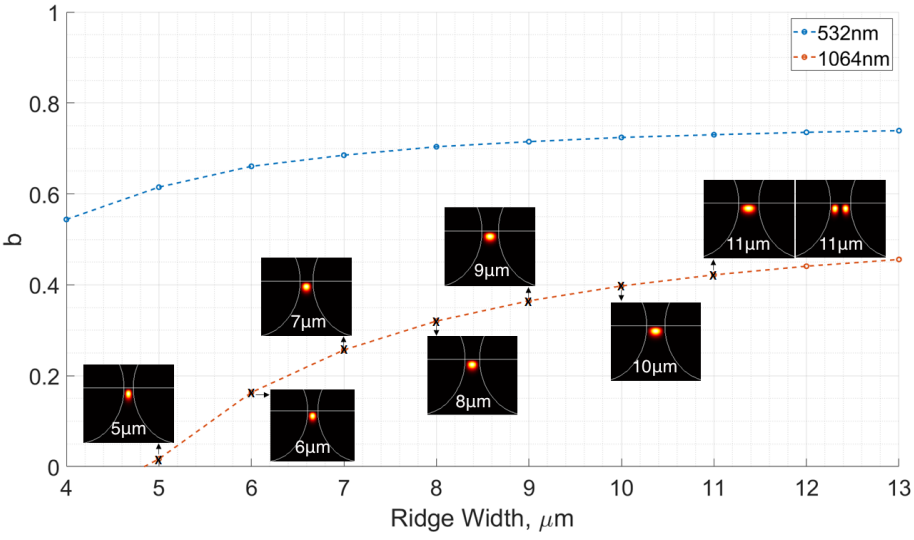

(B)

FIGURE 4.11: Normalised guided index values plotted against ridge width, with an overlay of the FIMMWAVE modal solutions at each ridge width, for (a) the 780SHG process, and (b) the 1064SHG process.

rameters will give us direction when modifying fabrication parameters to make specific interaction waveguides.

4.2 Conclusions

Chapter 4 outlines the development and application of a numerical model to study zinc-indiffused PPLN waveguides. The model is used to infer refractive index parameters from fabrication parameters, such as zinc thickness, deposition power, and indiffusion temperature. These predictions are validated against experimental data, enabling the design of waveguides with optimal mode confinement and nonlinear conversion efficiency. The chapter explores how waveguide dimensions and refractive index changes affect coupling efficiency and supported wavelengths. By tailoring fabrication parameters, the models guide the development of waveguides suited for specific applications.

Chapter 5

PPLN Waveguides for SHG to UV and Visible Wavelengths

Wavelengths at the lower end of the MgO-doped lithium niobate transparency window have a plethora of use cases. Compact and low-cost laser devices emitting in the blue and ultra-violet (UV) are of growing importance in quantum technologies such as atom cooling [96] and quantum computing [97] to create portable systems for timing and navigation. Of particular interest is achieving 369.5 nm sources for the Doppler cooling of Yb+ ions [98], where ridge-type PPLN waveguides have already demonstrated high-efficiency generation of light as low as 340nm before [99]. High power laser emission in the green region typically relies on nonlinear conversion due to a lack of materials for direct emission, and green sources can also be used as a pump for solid state lasers such as Ti:sapphire [100]. At lower powers, molecular iodine has a transition at 532nm which has been used to build an atomic clock [101].

The work presented in this Chapter applies the nonlinear theory presented in Chapter 2, with PPLN waveguide fabrication techniques and characterisation techniques of Chapter 3, with the modelling and design elements of Chapter 4 towards the realisation of extending the Zn-indiffused MgO:PPLN diced ridge waveguide fabrication process towards devices that operate in the 370-532nm range of wavelengths. These

particular wavelengths were chosen due to availability of the laser sources and components and relative ease of SHG phasematching experiments when dealing with visible wavelengths. The results at these wavelengths will be compared to the numerical modelling presented in Chapter 4 to test numerical model robustness, and inform the design of future waveguides at MIR wavelengths.

5.1 Visible and Near Infrared Waveguides

Waveguides for operation at visible wavelengths are typically more challenging to fabricate compared to those designed for telecom wavelengths, due to their smaller aperture size and shorter poling period, placing tighter tolerances on the fabrication process. Moving to shorter wavelengths also means dealing with faster changes in chromatic dispersion and a higher sensitivity to small changes in propagation constant of pump and SHG modes, which in our case is dependent on ridge width variation and uniformity of Zn deposition and indiffusion.

A first-order 780nm SHG waveguide has been previously fabricated at Southampton [48], with a short period length of 2.2-2.4μm. The fabrication challenges associated with fine-period domain poling can result in reduction of the nonlinear coefficient and thus conversion efficiency. A maximum CW output power of 1mW and a conversion efficiency of 6.9%/W was obtained in a 14mm long crystal. Longer waveguide devices would increase the conversion efficiency, and the high damage threshold of a Zn-indiffused ridge waveguide structure [41] could open the door to using third-order poling at higher pump powers to increase overall conversion efficiency.

Our objective is to make single mode waveguide devices in the visible regime. Individual waveguide modes have distinct phasematching conditions, at different temperatures or wavelengths, thus we want to avoid coupling pump power into additional modes that will not contribute to conversion efficiency. Additionally, maximising the overlap integral of the pump and SHG modes is paramount for an efficient interaction

as SHG power is directly proportional to the square of this figure, shown by Equation 3.1. For most quantum systems simple, standardised components are preferred, these would benefit from efficient fibre-to-waveguide coupling, so a numerical investigation into how mode shape and size affects coupling efficiency to optical fibre was also carried out. Typical MFDs for commerically available fibres are listed in Table 5.1.

	Name	Wavelength	MFD
ThorLabs	PM980-XP	970 - 1550nm	6.6 ± 0.5 µm @ 980 nm
Newport	F-HB1060-7	1015 - 1105 nm	6.0 - 8.0 µm @ 1064 nm

TABLE 5.1: Listed mode field diameters for commercially available 1064nm PM fibre.

5.1.1 Numerical Modelling

The FIMMWAVE numerical model presented in the previous Chapter (Figure 4.2) was used to analyse the waveguide structure parameters needed to meet the criteria set out for visible PPLN waveguides. This is done by adjusting refractive index change and indiffusion depth, and building a matrix of waveguide mode variables that accounts for changes in controllable fabrication parameters within known tolerances. The range of variables for the model was chosen to be; 5µm to 7µm ridge widths, based on the fibre MFDs and normalised guide index values found in Section 4.1.4; refractive index change of 2 to 6x10^{-3} based on what has been achieved already (Figure 4.6); and indiffusion depths of 2 to 7 µm, based on the assumption that a shallower indiffusion depth than that used for 1560nm SHG waveguides will be needed, for the smaller 1064nm and 780nm modes. The base lithium niobate refractive index was given by the temperature-dependent Sellmeier equation from Gayer [59], set to a temperature of 11^{o}C to closely match the bulk indices measured by the Metricon at 532nm and 1064nm, given by 2.2207 and 2.1446 respectively.

Figure 5.1 shows the number of modes supported in 5µm and 7µm wide ridge waveguides respectively, where the condition at which the mode is guided is set by the absolute value of the imaginary effective index. As no absorption coefficient is set for lithium niobate in the numerical model, loss is simulated by an absorbing layer placed on the boundary of the model which measures the radiating field outside the waveguide structure. Firstly, by comparing these tables, we find that single-mode operation is achievable across a wider range of fabrication conditions in the narrower 5µm ridge, whereas conditions for single-mode guidance in the 7µm ridge are stricter, making it more difficult to reliably fabricate, as the tolerances for the deposited Zn thickness and indiffusion temperature are much smaller, in addition to not being as well confined. Secondly, these tables have provided a clearer picture of what refractive index profile parameters to aim for single-mode operation, and how they change.

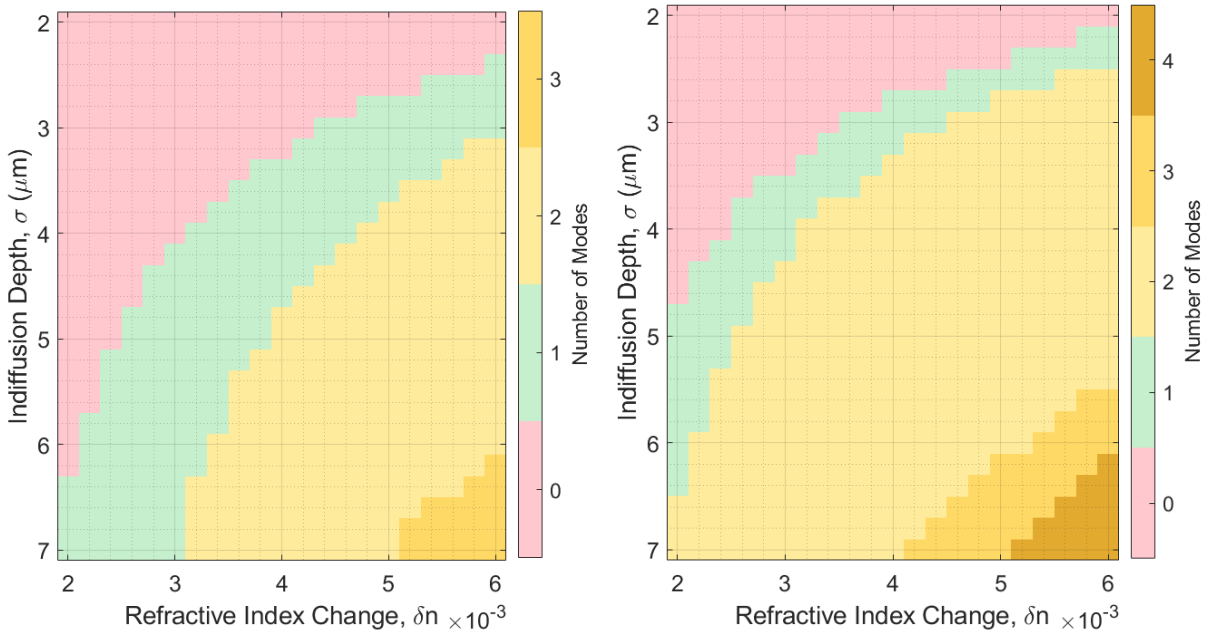

FIGURE 5.1: Graphs displaying the number of 1064nm modes found by the numerical model supported in; (left) a 5µm wide ridge waveguide, (right) a 7µm wide ridge waveguide, when varying refractive index profile parameters.

As previously alluded to, the use of waveguides introduces another factor: mode overlap. The modes in a waveguide have well-defined wavelength-dependent transverse spatial variations, thus the distribution of energy in the fundamental and second-harmonic waves may differ, thereby reducing the efficiency of energy transfer between

them. Therefore the nonlinear overlap integral, ζ_{OV}, between pump and signal waveguide modes must be calculated. This quantifies the linear degree of confinement, with units of m^{-1}, the efficiency with which a mode with electric field distribution $E_p^2(x,y)$ can excite a field $E_s(x,y)$, and differs from the overlap integral used for mode matching, which is dimensionless. A more intuitive way of understanding the nonlinear overlap integral would be to convert it to effective area of the nonlinear interaction, A_{eff}, where $A_{eff} = 1/\zeta_{OV}^2$ a quantitative measure of the area which a mode effectively covers in the transverse dimensions, where a smaller effective area means tighter confinement, resulting in a more efficient interaction.

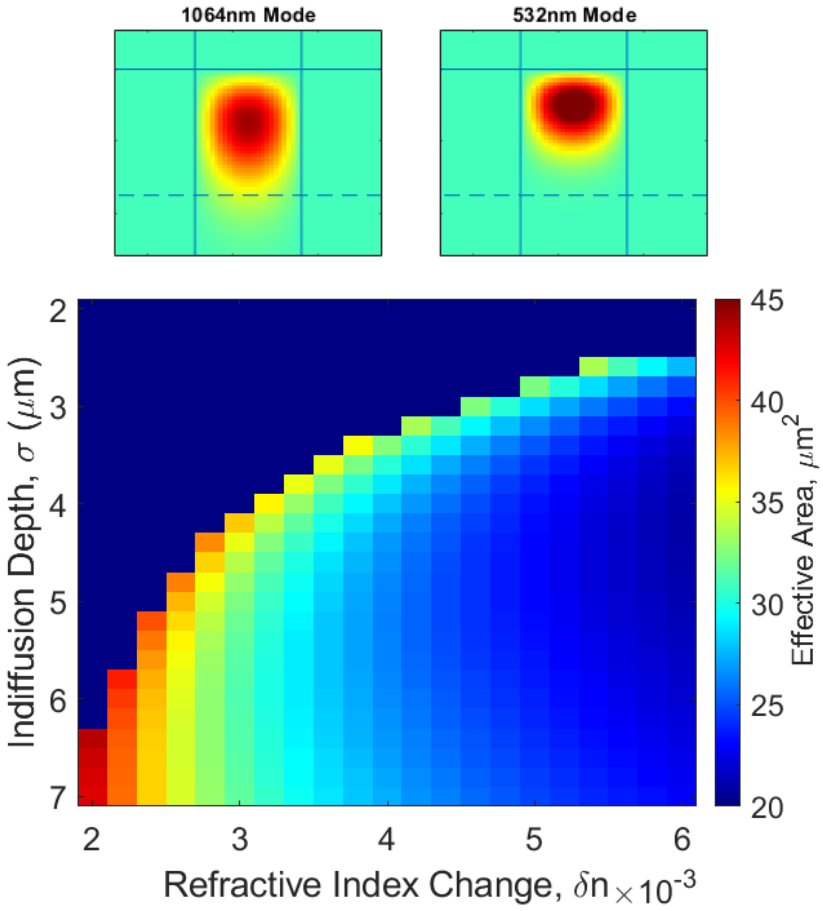

FIGURE 5.2: Nonlinear overlap integral values for fundamental 1064nm to fundamental 532nm mode in a 5μm wide ridge waveguide, for a range of refractive index profile parameters.

Figure 5.2 shows the electric field amplitude distribution of the fundamental 1064nm mode and the fundamental 532nm mode it is exciting for a 5μm wide ridge waveguide, and the effective area between them calculated using Equation 2.17 and FIMMWAVE

modelled vertical electric fields at 532nm and 1064nm. Doubling the effective area reduces the SHG interaction efficiency by 4. The smallest effective area is achieved at the highest change in refractive index modelled, with shallow indiffusion depths between 4.0 and 4.4µm, resulting in an effective area of 21.3µm^2. Moving to a refractive index change of 5x10^{-3}, with the same indiffusion depths, the nonlinear interaction has an effective area of 23.5-23.9µm^2 (10-12% increase) which would decrease the overall conversion efficiency to ∼80% of the one achieved with 6x10^{-3}. Moving across further to a refractive index change of 4x10^{-3} with the same indiffusion depth, the effective area increases to 27.2-28.2µm^2 (27.7-32.4% increase), halving the conversion efficiency with respect to the highest refractive index change modelled.

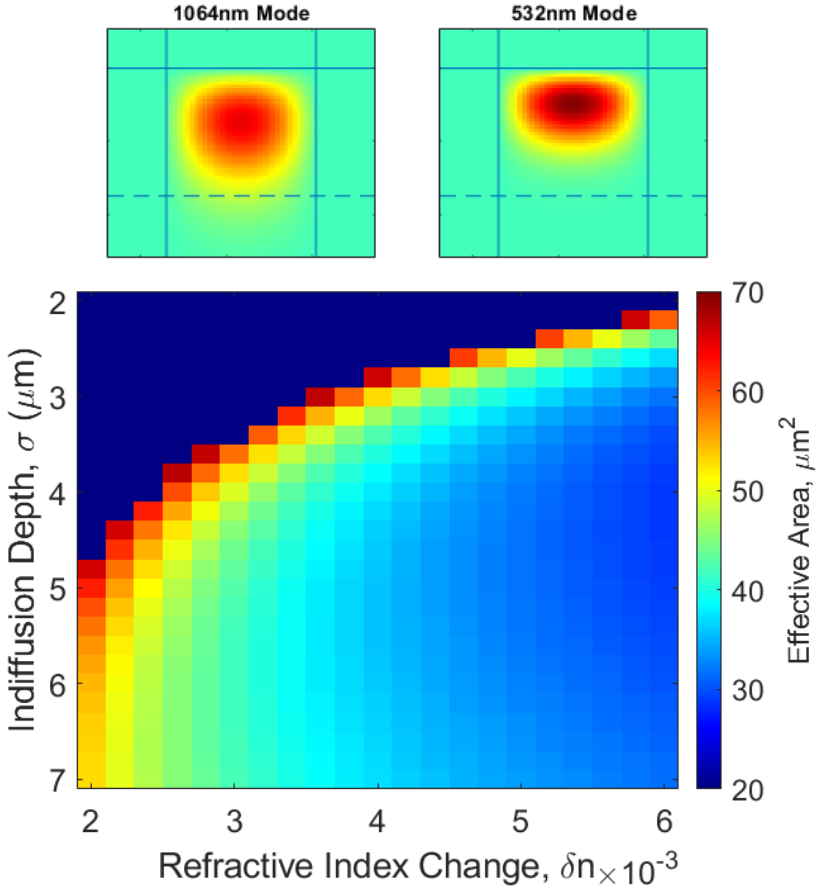

FIGURE 5.3: Nonlinear overlap integral values for fundamental 1064nm to fundamental 532nm mode in a 7µm wide ridge waveguide, for a range of refractive index profile parameters.

Similarly for a 7µm wide ridge waveguide, Figure 5.3, the smallest effective area 28.9µm^2 is achieved with a refractive index change of 6x10^{-3}, at indiffusion depths between 4

and 4.4µm. This means that for a completely 'perfect' waveguide (lossles, constant n_{eff} along the propagation length), with the same amount of light coupled into the fundamental 1064nm mode, a 7µm wide ridge waveguide will produce half the SHG power of a 5µm with the same refractive index profile parameters.

The fundamental 1064nm mode can phasematch with different 532nm modes, given the right phasematching condition, and sufficient spatial overlap to allow energy transfer between the pump and signal modes. Figure 5.4 displays the effective area for the 1064nm fundamental mode with the 1st-order 532nm vertical mode (TM01). The negative amplitude of the electric field in a 1st-order vertical mode reduces the nonlinear overlap integral, but the lack of vertical symmetry means the integral is not negligible, with an effective area about 3.5 times larger than for the fundamental-to-fundamental conversion, in both the 5 µm and 7 µm ridges.

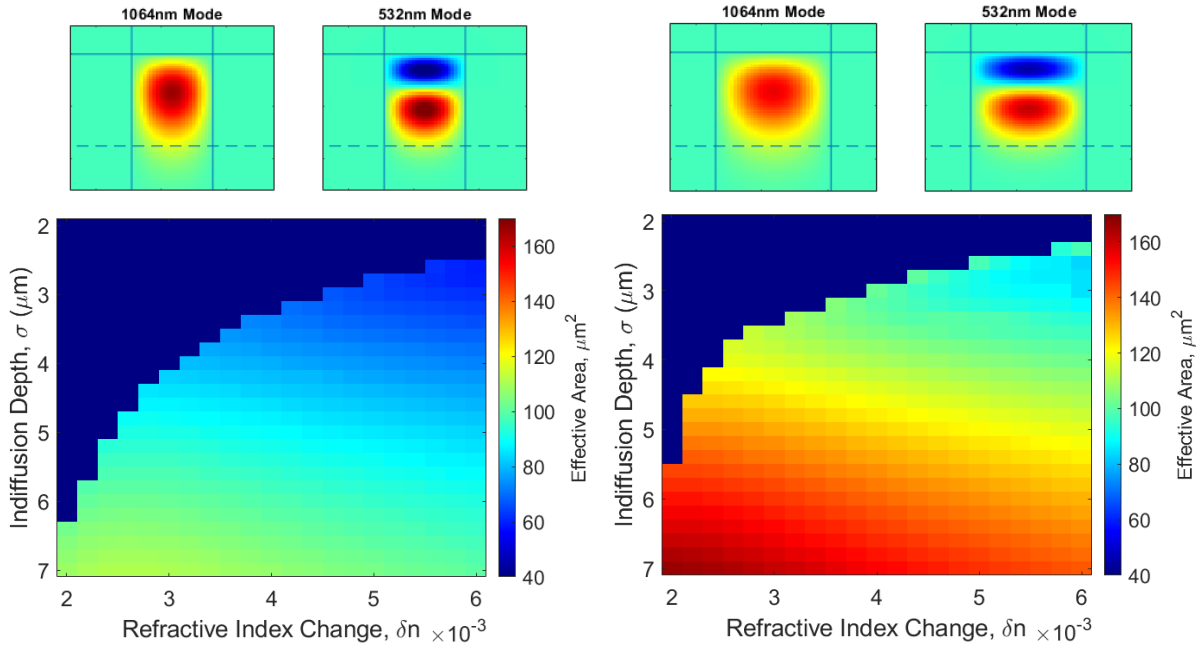

FIGURE 5.4: Nonlinear overlap integral values for fundamental 1064nm to 1st vertical SHG mode in a 5µm (left) and 7µm (right) wide ridge waveguide, for a range of refractive index profile parameters.

As a starting point to studying fibre coupling into waveguides, we define the theoretical mode matching of two beams/modes, η, with respective complex electric fields E_1

and E_2, as

$$\eta = \frac{\int\int_{-\infty}^{\infty} E_1^* E_2 \, dx \, dy}{\left[\int\int_{-\infty}^{\infty} E_1^* E_1 \, dx \, dy \int\int_{-\infty}^{\infty} E_2^* E_2 \, dx \, dy\right]^{\frac{1}{2}}} \tag{5.1}$$

Assuming a smooth end-facet for coupling light and the optical phase profile of the beams are matching, this quantifies the spatial overlap between them, and can be used to calculate the coupling efficiency of a laser beam, E_1, to a waveguide mode, E_2. The modal overlap between a Gaussian beam with MFDs of 6µm and 8µm, and a 1064nm fundamental mode in a 7µm wide ridge was calculated for a range of refractive index changes and indiffusion depths, as shown in Figure 5.5. The position of the Gaussian mode was adjusted to maximise the calculated overlap integral.

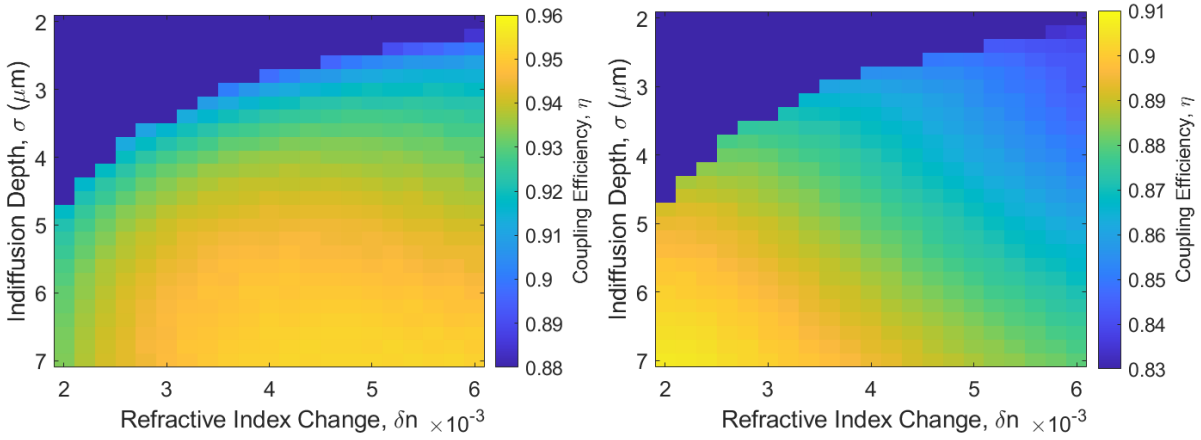

FIGURE 5.5: Theoretical coupling efficiency values to quantify the quality of mode match between the 1064nm fundamental mode in a 7µm wide ridge waveguide, and a Gaussian beam with MFDs of; (left) 6 µm, and (right) 8 µm, for a range of refractive index profile parameters.

The coupling efficiency of a Gaussian beam is better in the wider ridge, with coupling being 6 percentage points higher than for the narrower 5µm wide ridge for a Gaussian with MFD of 6µm, and 9 percentage points lower for a Gaussian with MFD of 8µm. From this data, it can be seen that a greater overlap happens for larger diffusion depths, it becomes apparent from Figure 5.6 that as the indiffusion depth increases the waveguide mode becomes more circular, and more closely matches the Gaussian beam shape. Figure 5.6 also shows why higher δn gives higher nonlinear overlap integrals, the 1064nm mode shape is more similar to the 532nm mode shape.

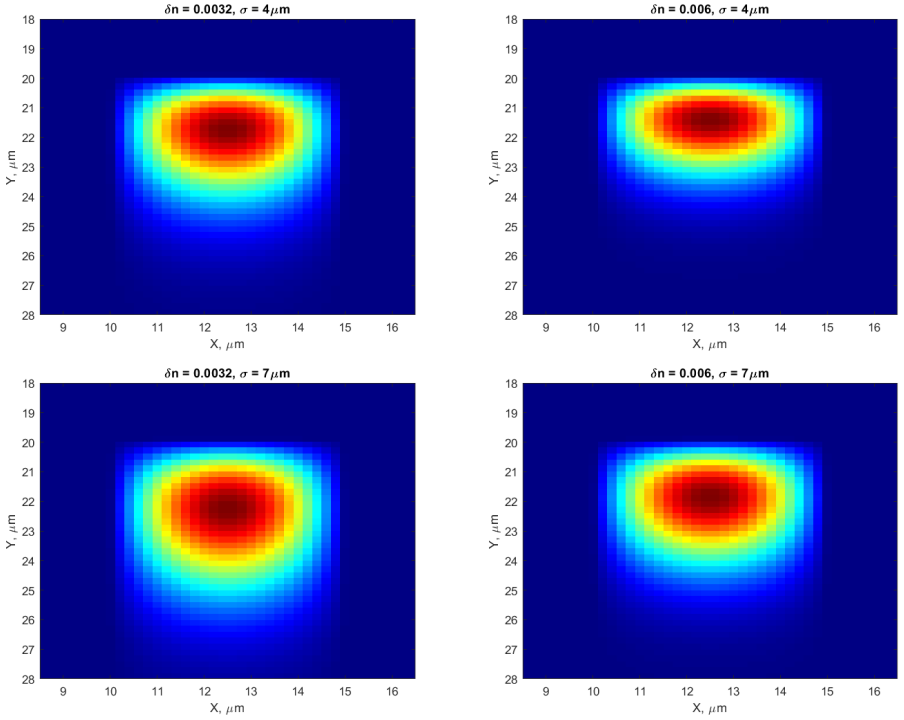

FIGURE 5.6: Model 1064nm mode profiles showing the effect of refractive index profile parameters; a) δn = 3.2x10$^{-3}\sigma$ = 4µm b) δn = 6.0x10$^{-3}\sigma$ = 4µm c) δn = 3.2x10$^{-3}\sigma$ = 7µm d) δn = 6.0x10$^{-3}\sigma$ = 7µm, on waveguide mode shape in a 5µm wide ridge waveguide.

Optimal refractive index parameters for nonlinear overlap differ from those for best coupling efficiency to fibre. Additionally, areas of high coupling efficiency have multimode operation, which would reduce coupled power into fundamental mode. Since SHG power is proportional to the square of both the coupled pump power and the nonlinear overlap integral, Figure 5.7 looks at how the combination of these overlaps, $P_1^2\zeta_{OV}^2$, changes with refractive index profile.

Assuming the launched mode is a Gaussian beam with an MFD of 6µm, which gave the highest theoretical launch coupling efficiency, the maximum combined efficiency overlap value for both the 5µm and 7µm waveguide happens at δn = 0.006, and σ = 4.6µm. From the Figure, the key parameter in maintaining a high overlap integral value is the refractive index change, as it changes more rapidly than when varying indiffusion depth. For this range of refractive index profile parameters, where the launch coupling efficiency does not vary greatly, the nonlinear overlap value holds

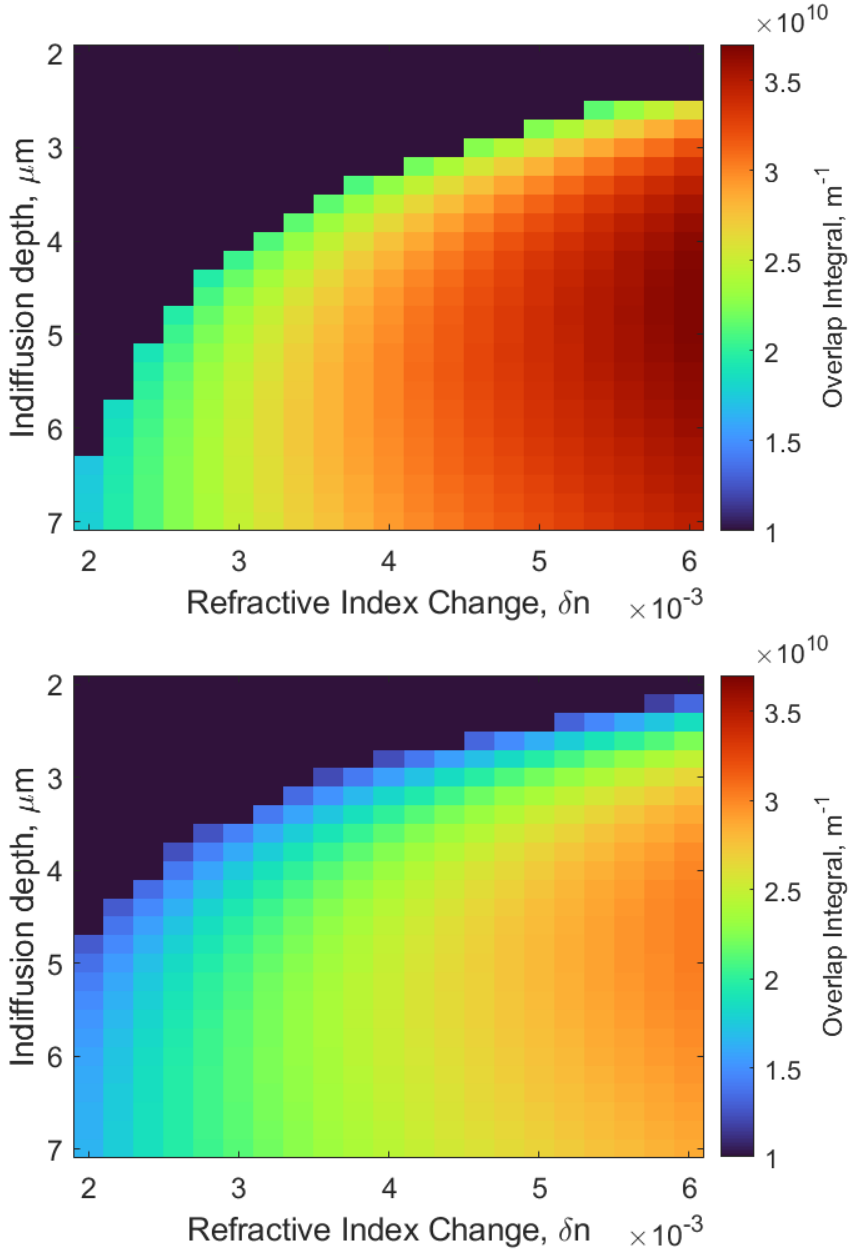

FIGURE 5.7: Quantified efficiency, $P_3 \propto \zeta_{OV}^2 P_1^2$, consisting of nonlinear overlap integral, ζ_{OV}, between fundamental 1064nm and 532nm modes, and waveguide coupling efficiency, P_1, between a 6μm Gaussian mode and the fundamental 1064nm waveguide mode; (top) 5μm wide ridge waveguide, (bottom) 7μm wide ridge waveguide.

more weight than the launch coupling efficiency. Even with the lower coupling efficiency of a Gaussian mode into the 5μm wide ridge waveguide mode, the combined overlap integral is 19% higher than for the 7μm wide ridge waveguide. These refractive index profile parameters for 5-7μm waveguides support 2 modes at 1064nm, the fundamental and 1st-order horizontal mode (TM10), however, since the TM10 mode is odd, no light from the fundamental will be lost to that mode.

Utilising the relationship of LN wafer fabrication parameters to the depth-diffusion shape of the refractive index profile from Chapter 4; increasing the sputtered zinc layer thickness increases the refractive index change up to a saturation point for a given temperature, and increasing the furnance temperature increases the indiffusion depth of the zinc layer, while slightly decreasing the refractive index change; applied to waveguide design to achieve the desired profile for a 1064nm SHG waveguide, lower furnace temperature to reduce indiffusion depth.

5.1.2 Prism Coupling

A series of wafers were fabricated with an indiffusion temperature of 900^{o}C, deposited with nominal zinc thicknesses ranging from 40 to 100nm, at 300W of power, and characterised with the prism coupling technique and method referred to in 4.1. Results for the 900°C indiffused wafers' refractive index profile parameters, δn and σ, are shown in Figure 5.8, using effective refractive indices measured at 532nm. They are plotted alongside prism coupling results from Section 4.1.2 with 300W deposition powers, for comparison of the different indiffusion temperatures. The error bars correspond to the range of δn and σ for which the n_{FW}=$n_{Met}$$\pm$0.0001 condition is true. Wafer C121 was used by Dr. Gray to achieve first-order 780nm SHG in a PPLN waveguide at Southampton [48], and is listed here as a possible target refractive index profile for 780nm SHG waveguides.

As expected, the lower indiffusion temperature used to fabricate this sample decreased the indiffusion depth, encompassing the 4.6µm indiffusion depth required to maximise the combined overlap integrals and therefore strength of the interaction. It also slightly increased the refractive index change with respect to the other indiffusion temperatures, following the trend identified in Section 4.1.2.

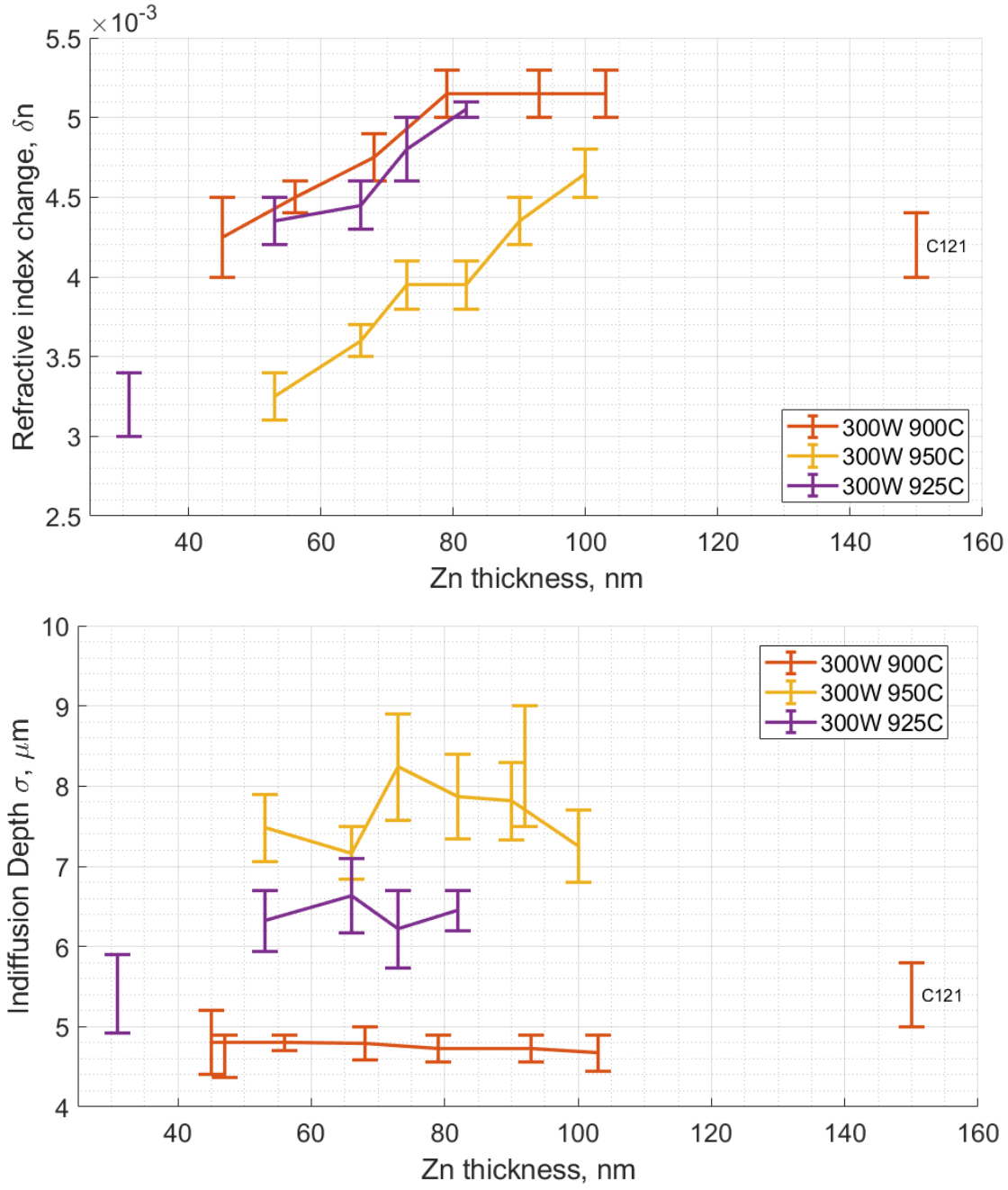

FIGURE 5.8: Modelling results of refractive index profile parameters based on Metricon prism coupling measurements at 532nm, for different fabrication parameters; indiffusion temperature and zinc thickness, including the new wafer indiffused at 900°C. The bar labelled C121 is the wafer used for 780nm SHG in Dr. Gray's paper [48].

5.2 Fabrication of 1064nm SHG Waveguides

The maximum conversion efficiency $\zeta_{OV}^2 P_1^2$ of Figure 5.7 had refractive index profile parameters of δn=6x10^{-3} σ=4.6μm, which is a multi-mode at both 5μm and 7μm. In the 5μm waveguide the second supported mode is a 1st-order horizontal mode (TM01)

which has an overlap integral of 6% with the Gaussian launch mode, there is also a lossy 1st-order vertical mode which has an overlap integral of 12% with the Gaussian launch mode, calculated with the launch position that maximises overlap with the fundamental waveguide mode, to emulate real-life coupling. Overlap integral is computed over the whole area of the model area, 25µm by 50µm for the lossy modes, as they extend further down into the waveguide. This means ∼20% of the pump light would be lost to other modes.

To achieve single-mode waveguides with the highest $\zeta_{OV}^2 P_1^2$, the refractive index profile parameters would be δn of 4.0x10^{-3}, and σ of 4.6µm, which also has a 20% reduction in its nonlinear overlap integral value when compared to the largest value. As single-mode operation is valued, the waveguides will be fabricated with the lower refractive index change. The lowest diffusion depth measured in in Figure 5.8 ranged from 4.4µm to 5µm, and lowest refractive index change ranged from 4.0x10^{-3} to 4.5x10^{-3} which corresponds to the target parameters to maximise conversion efficiency and fibre mode overlap at single-mode operation. We don't want to go lower than 40nm as this results in a sharp drop off in refractive index change. Nominal fabrication parameters of 40nm Zn deposited, and an indiffusion temperature of 900°C were used.

A starting design with ridge widths of 5-7µm were chosen, based on the normalised guiding index in Figure 4.11 showing no guidance below 5µm, and Figure 5.1 highlighting the narrow set of refractive index profile values for which achieving single-mode operation in a 7µm ridge is possible. The wafer was poled with 10 periods ranging from 6.0µm to 6.9µm, calculated from the modelled effective indices, for 1st-order 1064nm SHG phasematching and 3rd-order 780nm SHG phasematching. After fabrication, the measured Zn deposition was 47nm, and prism coupling measurements at 532nm confirmed a refractive index change range of δn=0.0044-0.0048 and σ=4.4-4.8µm.

5.2.1 Mode Profiling

After indiffusion, the wafer was diced to include 5 ridge waveguides between 5µm and 7µm, in 0.5 µm steps. Following the process described in Section 3.3.4, mode field diameter measurements of the diced ridges were taken at the available laser wavelength of 1041nm, and compared to model MFD values in the X and Y axes, using the calculated refractive index profile parameters, shown in Figure 5.9.

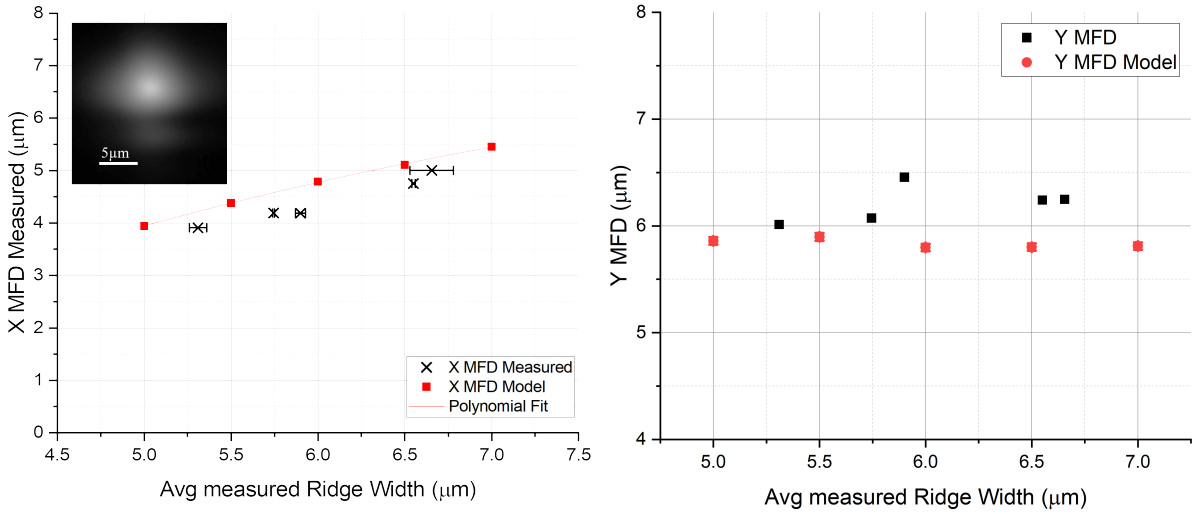

FIGURE 5.9: Mode field diameter values measured at 1041nm for wafer W163, diced with nominal ridge widths of 5-7 µm. Also plotted is the X and Y MFD values from the modelling, assuming refractive index profile parameters in the region δn=0.0044-0.0048 and σ=4.4-4.8µm, from prism coupling measurements. Inset shows the waveguide mode output at 1041nm in a 5µm wide ridge waveguide.

It can be seen that measured X MFD values follow the same trend as the model, with a small offset attributed to the method of measuring the ridge width values. The ridges are measured by focusing a x100 objective in a Leica DM microscope on the top surface of the waveguide and ridge edge positions are identified manually. The resultant ridge width value is dependent on focus and where the edge is chosen to be, resulting in ridge width discrepancies of up to 300nm at the same position. The Y MFD value trend shows a larger MFD for wider ridges, differing from the model trend where in narrower ridges the mode starts to extend downwards. The inset of Figure 5.9 shows this is due to a weak lower lobe in the mode profile of the ridges affecting the evaluation of MFD. An effort was made to preferentially launch into the fundamental mode,

but the position of the weak 1st-order vertical mode in the waveguide means it cannot be completely excluded, the 5.9µm waveguide shows how stronger coupling into that mode increases Y MFD. All the waveguides were horizontally multi-mode (1st hor MM) when launched with a 1041nm beam, extrapolating from 1064nm mode number data in Figure 5.1 at the measured refractive index profile, the observed mode profiles observed and model mode profiles concur.

5.2.2 Nonlinear Optical Characterisation

An optical test setup similar to that presented in Chapter 3 was built for nonlinear characterisation of the 1064nm SHG waveguides, as illustrated in Figure 5.10. The pump source is a fibre-coupled 1063 nm diode-pumped Nd:$GdVO_4$ laser, assembled by Dr. Gorowny Tawy. The input beam is shaped by a zoom collimator and aspheric lens mounted on a Newport 5-axis stage (M-562F-TILT-LH) to enable fine positional adjustments. The collection optics are mounted on a 3-axis stage (M-562F-XYZ) to collimate and steer the beam. The pump and SHG modes are separated by a dichroic, and the where the SHG power measured with a S120VC photodiode, which can be removed to take images of the SHG modes at different phasematching peaks with a scanning-slit beam profiler (Thorlabs BP209-VIS/M).

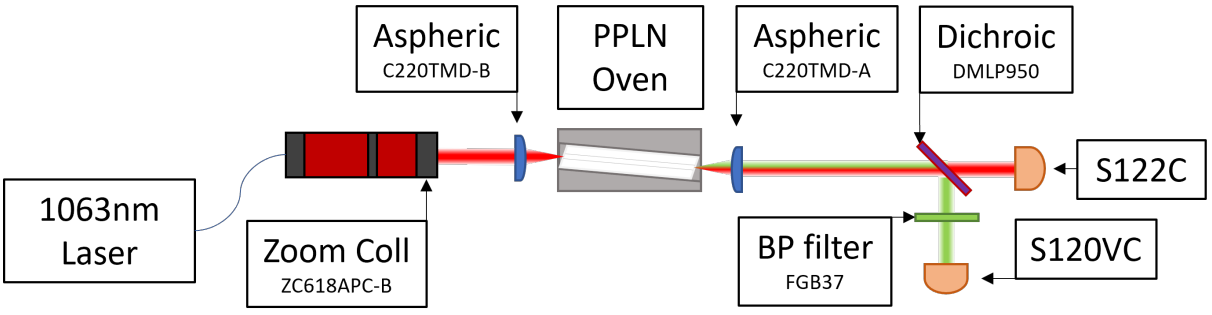

FIGURE 5.10: SHG experimental set-up. Images of the SHG mode are taken by removing the S120C detector, and using a scanning-slit beam profiler placed behind the detector.

The temperature of the oven was scanned over a range of 30-200^{o}C to find the phase-matching peak. The experimental spectrum and modes are then compared to the

model, which uses the temperature dependent refractive index equation for 5% MgO:PPLN given by Gayer [59].

Height of PM peaks in FIMMWAVE model is given by efficiency;

$$\eta = \frac{8\pi^2 d_{eff}^2 \zeta_{OV}^2}{n_{eff,pump}^2 n_{eff,shg} c\epsilon_0 \lambda_{pump}^2} \tag{5.2}$$

where $P_{SHG}=\eta P_1^2$. The modelled phasematching spectrum for a 1064nm SHG 7µm wide ridge waveguide with a poling period of Λ = 6.7 µm is provided in Figure 5.11, the initial refractive index profile parameters defined in the model were δn = 0.0046 and σ = 4.6 µm. The colour of the peaks correspond to the pump mode; blue for fundamental (TM00) and green for horizontally multimode (TM10). An image of the corresponding phasematched 532nm mode is located next to each peak. The height of the modelled peaks is proportional to the overlap integral squared, as $P_{SHG} \propto \zeta_{OV}^2$ P_{pump}^2, where P_{pump} has been normalised for all modes.

The experimental phasematching spectrum for a 1064nm SHG 7µm wide waveguide, with a poling period of Λ = 6.7 µm, is also shown in the inset of Figure 5.11, overlaid with images of the 532nm spatial mode distribution at each of the peaks. From the model, the highest conversion efficiency is expected for the fundamental 1064nm mode to fundamental 532nm mode, as it has the highest overlap integral value, however, in the experimental data it is apparent that the first order vertical mode that has the highest conversion efficiency instead. This is postulated to be due to ridge width variation along the length of the waveguide, resulting in effective index variation.

The absolute position of the peaks is expected to differ slightly between experimental and model data, due to the actual wafer refractive index differing from the Gayer refractive index model. The relative separation of the peaks is not expected to be affected by this discrepancy, but will be affected by differences in the ridge width between the model and the real waveguide. While it would be more accurate to use measured wafer refractive index values as a function of temperature in the model, there is no

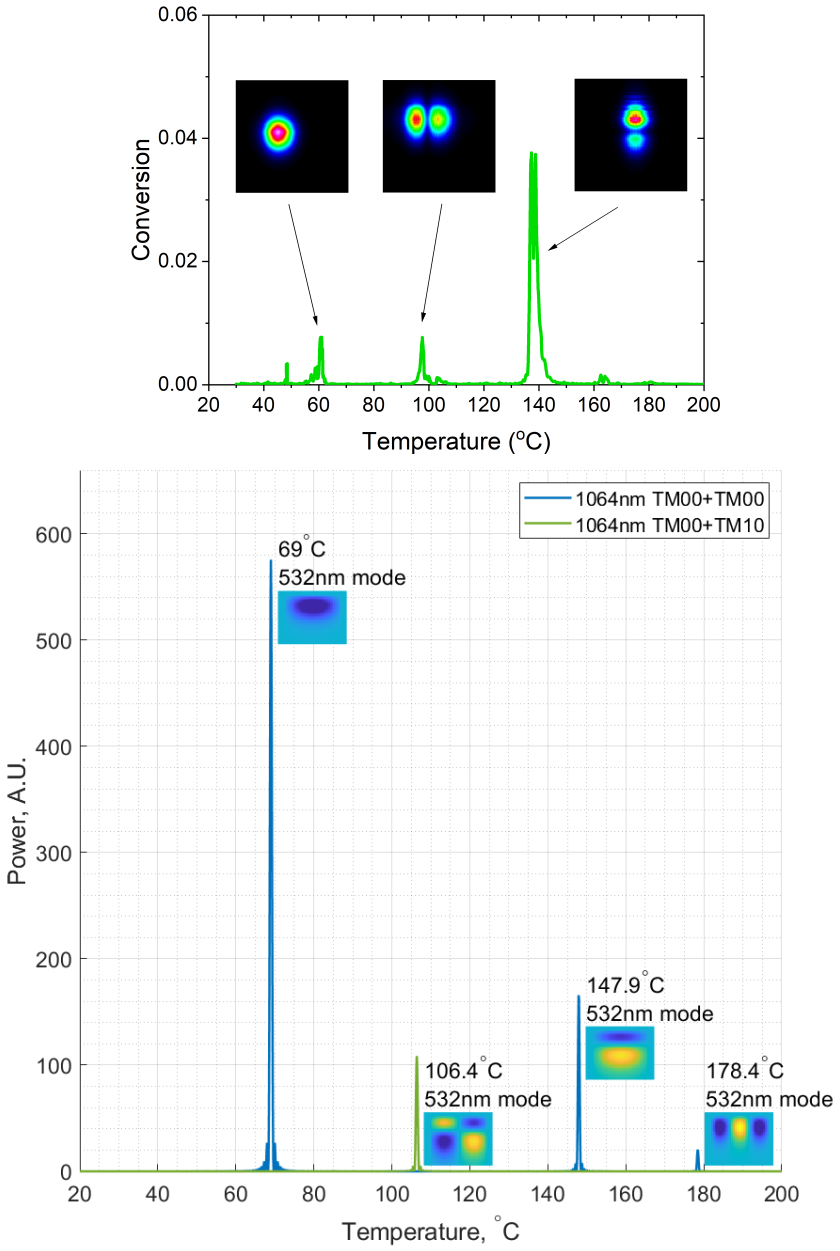

FIGURE 5.11: Temperature phasematching spectrum of a 7µm wide ridge waveguide produced by the FIMMWAVE model, peaks labelled with the corresponding phasematching; temperature and image of 532nm mode. Refractive index profile parameters for 1064nm mode and 532nm mode are δn = 4.6x10^{-3} and σ=4.6µm. Waveguide ridge width was measured close to 7µm.

temperature control capability in the Metricon prism coupler system, so we accept the shift in peak position. Additionally, an assumption is made that the absolute value of refractive index change caused by Zn diffusion into lithium niobate remains constant for the temperature range.

In the experimental waveguide phasematching data in Figure 5.11, there is a separation of 75°C between the fundamental (TM00) and 1st-order vertical (TM01) mode peaks, and 38°C between the fundamental and 1st-order horizontal (TM10) mode peak. Comparing this to the model in a 7µm wide waveguide with a poling period of Λ = 6.7 µm, the separation between the fundamental and 1st-order vertical (TM01) peak is $\sim$ 79°C, which is slightly higher than observed experimentally. Decreasing the separation between these peaks is achieve by either decreasing the refractive index change, reducing 1064nm δn relative to 532nm δn, or increasing the ridge width, so it is likely the discrepancy is a combination of these effects derived from manufacturing tolerances. The model separation between the fundamental and 1st-order horizontal (TM10) mode peak is 37°C, showing close agreement between them.

The 532nm 1st-order vertical mode having a higher conversion efficiency than the 532nm fundamental mode does not agree with the theory, we want to aim for fundamental to fundamental phasematching as it gives the highest overlap integral and therefore conversion efficiency. Modelling of the 7µm waveguide, assuming refractive index change and indiffusion depth is the same for both wavelengths, shows the overlap of the fundamental modes with current refractive index profile parameters is 33.2 µm^2, which can decrease slightly to 28.9 µm^2 by further increasing δn and σ. The 1064nm fundamental to 532nm 1st-order vertical mode is 117 µm^2. The experimental 532nm 1st-order vertical mode peak is about 4 degrees wide, which is 4 times higher than the 1°C bandwidth of the bulk sinc^2 curve. We could also be preferentially launching into the 1064nm 1st-order vertical mode observed in the mode profiling, meaning the 1064nm fundamental mode isn't carrying as much power, but this is unlikely as launch was optimised and it has not improved the conversion significantly, and this would affect both peaks.

For a preliminary insight into the effect of effective refractive index variation on phase-matching peak position, when comparing the 5.5 µm and 7 µm wide ridge phase-matching spectra in Figure 5.12, the peak position of the TM00+TM00 1064nm mode to TM00 532nm mode phasematching peak shifts by 29°C, whereas the position of the other TM00+TM00 1064nm mode to TM01 532nm mode phasematching peaks only shift by 23°C, implying the same variation in width results in a larger change in the effective propagation constant β_{eff} for the 1064nm TM00+TM00 to 532nm TM00 phase-matching peak, reducing efficiency in that interaction more.

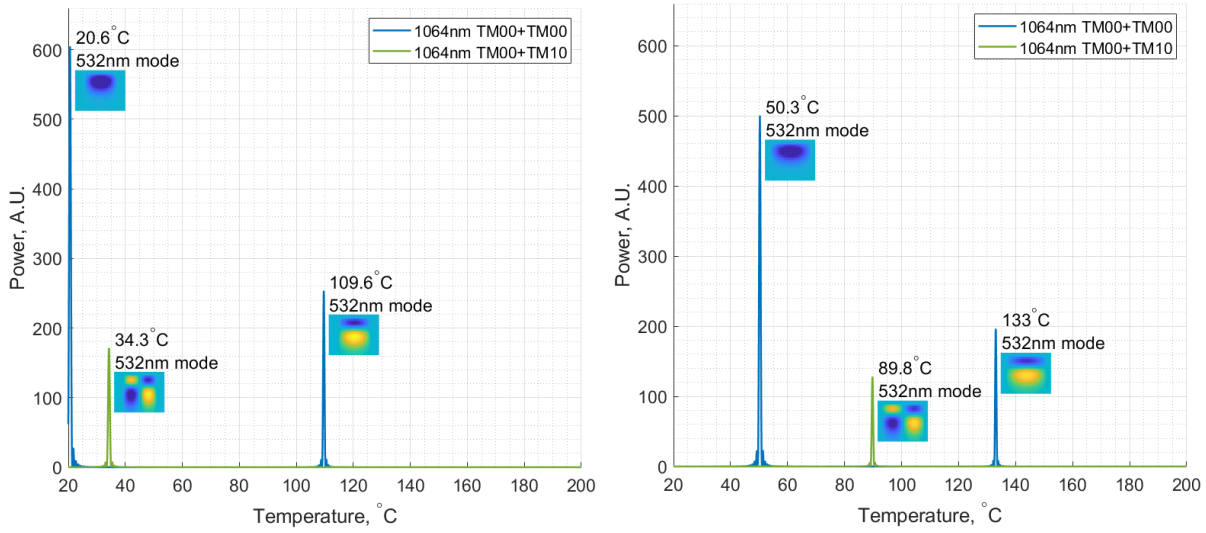

FIGURE 5.12: Modelled temperature phasematching spectrum, for waveguide ridge widths; (a) 5.5µm, (b) 7µm, with the corresponding phasematching temperature and image of 532nm mode. Refractive index profile parameters for 1064nm mode δn = 4x10^{-3} and σ=4.6µm, and 532nm mode δn = 4.6x10^{-3} and σ=4.6µm.

Additionally, variations in effective refractive index along the length of the waveguide due to variations in ridge width or zinc indiffusion uniformity will affect both the shape of the sinc^2 profile, and reduce the efficiency of the SHG conversion as shown in Figure 5.13. Through optical tests in these early samples, we also found that increasing the length of waveguides from 20 to 40mm does not achieve the expected quadratic increase in SHG efficiency, supporting the hypothesis of variations in ridge width affecting the experimental phasematching spectra.

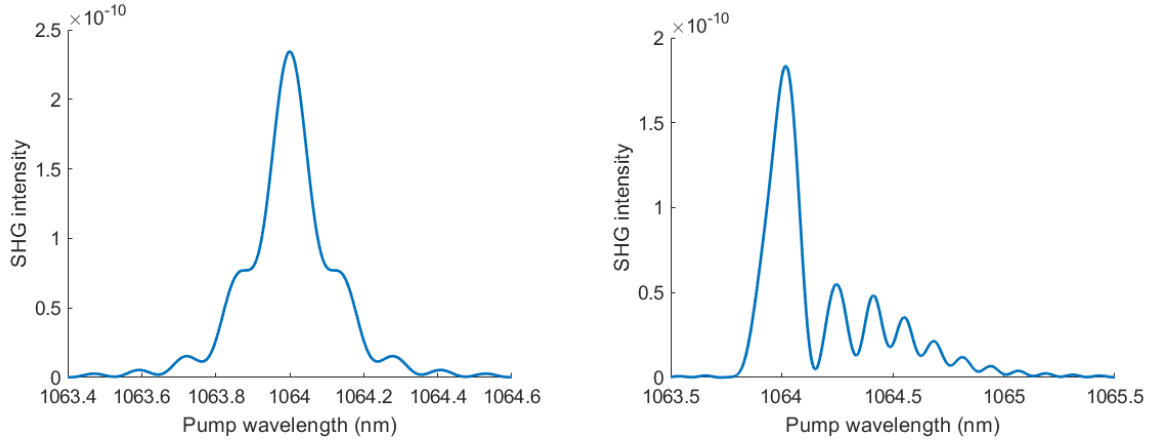

FIGURE 5.13: The phasematching curves generated by numerically solving the three photon ODEs with variable propagation constant, $\delta\beta_{eff} = \frac{2\pi(n_{eff(SHG)} - n_{eff(pump)})}{\lambda_{SHG}}$, along the length of the waveguide. Solutions where $\Delta(\delta\beta_{eff})$=500m^{-1} for; (a) a linear width variation along the waveguide length, (b) a centrally symmetric quadratic function imposed on the waveguide length.

Figure 5.14 shows the conversion efficiency, calculated as $P_{SHG}/P_{\text{pump throughput}}$, for a 7µm wide 20mm long waveguide and a 5µm wide 40mm long waveguide, fabricated with the same conditions, where the theoretical sinc^2 curve has been overlaid with the experimental data to show what the bandwidth should be. It can be seen that the 20mm long waveguide has the highest conversion. Looking at the shape of the spectra, for the 20mm long waveguide, the shape of the spectrum closely follows the theory, with only a slight asymmetry in the right-handed peak. Meanwhile spectra for the 40mm long waveguide is wider than the theoretical sinc^2 curve, and has more noise and asymmetry. This implies that there are variations in the ridge width along the waveguide. This would also explain why the 7µm wide ridge waveguide is the most efficient, contrary to model predictions, the variation in ridge width is proportionally larger in the narrow ridges, resulting in a broader spectrum/less efficient conversion.

Width variation along the length of a waveguide means reduced throughput power as the overlap of the fundamental mode changes as it propagates. Width variation also affects the propagation constant, which defines the phasematcing condition as seen in Chapter 2, therefore changes in width will set different phasematching conditions along the waveguide, reducing overall efficiency. Nonlinear overlap integral will also

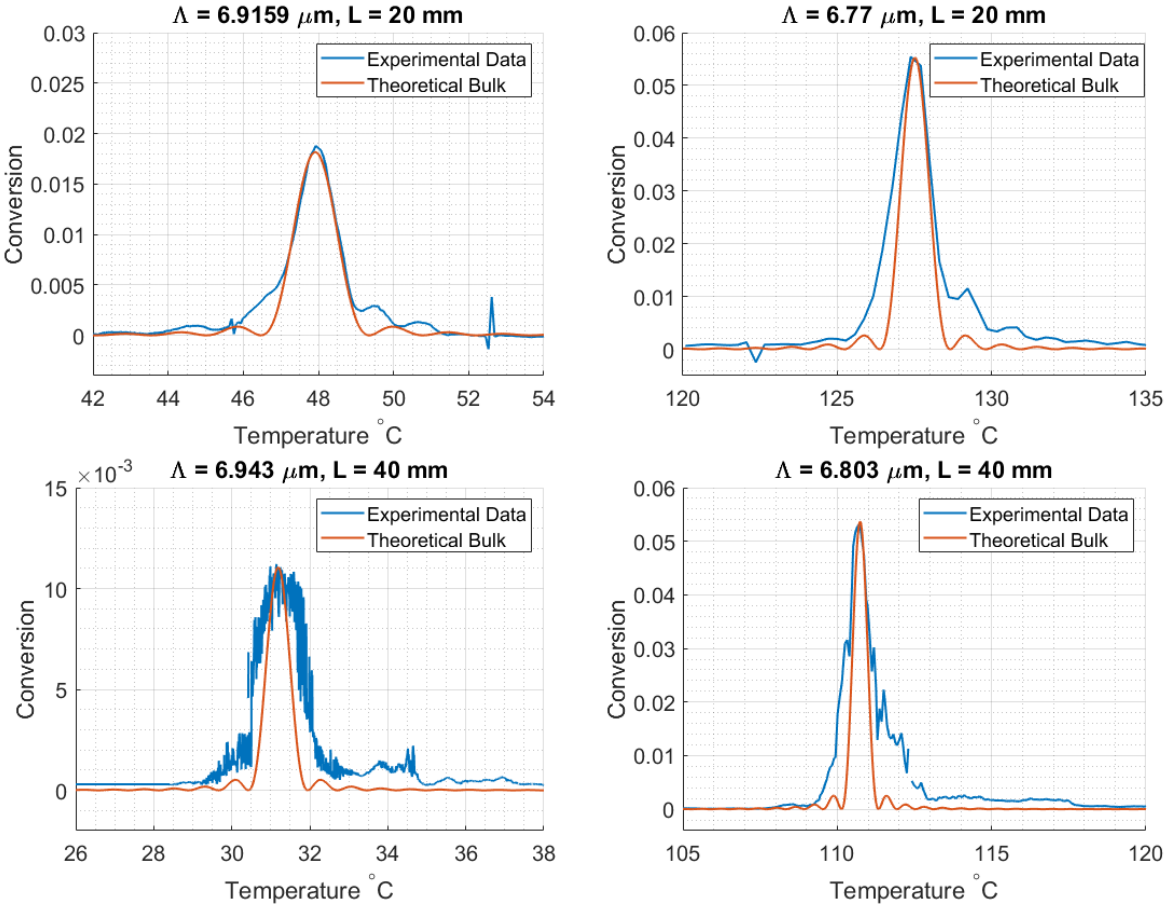

FIGURE 5.14: Temperature phasematching spectrum for; (top) 20mm long, 7μm wide waveguide, wafer W163 S9 (Λ = 6.7 μm), and (bottom) 40mm long, 5μm wide waveguide, wafer W155 S2 (Λ = 6.7 μm), both with the theoretical bulk sinc^2 spectrum overlaid, where the poling period is adjusted to fit the experimental data. The leftmost plots correspond to the fundamental to fundamental mode, while the ones on the right are for the fundamental to 1^{st}-order vertical mode.

change, affecting the total conversion efficiency but this is not expected to change the phasematching spectra shape. Width uniformity and waveguide straightness become more critical to get right for UV and short visible wavelength conversions, as the narrower ridges mean the same variation in width will result in much larger variations in the propagation constant.

5.2.3 Waveguide Width Variation

The propagation of a waveguide mode is dependent on the structure it is travelling in, with losses arising from material absorption, scattering, and coupling into lossy modes [63]. In ridge waveguides, additional sources of scattering are sidewall roughness and quality of the dicing, i.e., chipping, which has been investigated by D'Souza [102]. It is well known that variations in the propagation constant along the length of a waveguide will affect efficiency in the waveguide and phasematching spectra shape, making it an innovative tool for investigating dicing machining stability as a cause of reduction in efficiency in longer waveguides. Current machines are rated to 1µm cut straightness variation over 200 mm, before considering blade flutter and flex. It is common to use blades between 100 µm and 300 µm for dicing, but their role in waveguide width uniformity has not been fully explored yet. Xing *et al.* [103] diced ridge waveguides for 1550nm SHG using 15 µm wide blades, which resulted in a phasematching bandwidth of ~ 9°C, compared to a theoretical bandwidth of 5°C. To investigate this new devices were poled with 6.7µm, fabricated using the same 40nm zinc deposition thickness and 900°C indiffusion temperature, and diced two ridges per device, targeting a 7µm ridge width. Each waveguide was machined using diamond blades of different widths, 100µm and 300µm in an effort to reduce blade flutter and provide better width uniformity.

The waveguides were optically characterised with the same process outlined before, a fibre-coupled free-space IPG Photonics 1064.5nm laser was used as a pump source. Figure 5.15 shows a top-down image of the diced waveguides, as well as the phasematching spectra of the fundamental 1064nm SHG to fundamental 532nm mode, fitted with a theoretical sinc^2 curve. This new comparison of the temperature bandwidths, and conversion efficiencies, makes it clear that wider dicing saws provide more stability, and more uniform ridges in longer waveguides.

The waveguides were then profiled by Matt D'Souza using white-light interferometry (WLI) to measure the absolute width of the waveguides. WLI is a characterisation

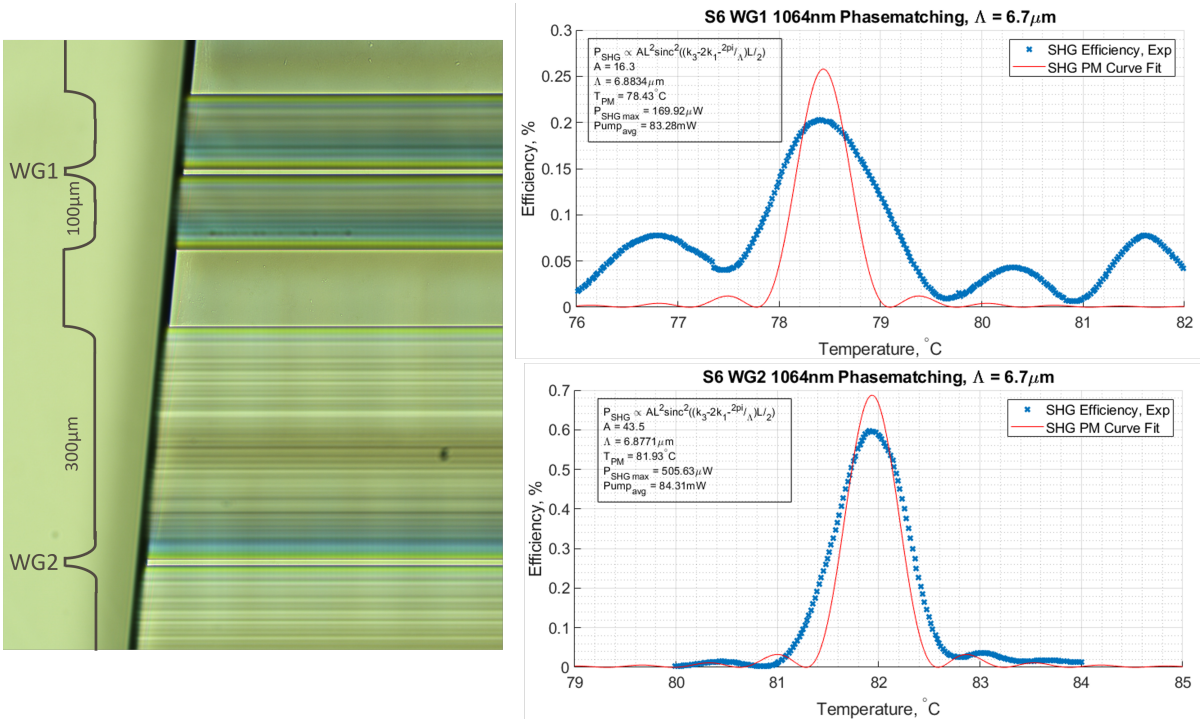

FIGURE 5.15: (left) Top view image of the diced waveguides, (right) Comparison of phasematching spectra between narrow blade dicing (top) and wide blade dicing (bottom), in the pump fundamental to SHG fundamental mode conversion peak.

technique employed to measure surface topography and roughness of samples, it is non-destructive and has no requirement for a surface coating. It uses a broadband light source with short coherence length to form an interference pattern between a reference mirror and the sample surface. The fringe pattern is generated as the path length between the sample and reference arm is altered. Further details on WLI and algorithms for analysing the fringe pattern can be found in [104, 105]. The waveguide widths provided by D'Souza were used to numerically solve the three-photon ODEs. The raw width data was first fitted with a moving average, to eliminate non-physical outlier values, and then with the lowest-order polynomial fit which would minimise residual errors. This is shown in Figure 5.16, along side the numerically solved phase-matching curve, overlaid on the experimental data.

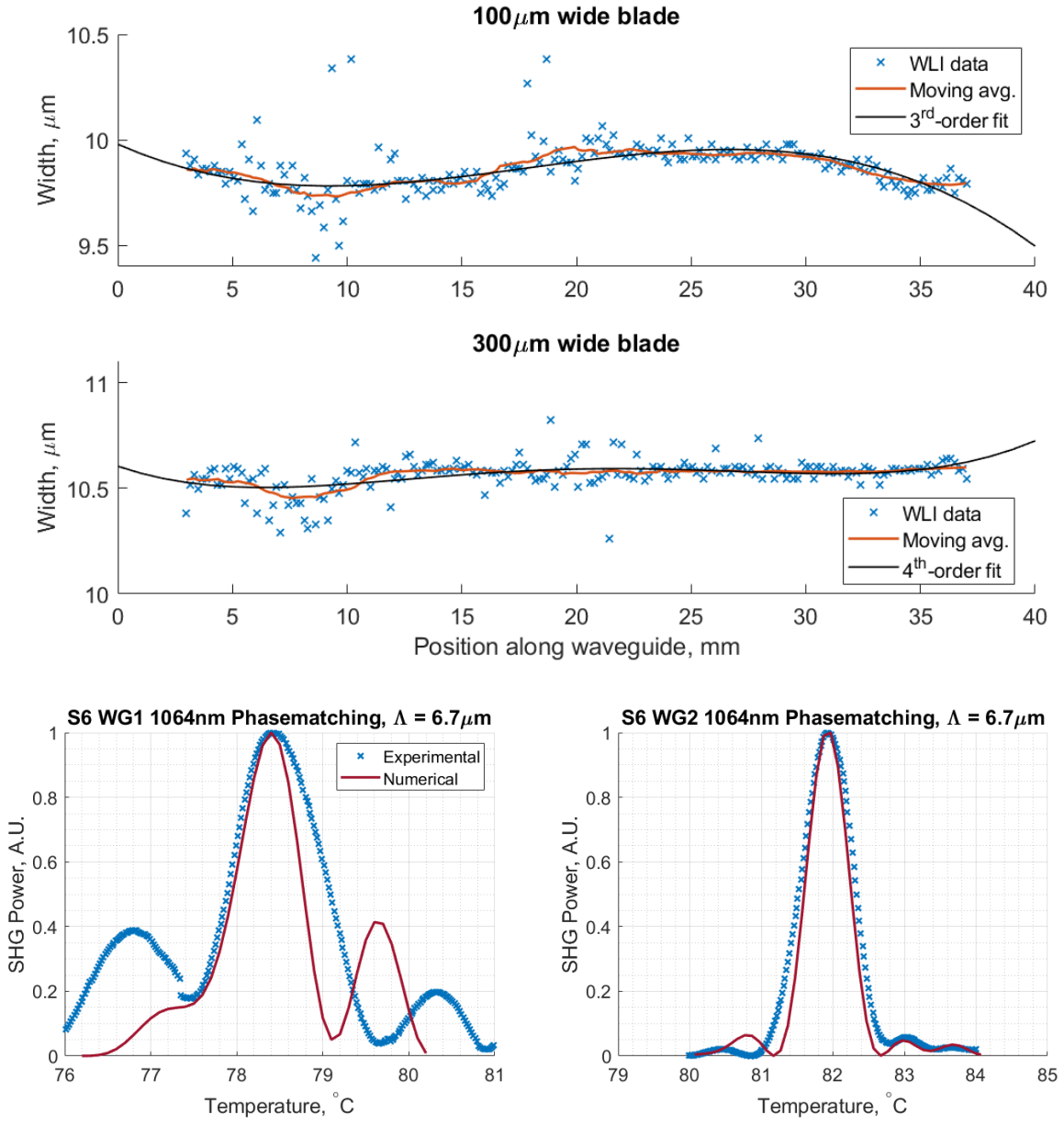

FIGURE 5.16: (top) Calculated waveguide widths from the edge detection of WLI surface profiling, measured by Matt D'Souza, overlaid with a polynomial fit to the smoothed data. (bottom) Comparison of experimental data to numerical data when solving the three photon ODEs with the width data, for waveguides diced with (left) a 100 µm wide blade, and (right) a 300 µm wide blade.

5.2.4 Power Scaling 1064nm SHG Waveguides

From the fabricated Zn-indiffused PPLN ridge waveguides for 1064nm SHG, the most efficient waveguide was found to be the 7µm wide ridge in a 20mm long waveguide with poling period Λ=6.7µm. It was characterised using the setup described in Figure 5.17.

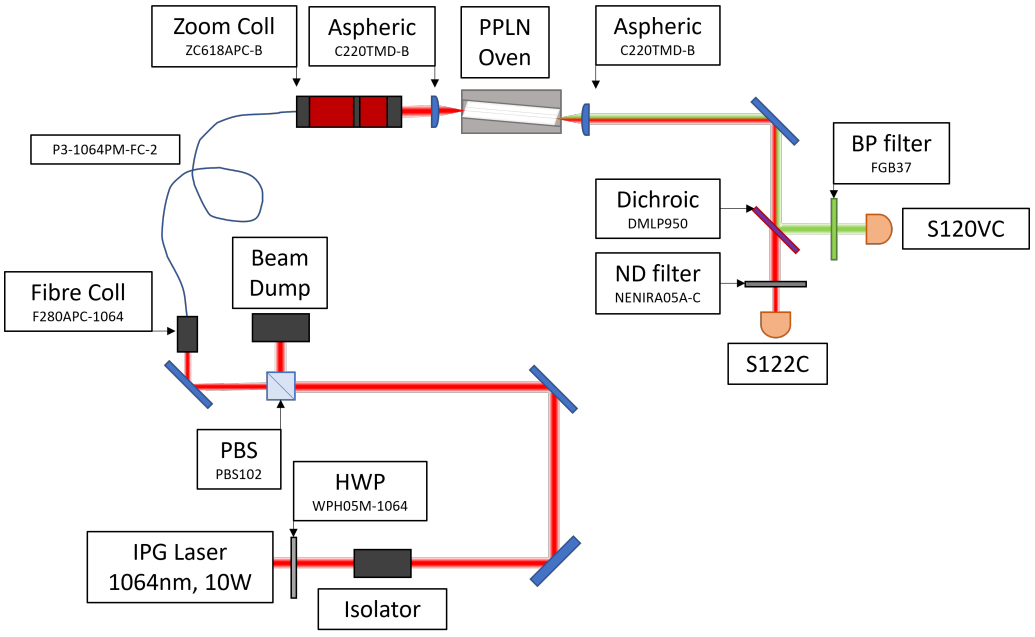

FIGURE 5.17: Diagram of optical setup used to measure 1064nm SHG efficiency in PPLN ridge waveguides. Focus of collimator adjusted to maximise SHG efficiency (typically f=12-16mm)

This waveguide generated 175mW of 532nm light, at a crystal efficiency of 37.5% and normalised conversion efficiency of 100.1%/W, Figure 5.18. Stress testing the waveguide, the highest amount of 1064nm power available to us was 2.2W, which was focused into the widest ridge, nominally 7µm wide, measured to be 6.7 µm. The throughput power measured at the output, away from phasematching, was 800mW, with no signs of facet damage. Comparatively, the 1560nm SHG PPLN waveguide tested at high powers by this group [41], a 10×8.8µm mode in a 12µm wide ridge waveguide withstood up to 4.5W of power before failing.

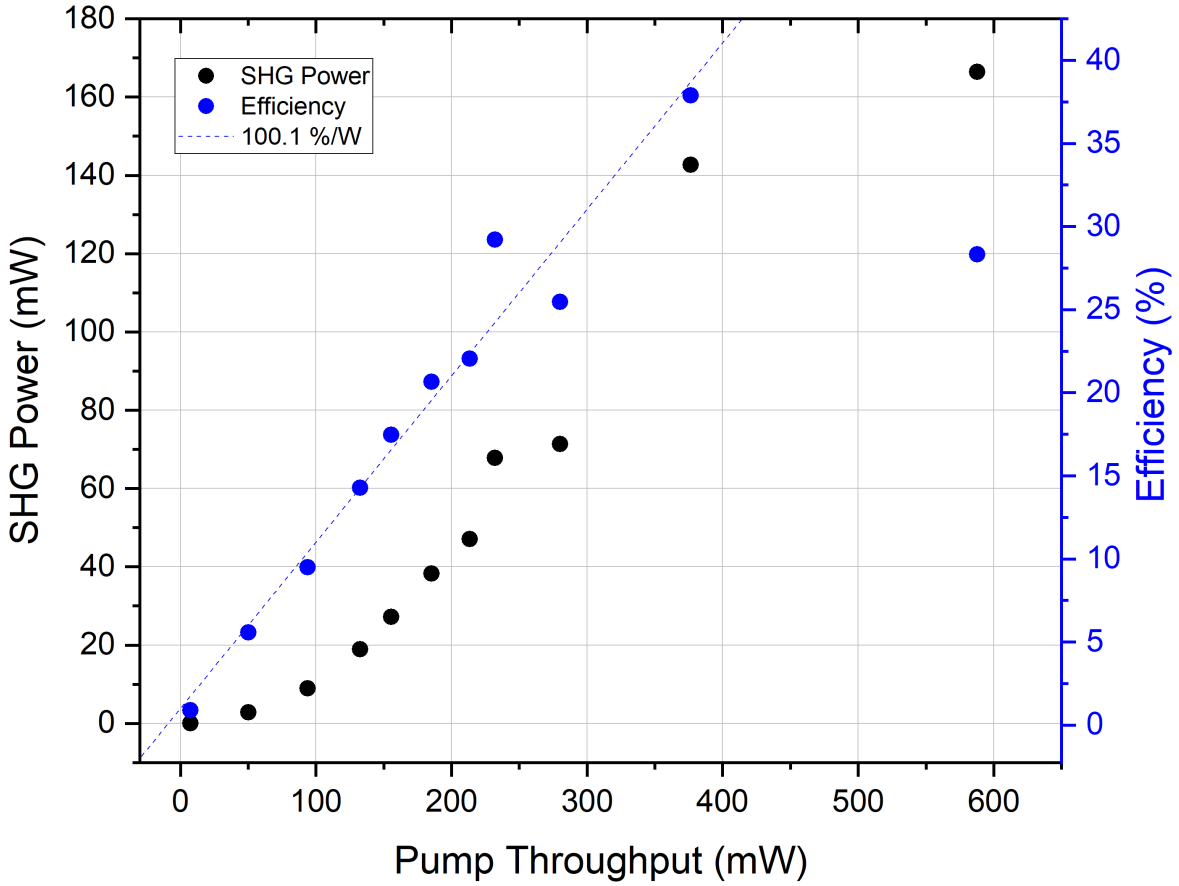

FIGURE 5.18: Graph of measured SHG power and conversion efficiency of most efficient 1064nm SHG waveguide as a function of pump power, measured at the waveguide output..

5.3 780nm SHG Waveguides

Calculations showed that first-order poling for 1064nm SHG corresponded to 780nm SHG third-order poling in zinc-indiffused PPLN ridge waveguides. A home-built temperature tunable Alexandrite laser was used to characterise the phasematching of at a range of wavelengths from ∼750 to ∼780nm, for 10mm and 20mm long waveguides. More detail on the build of the laser and some of the 780nm phasematching experiments can be found in [106]. Similar to the 1064nm SHG waveguides, the waveguides were temperature-tuned and images of the SHG modes were taken, using setup showin in Figure 5.19. As the waveguides were not optimised for single-mode 780nm support, the phasematching spectra showed many SHG modes, making it difficult to ascertain which pump modes they might've been excited by. The quality of the SHG

mode images was also not sufficient to conclusively determine which TM mode was present.

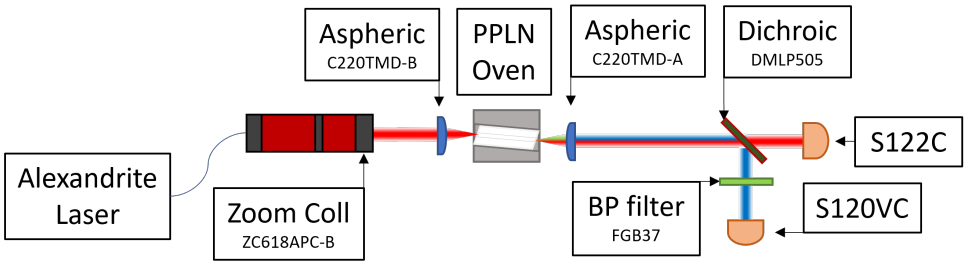

FIGURE 5.19: Diagram of the optical characterisation setup for 780nm SHG waveguide testing. Images of the SHG mode are taken by removing the S120VC detector, and using a scanning-slit beam profiler placed behind the detector.

Contrasting with the 1064nm SHG waveguides, Figure 5.20 shows the 780nm SHG waveguides did exhibit an increase in conversion efficiency when increasing the length of the waveguide, albeit not by a factor of L^2. Due to the shorter length of the waveguides, it is expected that the variation in ridge width along the length is smaller, resulting in less distortion of the $sinc^2$ profile consequent efficiency decrease.

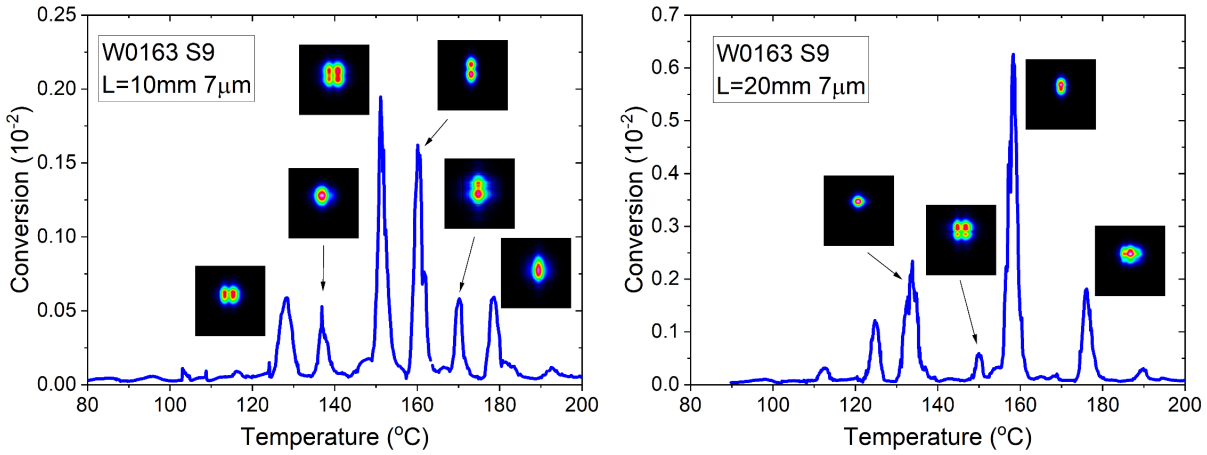

FIGURE 5.20: Phasematching spectrum for conversion comparison between (left) 10mm long, 7μm wide waveguide, wafer W163 S9 (Λ = 6.7 μm) at 776nm and (right) 20mm long, 7μm wide waveguide, W163 S9 (Λ = 6.7 μm) at 776nm. Data taken by Gorowy Tawy.

5.3.1 Power Scaling 780nm SHG Waveguides

Even though conversion efficiency might be expected to be higher in the 5µm wide waveguide, due to a tighter confinement and better overlap of the modes, the conversion efficiency was higher in the wider 7µm waveguide, likely due to the higher power handling capabilities of the wider ridges, and the quadratic dependence of efficiency on pump power. This was in a 20mm long waveguide with a 6.1µm period, where the experimental and modelled phasematching spectra can be seen in Figure 5.21. Once again it appears the most efficient SHG mode is the 1st-order vertical mode.

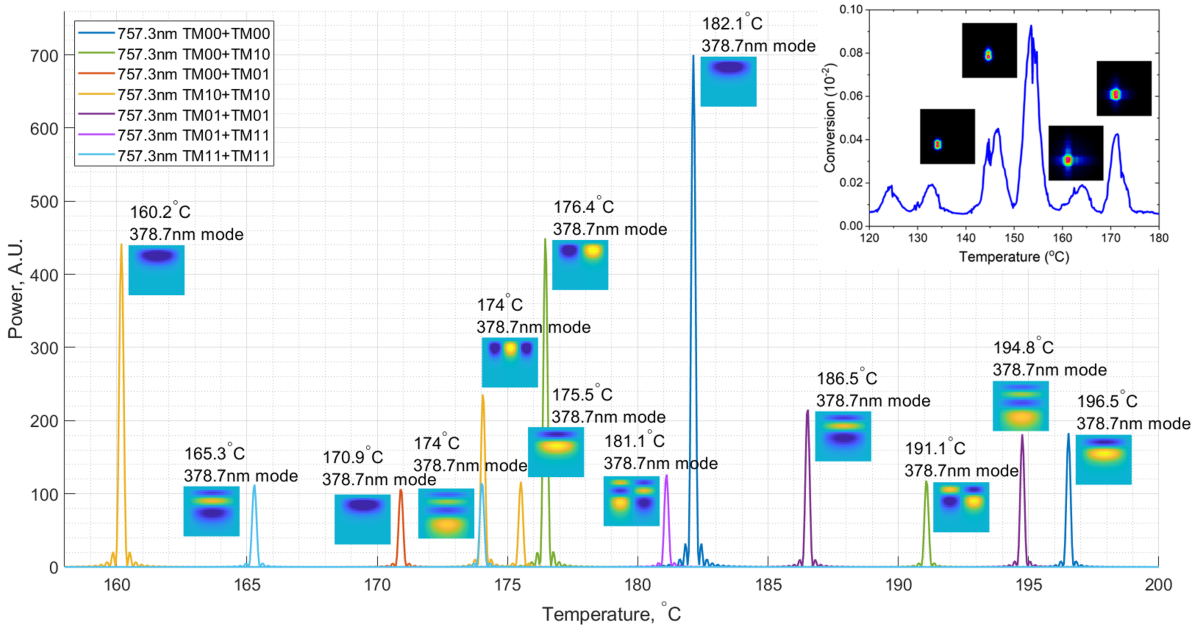

FIGURE 5.21: Temperature phasematching spectrum produced by the FIMMWAVE model, with the corresponding phasematching; temperature, 757.3nm mode and image of 378.65nm mode. Experimental phasematching data taken by Gorowy Tawy. (inset) Temperature phasematching spectrum for a 20mm long, 7µm wide waveguide in wafer W163 S6 (Λ = 6.1 µm), with images of the 378nm mode at their corresponding peaks.

Figure 5.22 shows the power test for the most efficienct waveguide. A maximum of 0.7% conversion efficiency for third-order 757.3nm SHG was found, obtaining an output power of 1.3mW with a throughput pump power of 185mW, a power level suitable for many compact ion-trap applications.

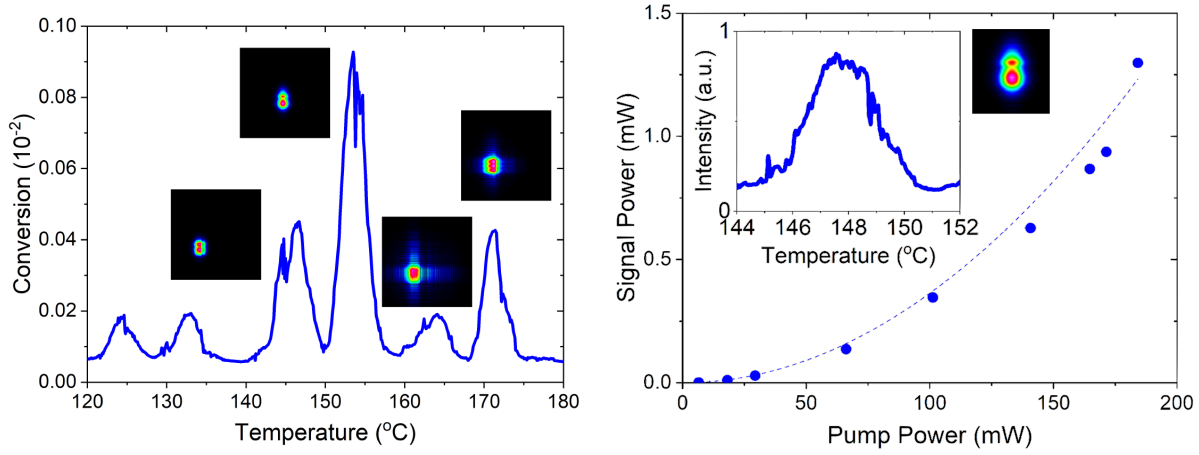

(A) (B)

FIGURE 5.22: (a) Phasematching spectrum for 20mm long, 7µm wide waveguide, W163 S6 (Λ = 6.1 µm) at 760nm. (b) Power scaling of third-order 780nm SHG waveguide. Data taken by Gorowy Tawy.

5.4 Summary

Chapter 5 investigates the design, fabrication, and characterization of PPLN waveguides for visible and NIR applications. Numerical modelling of waveguide parameters has been presented, showing conditions for single-mode operation as well as how to optimise nonlinear conversion efficiency. This is a key step in the development of high-efficiency, high-power handling Zn-indiffused PPLN ridge waveguides for visible and near infrared upconversion. New waveguides were fabricated based on modelling results, and optically characterised. Experimental results validate the numerical models presented in Chapter 4, showing strong agreement with numerical phasematching spectra. Strategies to minimize ridge width variations are explored, improving waveguide uniformity and increasing efficiency performance by threefold. Conversion efficiencies of SHG were determined, achieving up to 100.1%/W in a 1^{st}-order 1064nm SHG waveguide and 3.65%/W in a 3^{rd}-order 756.6nm SHG waveguides, both in a nominally 7 µm wide ridges. Power operation tests reveal the robustness and efficiency of these waveguides, making them suitable for applications such as optical communications and high-resolution imaging.

Chapter 6

Mid-Infrared Detection with PPLN Waveguides

The MIR region of the electromagnetic spectrum has extensive applications and use cases well documented in literature [107, 108]. It contains the absorption and emission spectral positions of numerous molecules and structures, as well as atmospheric transparency windows, making it useful in the fields of environmental monitoring [109], molecular spectroscopy [110], biomedical sensing [111], free-space communication [112], and, in future, quantum communications [113, 114]. PPLN waveguides have been used in literature for single photon detection of MIR [38], in upconversion spectrometers [14, 40], as photon pair sources for quantum communication [115, 116] and in quantum key distribution systems [35, 36, 117].

One of the early instances of using frequency conversion as a method to spectrally shift the photon into a more desirable detector range was by Boyd [118], where weak signals received by a telescope at 10 µm were upconverted through the SFG process in a Proustite crystal using a Krypton ion laser, and the signal was detected with relatively low noise photo-multipliers at visible wavelengths. The Manley–Rowe laws on photon number conservation tell us that SFG-based frequency conversion takes place

in the absence of additional coupling with vacuum states [119] and consequently in absence of spontaneous noise. Such properties are of great interest when upconverting the frequency modes of IR photons, and upconversion has already been demonstrated to overcome infrared detector limitations [120, 20]. Upconversion detection offers notable advantages over a direct IR detector, namely, high efficiency, low background noise, fast response time, and room-temperature operation.

Upconversion has been used for spectroscopy in combination with dispersive elements such as gratings [121], or the wavelength selective behaviour of the nonlinear process [122], to determine MIR spectra. It presents large potential for fast spectrometers in the wavelength range beyond the current limit set by InGaAs detectors, and has already been commercialised by NLIR [123], offering up to 2.5cm^{-1} resolution and 130kHz speeds. In the NeW-VIEUW project Covesion Ltd., Fraunhofer IPM and HighFinesse GmbH developed a spectrometer demonstrator that utilises a PPLN waveguide crystal, with a speed up to 500 Hz and $<$10 MHz accuracy.

6.1 Single Photon Detectors

Direct MIR detectors for light levels above a few µW's are thermal sensors, which are relatively cheap, but have a slow response time, and exhibit a low sensitivity and poor resolution. Semiconductor photon sensors operate in lower light regimes, they offer higher temporal bandwidths but are more expensive than thermal sensors and need to be cooled to reduce noise. Table 6.1 lists common materials for these sensors and their ranges.

Wavelength, µm	$<$0.4	0.4-1	1-3	3-5	8-14
Detector Materials	Si, GaN	Si	InGaAs, GeSi, PbS	InSb, PbSe, HgCdTe	HgCdTe

TABLE 6.1: Table listing common detector materials for the wavelength ranges shown.

In the low-light regime there also are superconducting nanowire detectors (SNSPDs) for direct MIR sensing, they have have been used in applications such as MIR LiDAR [124] thanks to their high sensitivity and fast operation, but require temperatures in the order of mK to operate, are very expensive, and not very portable. Visible single photon avalanche diodes (SPADs) and photomultiplier tubes (PMTs) have been used for detection of upconverted single photons, giving better detection efficiency at low dark-count rates, and higher count rates with better pulse-pair resolution than direct detection [125]. As previously mentioned, enhancement factors of 64 in the signal-to noise ratio have been demonstrated in upconversion detection with uncooled Si detectors with respect to direct InSb detection in the MIR [17], highlighting the advantage of up-conversion over direct detection.

For quantum information applications, efficient detection of single photons is critical. Infrared optimised APDs (usually InGaAs-InP, Ge and PbS), solid-state photomultipliers suffer from relatively low quantum efficiencies of $<$16% at 1.3µm and $<$7% at 1.55µm, high dark counts of $> 10^4 - 10^5$ counts/s and require cryogenic cooling [33]. Superconducting nanowire single photon detectors can have quantum efficiencies as high as 93%, with a dark count rate of about 1,000 counts/s around 1.55 µm [126], however for direct MIR detection efficiency drops to about 2%, while the dark count rate increases to $>$10,000 counts/s [127]. In contrast, single photon detection in the visible and NIR can be performed with silicon APDs, with detection efficiencies as high as 70% and dark counts below 25 counts/s, requiring little to no cooling.

Avalanche photodiodes (APDs) can be used as very sensitive detectors, which need less electronic signal amplification and are thus less susceptible to electronic noise. A single-photon detector emits a pulse of signal for each detected photon, they have a higher gain-voltage curve than regular photodiodes, while regular photodetectors generates a signal proportional to the photon flux. Generally silicon APDs are most suitable single photon detectors as they have low bulk dark currents. For low-light detection in the 200 nm to 1µm range, there are three basic detector choices; the silicon

PIN detector, the silicon avalanche photodiode and the photomultiplier tube (PMT). Factors to consider when looking at detectors are range, responsivity, efficiency and noise. APDs offer high speed and high sensitivity over PIN detectors, as well as a higher quantum efficiency than PMTs at wavelengths larger than 400nm.

6.2 Supporting Mid-Infrared Wavelengths

An introduced difficulty when dealing with nonlinear processes that cover a broad range of wavelengths, such as MIR to visible in this project, is the vastly different dispersion values of the the modes. This necessitates the optimization of guided modes at different wavelengths. First, the waveguide parameters needed in the model to support ~3.5µm MIR light will be investigated. This wavelength was chosen as methane has an absorption band in this region [128], and was a wavelength of interest to DSTL, who sponsored this project. Using the same waveguide shape shown in Figure 4.2, all model parameters (ridge width, δn and diffusion depth) were varied to gauge how guidance of 3.5µm modes is affected, with the previously defined normalized guide index. The findings are presented in Figure 6.1.

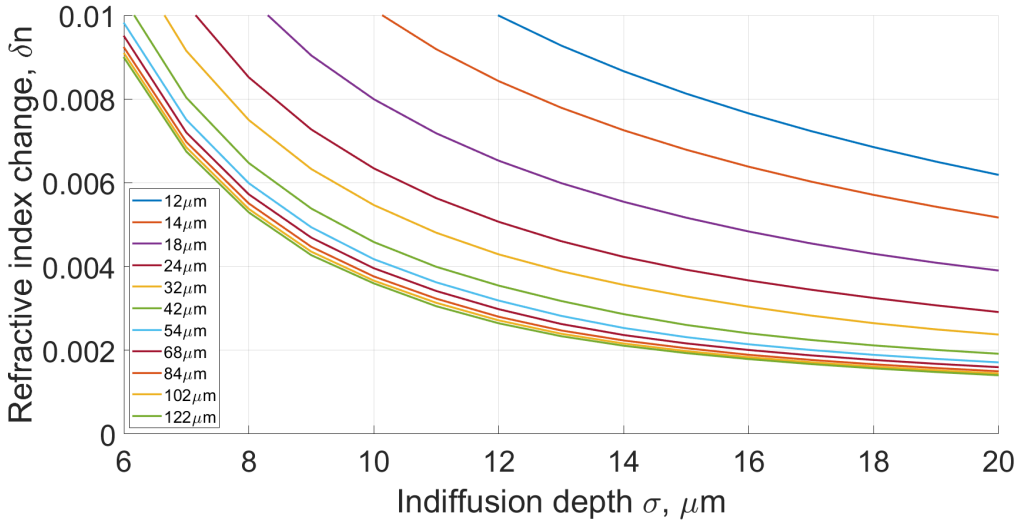

FIGURE 6.1: Refractive index difference values plotted against the indiffusion depths required for supporting a 3500nm fundamental mode for a range of waveguide ridge widths, with a normalized guide index value of b = 0.05 (weakly guiding).

First we look at increasing ridge width to increase supported wavelength, Figure 6.1 shows the refractive index change and indiffusion depth needed to weakly (b=0.05) support the fundamental mode in increasingly large ridges. Increasing ridge width after a certain point, around 50µm, has minimal impact on reducing the necessary refractive index profile parameters to support a 3.5µm fundamental mode. Inputing the approximate refractive index parameters for a standard 1560nm SHG wafer in the FIMMWAVE model (δn = 4x10^{-3}, σ=8µm at 532nm), it shows that 3.5µm modes are not supported, even by massively increasing ridge width. To increase the guidance strength up to 3.5µm the refractive index profile parameters have to be modified. The effect of changing δn and σ on the normalised guide index for a 3.5µm mode in 54µm wide waveguide is shown in Figure 6.2.

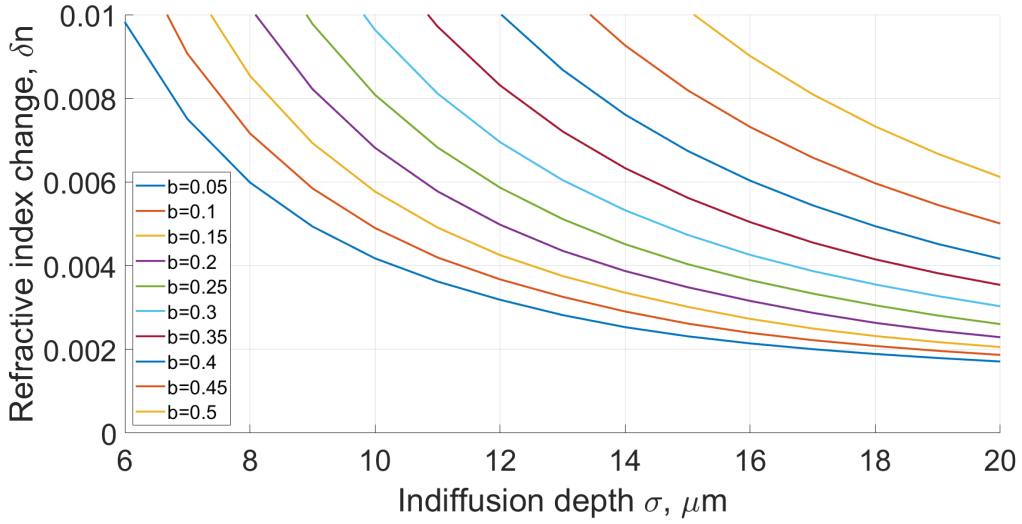

FIGURE 6.2: Refractive index difference values plotted against the indiffusion depths required for supporting a 3500nm fundamental mode for a range of normalized guide index values, with a fixed waveguide ridge width of 54µm.

At this width, both refractive index change and indiffusion depth need to increase with respect to the values for a standard 1560nm SHG waveguide. To support a weak 3.5µm mode in a 54µm wide waveguide with the same indiffusion depth as a standard 1560nm SHG waveguide, the refractive index change has to be 6·10^{-3} at 3.5µm, this index change has not yet been achieved at 532nm in our process. Increasing indiffusion depth from 8µm to 12µm halves the necessary refractive index change. Having summarised the effect of the parameters on guidance of an MIR mode in zinc-indiffused

waveguides, we will now look at how to change these parameters to support the wavelengths we want.

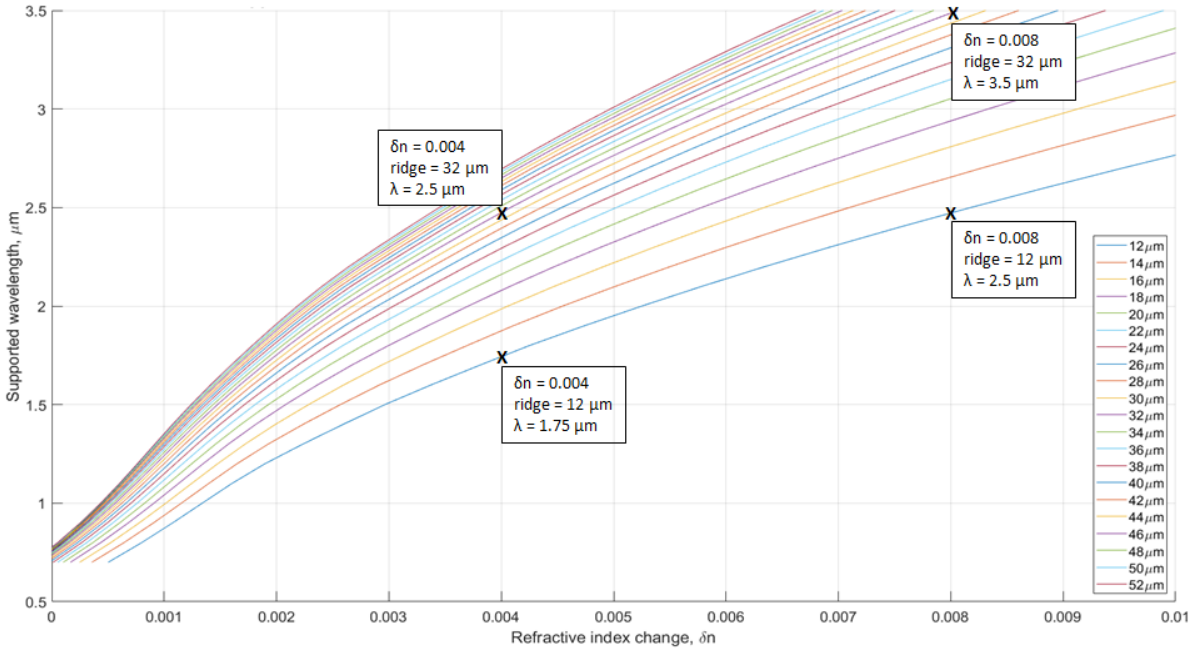

FIGURE 6.3: Supported wavelengths plotted against refractive index difference, for a normalized guide index of b = 0.05 and a fixed σ = 7.46 µm. Several points are labelled as to more easily read the trends.

To find the shortest wavelength that will be supported in a waveguide, for a set of given parameters, the normalised guide index is used as a measure. Fixing the the indiffusion depth at σ=7.46µm, from SIMS data from Section 3.3.2, the resulting values for range of the ridge widths and δn in the model were compiled and displayed graphically in Figure 6.3. These model results match the measured cut-off wavelength of 1750nm in a 12µm wide ridge in a standard 1560nm SHG waveguide with δn = 4x10^{-3}. From the graph we see how increasing the ridge width becomes less significant after reaching $\sim$ 40µm, an extra 10µm in ridge width only increasing the maximum guided wavelength by $\sim$100 nm. It can also be seen that doubling the refractive index difference has a larger impact on the supported wavelength than doubling the ridge width, which will prove useful for increasing supported wavelength while maintaining a round mode. These trends have been taken into account when designing the next prototype of MIR wavelengths. Testing these waveguides for MIR guidance has been done in conjunction with Fraunhofer.

6.2.1 MIR Waveguides

Owing to the fact the prism coupling system does not have a MIR source, direct measurements of the planar mode effective indices in zinc-diffused LN wafers is not possible. Prism coupling measurements will be taken at 532nm and the trends examined to inform new depositions. While increasing refractive index change and indiffusion depth has a larger impact on highest supported wavelength than ridge width, the zinc-indiffusion process means there is a constraint on how much the refractive index profile values can be increased before the wafer quality degrades. Temperatures above 1000°C start to degrade the poling period, and high Zn thickness depositions deteriorate the surface quality of the wafer, increasing waveguide losses. High zinc concentrations could also decrease the second-order nonlinear coefficient

In order to support longer wavelengths in Zn-indiffused PPLN waveguides, the refractive index change, indiffusion depth and ridge widths have to increase relative to the 1560nm SHG standard recipe. Based on the trend observed in Chapter 5, where shallower modes at the longer wavelength had a better nonlinear overlap integral, the greatest refractive index change that can be achieved is desirable, so zinc thickness was increased by 100nm steps to test the limitations of the process. Several wafers for MIR support were prepared with zinc depositions of 200nm, 300nm, and 400nm at 300W sputterer power and indiffused at 950°C. Results for the refractive index indiffusion profile, measured with the Metricon at 532nm, are shown in Figure 6.4, plotted alongside previous results of 300W depositions for comparison. The 300nm zinc wafer was too cloudy to take data and is missing in the graphs. From the results, it appears that refractive index change saturates above 300nm of zinc for indiffusions temperatures of 950°C.

From the wafers indiffused at 950°C, the 200nm zinc deposition thickness wafers were diced with ridge widths of 20-60µm and sent to Fraunhofer IPM for testing of supported wavelengths, as we do not have a MIR camera. The waveguides supported wavelengths of up to 2.65 µm in the widest ridge, implying a $\delta n \approx 3.6 \cdot 10^{-3}$ at this

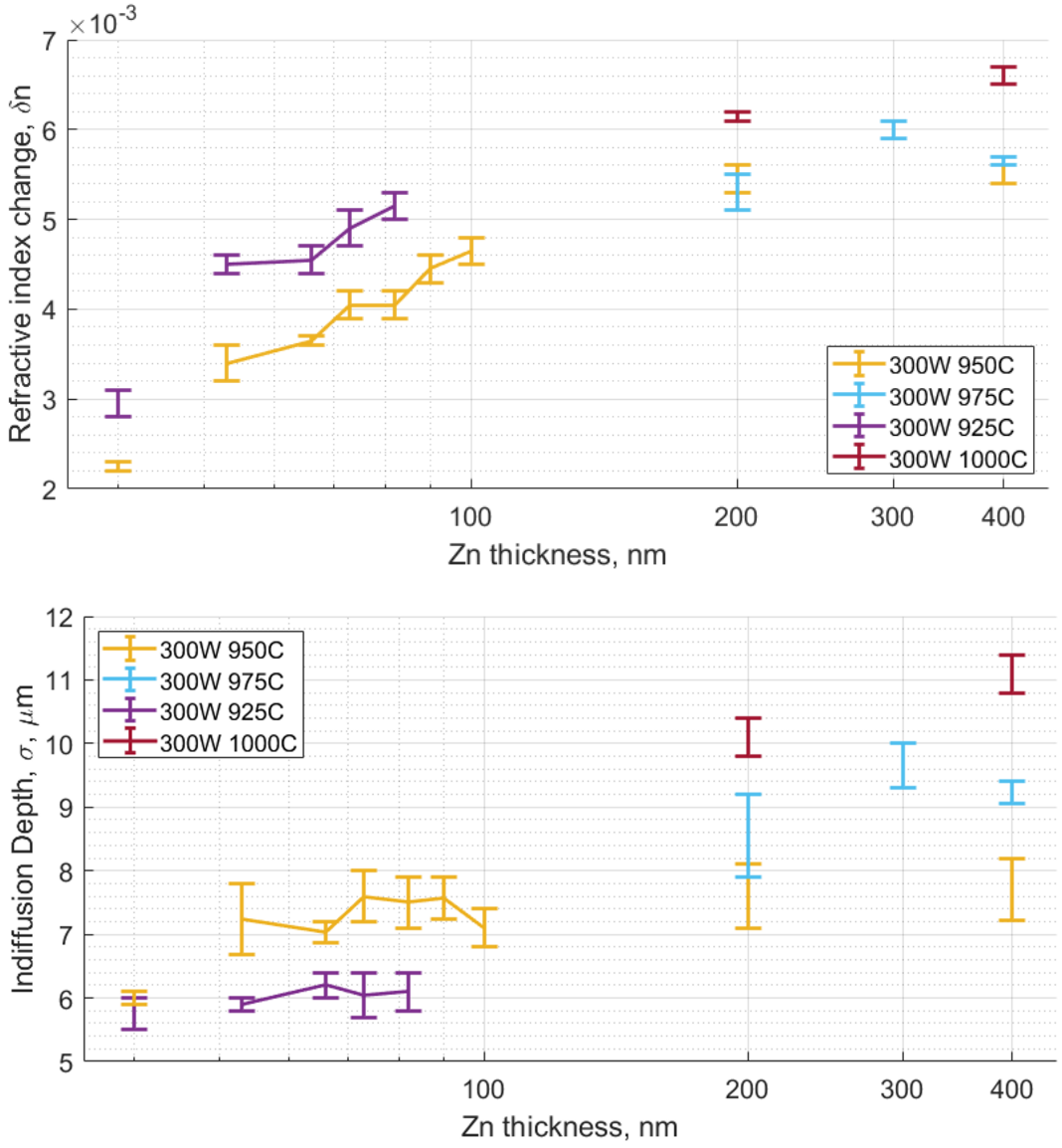

FIGURE 6.4: Modelling results of the refractive index profile based on Metricon measurements at 532nm, including thicker zinc depositions. Profile parameters plotted are refractive index difference (left), and indiffusion depth (right), against zinc thickness. For temperatures of 950^{o}C and below n_{FW}=n_{Met}± 0.0001. For temperatures of 975^{o}C and above n_{FW}=n_{Met}± 0.00015.

wavelength, extrapolated from Figure 6.3. The 300nm and 400nm zinc waveguides were were diced with wider ridges of 40µm-100µm, it was found that the 300nm of zinc waveguides supported modes better than the 400nm of zinc wavguides, so they were used for testing. The waveguides showed guidance up to 3150nm in the 60µm wide waveguide, a 500nm increase from 200nm of zinc waveguides, and up to 3300nm in the 100µm wide ridge. This follows from Figure 6.3 on the diminishing returns of increasing waveguide ridge width, where the small increase in refractive index change

from thicker zinc layer had a stronger effect than nearly doubling ridge width. Since guidance was weak further steps were taken based on model trends to increase the supported wavelength, as well as attempting to reduce the ridge width to reduce the number of horizontal modes at lower wavelengths for upconversion interactions. We are aiming to further increase the indiffusion depth, while also maintaining or increasing the refractive index change.

To investigate this, a new iteration of unpoled 5% MgO-doped lithium niobate samples were deposited with zinc thicknesses of 200nm, 300nm and 400nm at 300W sputterer power, and indiffused at higher temperatures of 975°C and 1000°C. The resulting refractive index indiffusion profile parameters are also shown in Figure 6.4, calculated from Metricon effective indices measured at 532nm. While the diffusion depth for samples indiffused at 975°C was larger than that of samples indiffused at 950°C, their refractive index change did not increase significantly when compared to samples with the same Zn deposition thickness. The samples indiffused at 1000°C show an increase in both refractive index change and indiffusion depth. The indiffusion depth is expected, increase in refractive index change could be due to the source of zinc being undepleted at the surface.

New wafers were poled and prepared with 100nm and 200nm thick zinc depositions, indiffused at 1000°C, to be tested by Fraunhofer UK. The measured highest supported wavelength and coupling efficiency in each ridge width is displayed in Table 6.2.

TABLE 6.2: Coupling efficiency of longest wavelength supported in Zn-indiffused 5% MgO-doped lithium niobate waveguide ridges, fabricated with wafers deposited with different zinc thicknesses and indiffused at 1000°C, measured by Fraunhofer CAP.

Zn Thickness	Ridge Width	Supported Wavelength
100 nm	25 µm	3300nm at 10%
	30 µm	3400nm at 15%
	35 µm	3600nm at 15%
200 nm	20 µm	3300nm at 10%
	25 µm	3400nm at 35%
	30 µm	3600nm at 20%

As we get a saturation point with increasing Zn thickness depositions, increasing refractive index change beyond a certain point ($7{\cdot}10^{-3}$ at 532nm) becomes more complex with the present indiffusion method.

6.3 MIR Waveguide Characterisation

Building on the waveguide model, structures have been designed for a prototype MIR upconversion waveguide, towards detecting single photons in the 3.5µm spectral region, by SFG of 3-3.5µm with 1064nm. A set of 40mm long Zn-indiffused PPLN waveguides were prepared with a deposited Zn thickness of 100nm and an indiffusion temperature of 1000°C, these parameters were chosen to increase aperture area while maintaining a relatively narrow ridge. The ridge widths ranged from 30-50µm in 5µm steps. They were poled with 21.7-21.9 µm periods.

These results were obtained in conjunction with Imogen Morland, at the Fraunhofer Centre for Applied Photonics (CAP) in Glasgow. An optical setup built by Fraunhofer CAP was used to characterise the waveguides for MIR SFG. The schematic and photo for this setup is shown in Figure 6.5.

The optical signal source was a Firely IR laser, a pulsed OPO tunable between 2.4 to 3.8 µm, emitting a 10ns pulse with a 150kHz repetition rate. The laser output is fibre coupled and delivered to the setup, with a maximum average power of 210mW at the output, the fibre beam is collimated and its width controlled via the telescope, to allow independent adjustment of spot size at the waveguide facet. The pump source was a Mephisto CW 1064nm laser, also fibre coupled, able to deliver up to 500mW of power. The fibre output beam is attached to a zoom collimator, enabling adjustment of the beam width. The two beams are overlapped using a dichroic mirror, and focused using an E-coated aspheric lens. The waveguide chip is placed in a regulated temperature-stable oven capable of heating up to 200°C, held at a stable temperature

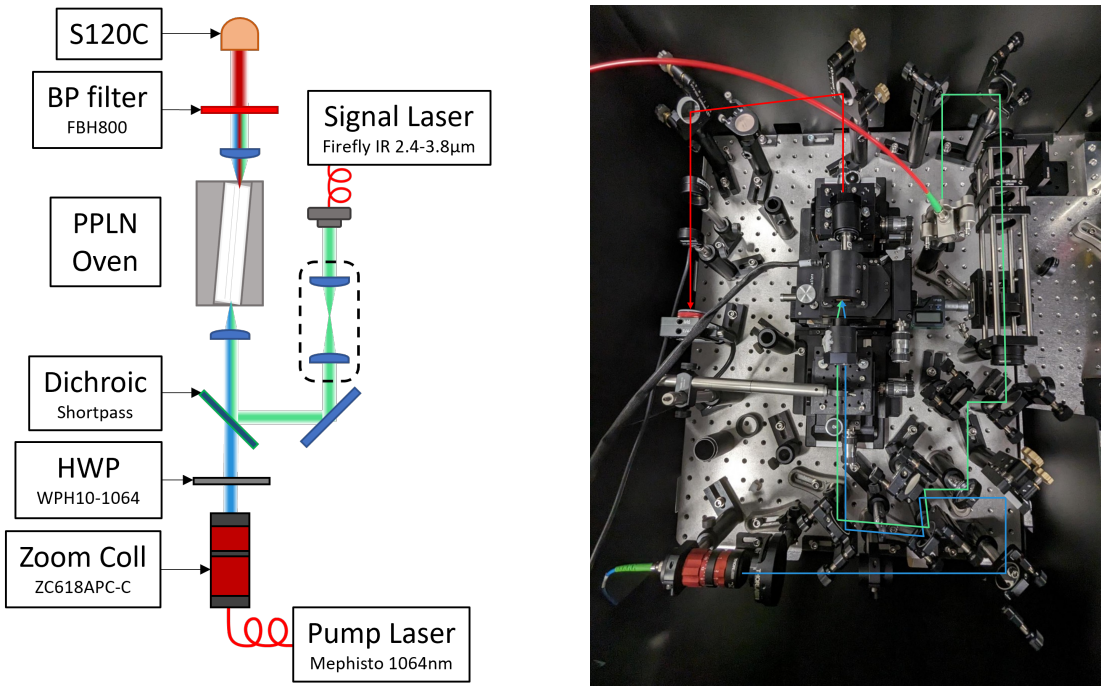

FIGURE 6.5: Diagram and photo of the setup used to characterise the MIR waveguides, built in Fraunhofer CAP by Dr. Imogen Morland.

of 40°C, which is mounted on a 3-axis stage for fine position adjustments enabling launch into a waveguide.

Through initial power measurements, it was found the 45 µm nominal ridge width waveguide offered the highest coupling efficiency of MIR light. The results presented are obtained from this waveguide. The MIR signal mode was collimated at the waveguide output with an E-coated lens and imaged with a WinCamD-IR-BB beam profiling camera. The mode field diameter can then be calculated using the lens equation $1/f = 1/v + 1/u$. A vertical MFD of 30µm was measured for wavelengths between 3.3-3.45µm in the waveguide, the 3.5µm mode had a smaller MFD of 24µm. Horizontal MFD increased linearly from 30µm at a wavelength of 3.3µm, to 32µm at a wavelength of 3.5µm. The highest coupled pump power was 7.75mW, a 4% coupling efficiency. The reason for this low coupling power becomes apparent when looking at the beam profile at 1064nm of the coupled mode, displayed in Figure 6.6.

The OPO wavelength is tuned, and the upconverted waveguide output is collimated with a C-coated lens, filtered, and imaged using a LBP2-HR-VIS2 laser beam profiler.

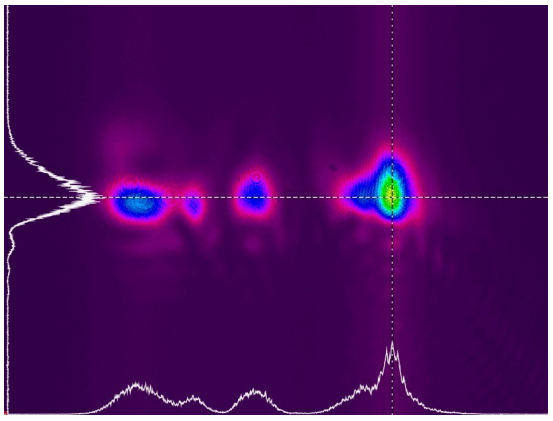

FIGURE 6.6: Beam profile of the launched 1064nm mode in a 3.5µm SFG waveguide, with nominal ridge width 45µm.

Different upconverted modes were excited as the wavelength changed, seen in Figure 6.7.

The highest conversion efficiency was at 3.3µm, the average coupled signal power was 2.4mW, a 15% coupling efficiency. The MFD in this waveguide ridge is equal in both axis, which would imply a better overlap with the fundamental fibre mode, low coupling efficiency is likely to be due to propagation loss. An average upconverted power of 0.0018mW was measured, corresponding to a 1.2mW peak power. The upconversion efficiency was calculated such that

$$\eta = \frac{P_{up}}{P_s} \cdot \frac{\lambda_{up}}{\lambda_s}$$

giving an upconversion efficiency η=0.11%. This waveguide efficiency was sufficient to have been used in a lab setup imaging MIR photons $\sim$2m away.

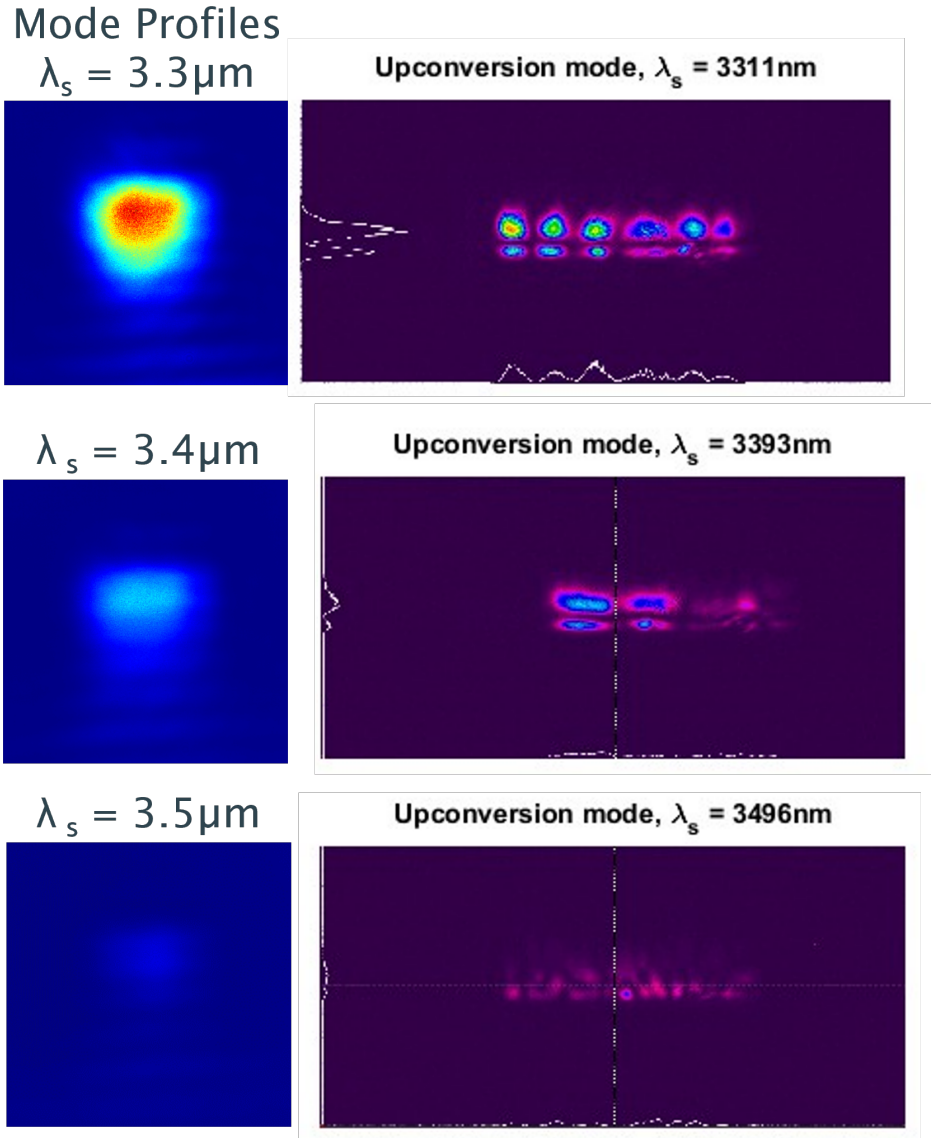

FIGURE 6.7: Mode profiles of MIR mode and the corresponding upconverted mode

6.4 Summary

Chapter 6 focuses on extending PPLN waveguide technology to the MIR wavelength range, accentuating the challenges of achieving efficient guidance and conversion. The Chapter investigates key parameters, ridge width and refractive index profiles, that influence MIR waveguide performance. Numerical modelling informs waveguide designs for MIR wavelengths, validated through experiments demonstrating guidance and upconversion detection up to 3.5 µm light with a maximum conversion efficiency of 0.11% in a pulsed regime. Recommendations for future work include optimizing fabrication parameters and exploring alternative routes to enhance refractive index changes, paving the way for more efficient MIR detection systems.

Chapter 7

Upconversion Imaging with PPLN Waveguides

Imaging systems are used to collect information from local and remote targets using specific or a range of wavelengths. It is a useful non-invasive and non-damaging detection and ranging method to determine object characteristics. Imaging in the MIR is of interest as many organic compounds have absorption bands in that range, it allows for visualisation through scattering media, and imaging for medical diagnosis [129]. The majority of upconversion imaging systems presented in literature have implemented bulk crystals as their nonlinear medium for frequency conversion. The FOV in a bulk nonlinear crystal is limited by the size of the crystal and phasematching requirement, upconverted light will only be produced at the angle where the interaction is phasematched. Thus, most reported upconversion imaging techniques rely on angle tuning [10], temperature tuning [20], broadband pump illumination [130], or more recently, chirped poling [22] to obtain a wider field of view.

Upconversion imaging cannot be done in the same way with single-mode (SM) waveguides, as the image information in the Fourier plane where the nonlinear crystal is placed, would be lost when coupling into the fundamental waveguide mode. Instead raster-scanning is used to cover the field of view in waveguide imaging systems, by

either steering the incident and collection beams or moving the object to scan it. While using SM waveguides can lengthen image collection time, there are several advantages to using a raster-scanning system; an arbitrary large object can be scanned, collinear interaction is possible, which enhances the detection efficiency for the full image, as opposed to more traditional non-collinear imaging setups, and laser power can be focused on each point at a time, so a high signal-to-noise can typically be obtained [56].

Employing PPLN waveguides for upconversion imaging is less common than bulk crystals, and most publications work around 1560nm, where waveguides with high conversion efficiencies are commercially available. Several 3D imaging systems have been demonstrated which mix ps pulses of 1554.1nm (probe) + 1565.5nm (pump) with a total system detection efficiency measured to be 3.6%, and a dark count of 250cps [131] obtaining 2400 pixels in 72 seconds. Chen *et al.* incorporated a deep-learning algorithm to reduce image aquisition time to 1µs, possible due to the noise tolerance capability of an upconversion imager [132]. PPLN waveguides have also been used in non-line-of-sight imaging [133, 134]. Fraunhofer CAP have presented work on upconversion imaging of wavelengths longer than 1560nm using PPLN waveguides provided by Covesion Ltd., developed using the work contained in this thesis. First, illumination at 1795nm upconverted to 780nm, they obtained a depth profile with a 10ns pulse so 3m depth resolution [135]. Using that previously developed system and a waveguide from the same wafer as that characterised in Chapter 6, they presented a 2D image upconverted from ∼3.3µm to ∼800nm [136].

This Chapter will present current progress towards using PPLN waveguides to upconvert MIR light in an imaging system, developing the process to integrate working MIR waveguides later on, allowing higher detection sensitivity at longer wavelengths. As long-wavelength waveguides are in the early stages of development and are nor fully optimised, they have a relative low efficiency, and we will therefore be working in a low-light regime. This will also allow for other low-light applications later on. The group also has a wider collaboration with the quantum imaging community via

the EPSRC QuantIC Hub for Quantum-Enhanced Imaging, where our role is in developing upconversion-enhanced imaging at the single photon level. Due to this we have chosen to go the route of single photon detection. For the purpose of these low-light applications, such as low-light imaging and heralded sources, a 4-channel silicon (Si) single photon detector (Excelitas SPCM-AQ4C) was initially acquired and characterised, this work has been done with the support of Dr. Paolo L. Mennea. To characterise single photon counting statistics, and conversion efficiency measurements of the detectors we will be using the well-established 1560nm SHG packaged PPLN waveguides supplied by Covesion. We have then done preliminary demonstrations of upconversion detection with the waveguide in a raster-scanning imaging format, obtaining SHG and SFG images. A 16-channel superconducting nanowire single-photon detector (SNSPD) was acquired with detection capability at 1550nm, 1064nm and 850nm.

7.1 Upconversion Detection

As part of this project an array of Excelitas detectors were purchased and assembled, as seen in Figure 7.1. They are connected to an Field Programmable Gate Array (FPGA) development board (DE2-115), which in turn communicates with a computer, and links to LabVIEW software developed in conjunction with Dr. Paolo Mennea to process information from the data packages received. To verify it was in working order, a 2MHz pulse train, corresponding to the maximum expected count rate during operation, was connected to each of the detector inputs in turn, and the expected number of counts was successfully retrieved.

Initially, an SHG process is used to upconvert photons from the imaging system, using a commercially available Covesion packaged 1560nm SHG PPLN waveguide. The SPAD detectors were used to characterise the SFG nonlinear conversion efficiency in the PPLN waveguide package, at the light levels expected from the system. This was done by mixing 1590nm and 1534.5nm light, that will be used in the imaging system

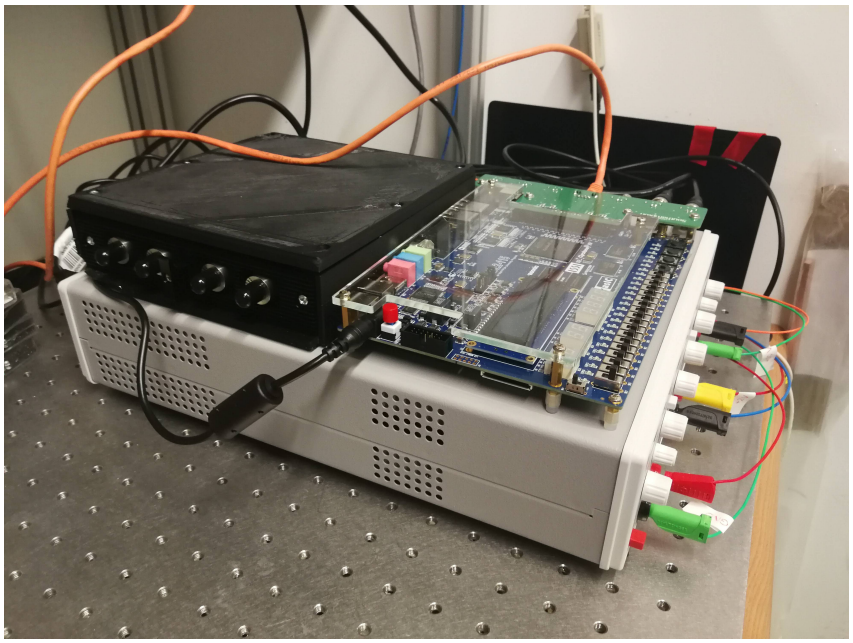

FIGURE 7.1: Picture of the Excelitas 4-channel single photon detector, in a 3D printed casing (top left), the FPGA board to communicate between the detector and the computer (top right), and the power supply to the Excelitas detector (bottom).

configuration later on, and measuring the relationship between the detector's count rate and the pump power (1590nm) supplied. It can be seen in Figure 7.2 that there are 3 different gain processes. The initial linear relationship is as expected for the SFG process, where the upconverted photons scale linearly with pump power. At $\sim$0 dBm, the steeper gradient is attributed to the output of the EDFA changing with current, generating amplified spontaneous emission (ASE) at 1534nm. Past that, the precise noise process increasing the expected linear relationship is not known. Noise in upconversion detection typically arises from spontaneous parametric down conversion (SPDC) and spontaneous Raman scattering (SRS) when the strong pump goes through the waveguide. Several works have demonstrated that a long wave pump can suppress both spontaneous processes without dramatically reducing the detection efficiency [137, 138], which is why those SFG wavelengths were chosen. A further investigation into noise processes at high powers would need to be carried out, but we are not expecting to pump at those powers.

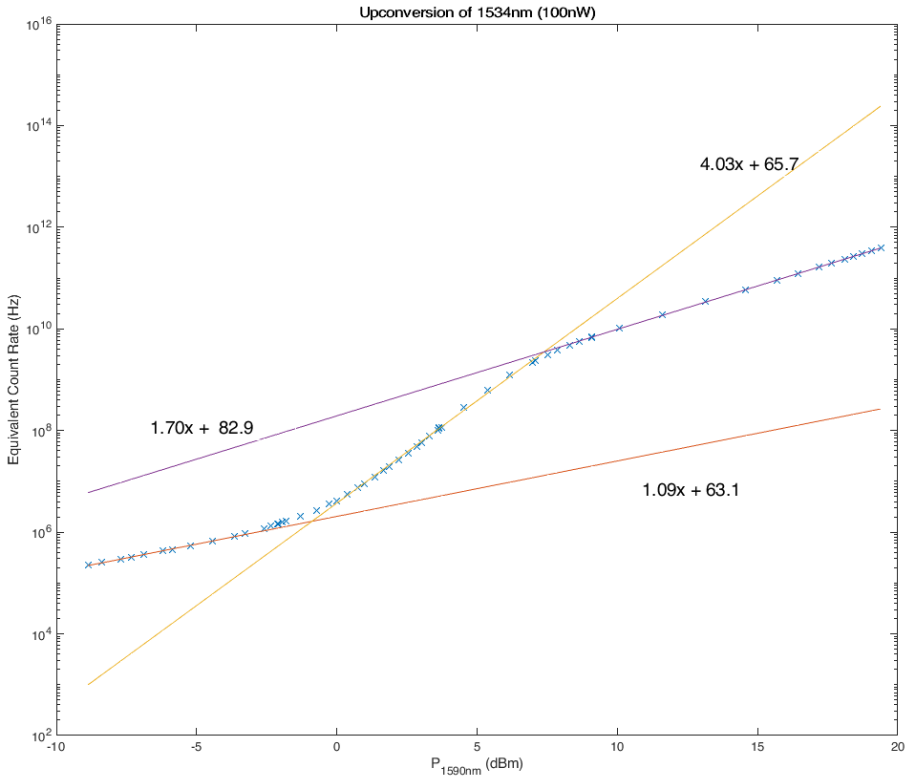

FIGURE 7.2: Count rate of the ≈780nm photons generated by the SFG process and detected by the Excelitas SPCM-AQ4C detector, where the 1590nm Agilent pump power is amplified with an EDFA, with no filtering, introducing noise to the counts. The inset shows upconversion process pumped directly with the Agilent at 1590nm (narrowband). Data taken by Dr. Paolo Mennea.

7.1.1 Direct Imaging at Visible and Telecom Wavelengths

Having no previous experience of building a laser-based remote imaging system, the initial imaging experiment for this project was designed for use at visible wavelengths, with a lock-in amplifier (LIA) to boost the detected signal. It was found the setup was very sensitive to alignment, lens position, and beam collimation. For the image collection, LabVIEW code was written in conjunction with Dr. Paolo Mennea, to control the raster-scan of the 2-axis Galvo mirrors with a data acquisition card (DAQ), and was scanned across an image of a cross in the visible imaging setup, and a regular check pattern in the NIR imaging setup. I developed the LIA parameter sweep and data collection aspect of the LabVIEW code. Images when first setting up the system were difficult to obtain, as it was uncertain if the lens was focused on the image correctly

to collect sufficient backscattered light. The imaging system for collinear illumination and backscatter collection is shown schematically in Figure 7.3, this was identical to the telecom light setup, except for using a Ge detector and optical components with C-coating.

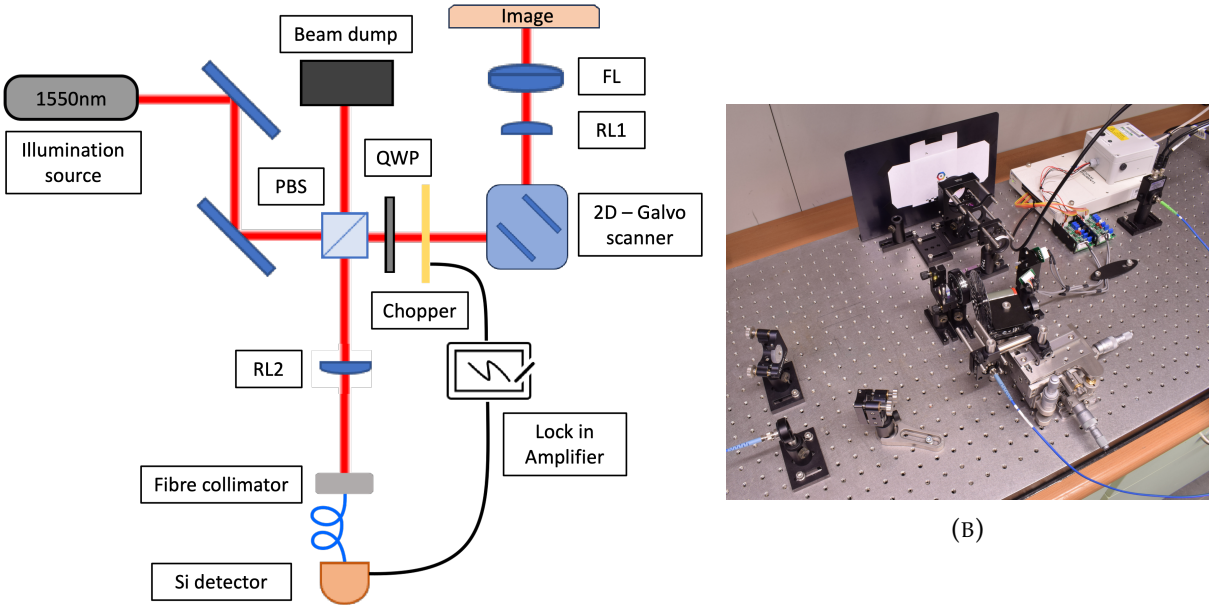

FIGURE 7.3: a) Schematic of imaging setup for visible light collection, FL: a 2" lens, with focal length 40mm was positioned in front of the image to maximise collected backscatter, b) photograph of setup.

The system was aligned by splitting the fibre coupled laser beam and back aligning from the collection optics. Getting good overlap of the two beams was key to efficient backscatter collection as the collection fibre is single mode, so has a very small aperture. A Fibre Port is used to assist in the collimation and coupling of the beam back into the fibre, to maximise the amount of collected photons. The image quality reduced drastically when the beam was not collimated properly. Initially multimode fibre was used when recording images to increase collected backscatter and confirm an image was visible, it was then swapped to single-mode polarisation-maintaining fibre. The resulting images can be seen in Figures 7.4 and 7.5, where the width of each square is 2mm. This process was then repeated for 1560nm light illumination, to verify an image was still obtained. The quality of the recorded images at 1560nm is noticeably reduced when compared to the visible light 633nm images.

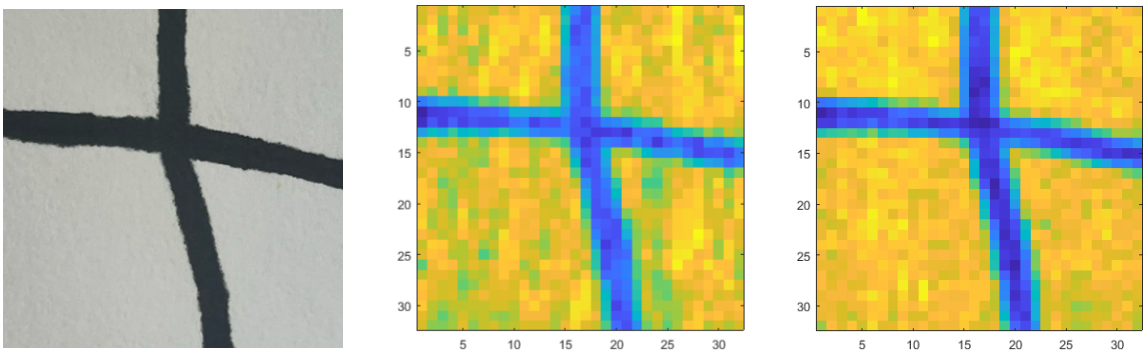

(A) (B) (C)

FIGURE 7.4: (a) photo of the target, and recorded images taken at 633nm of a check pattern, at chopper frequency 2778Hz, and phase 230°, (b) Time constant = 30.00ms (c) Time constant = 100.00ms

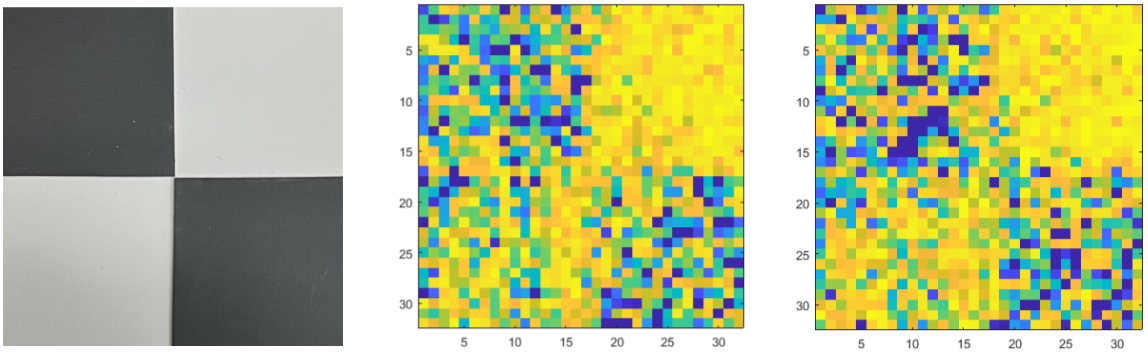

(A) (B) (C)

FIGURE 7.5: (a) photo of the target, and recorded images taken at 1560nm of a check pattern, at chopper frequency 2480Hz, and phase 50°, (b) Time constant = 30.00ms (c) Time constant = 100.00ms

7.1.2 Upconversion Imaging in 1560nm SHG Waveguides

Next, for a simple first demonstration of upconversion imaging with SHG, a commercially packaged fiber-coupled PPLN waveguide from Covesion with a system efficiency of 16% was used to switch from direct detection to upconversion for stable waveguide alignment, independent from the fibre coupled light collection point. The layout for this experiment was similar to that shown in Figure 7.3, where the Ge detector, LIA and chopper were removed, and in their place the packaged waveguide and Excelitas SPDs were connected in series to the collection fibre. Collecting upconverted 780nm images was attempted, based on the 1560nm power output from the collection

fibre, the SPDs were expected to produce an image, but no image was obtained. The collection fibre was then wound around a post to strip any fibre cladding modes, as these do not couple into the waveguide correctly and do not generate 780nm light. After stripping the cladding modes the detector was not sensitive enough to detect the produced CW 780nm light, due to the losses introduced by poor coupling of backscattered light into the collection single-mode fibre and PPLN waveguide, alongside the dependence of nonlinear efficiency on pump power.

The losses of the components are well known and taken from their specifications in the Thorlabs website, all components are anti-reflection -C coated. The lenses are positioned such that the light beam is incident at a normal to the image. The following assumptions have been made when calculating the expected scattered light at the image position. There are no specular reflections, and the back-scattered light is assumed to be polarization-independent. A Lambertian scattering model is used, as the scattering surface is assumed to be a diffused emitter. The 1560nm laser outputs up to 30mW of light, at the output facet of the Fibre Port. This light is collimated at the output of the Fibre Port, and travels the path show in Figure 7.3 to the image. The power that reaches the image is 21.4 mW with transmission and reflection losses. Using the Lambertian model, for a highly reflective spot (88.9% reflectance at 1560nm) the cone of back-scattered light that is collected by the focusing lens (FL) is 1.10µW. This beam is collimated by FL and reflected onto the Fibre Port by the polarising beam-splitter, where 880 nW reaches the fibre facet. The coupling into a single mode fibre of a non-Gaussian beam is inefficient, the losses result in approximately 440nW being collected. The low reflectance material has a reflectance of 6.4%, which results in 32nW being coupled into the fibre. These theoretical values were much larger than those collected by the system, where the light collected from bright areas was less than a nanowatt, the lower range of the power metre.

Following from the lack of an upconverted SHG image using a collinear back scattered light collection imaging system, a transmission imaging system was set up where light

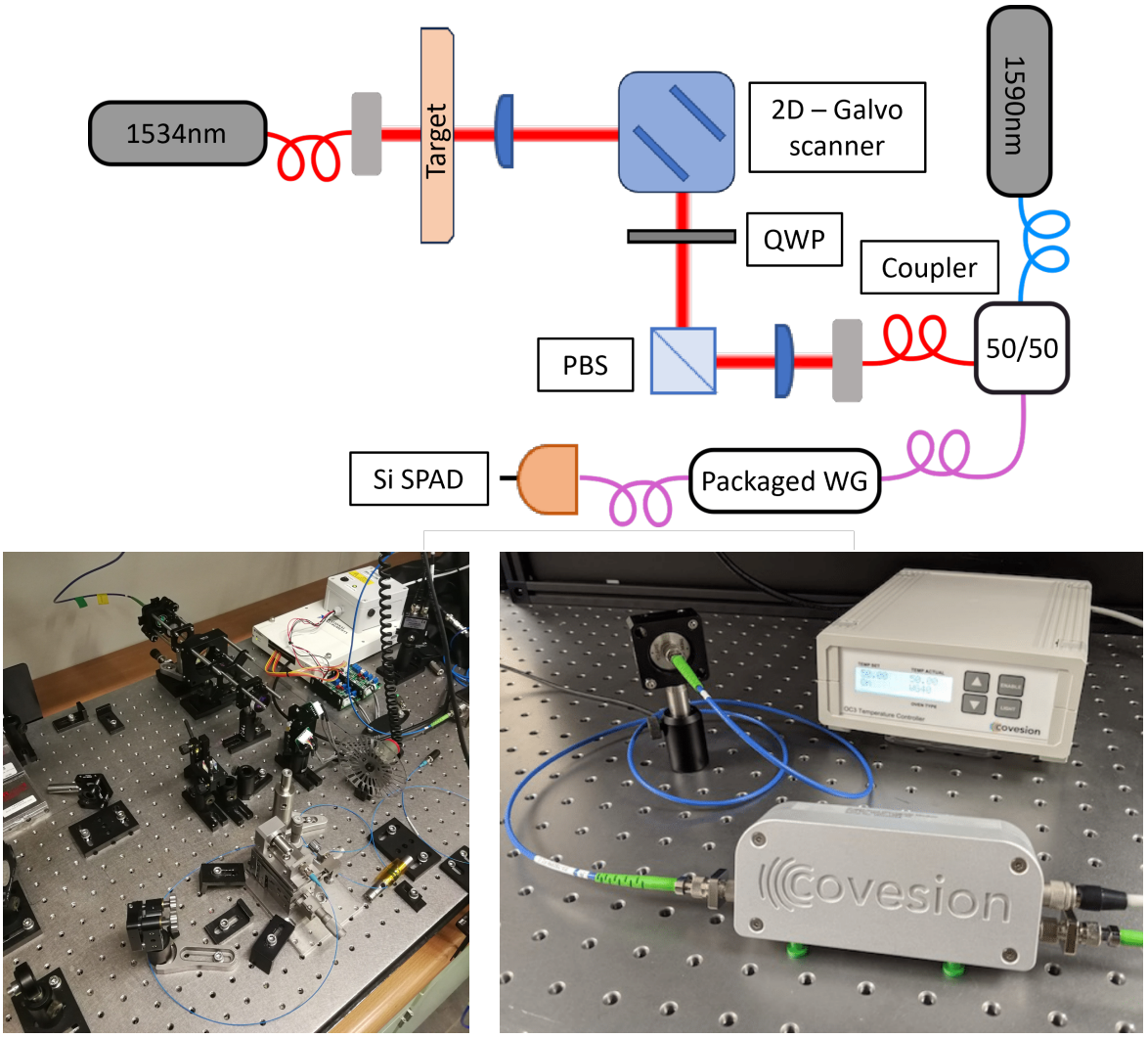

FIGURE 7.6: (a) Schematic and (b) photo for upconversion imaging system with 1550nm light and Covesion package, (c) commercially available packaged PPLN waveguide, developed for efficient watt-level SHG from 1560-780nm, with its temperature controller.

would travel through the object, to maximise the amount of photons to be collected by the system, shown in Figure 7.6. These upconversion imaging experiments align with a QuantIC project demonstration, as such, a QuantIC logo was imaged.

The imaging system in the transmission regime outputs 10-100nW of power. The laser and SPDs are now gated with an electro-optic modulator (EOM), using a 10:1 regime with the detectors to decrease the relative contribution of dark counts. The first approach to imaging with the single photon detectors was by 1560nm SHG, which recorded up to 10^4 counts/s at 780 nm, this is because it's a simple process but not

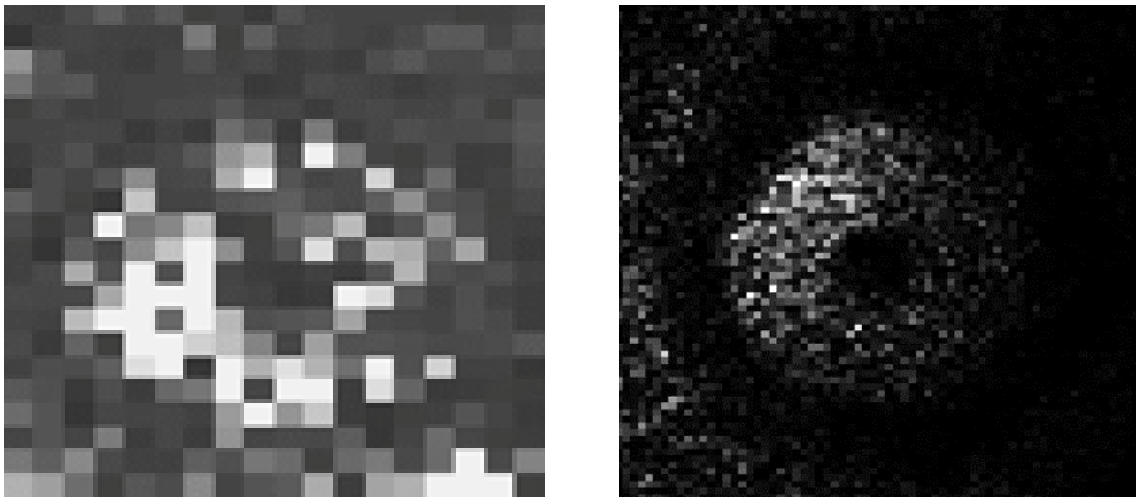

(A) (B)

FIGURE 7.7: a) Upconverted 1560nm SHG raster-scanned image, 32x32 pixels, b) upconverted 1590nm + 1534.5nm SFG raster-scanned image, 128x128 pixels, at a rate of 1px/s

very efficient in this case, as it scales quadratically to the pump power, and the imaging system only collects in the order of nanowatts of power. Following this SFG was attempted, which allows for an increase in pump power, improving the conversion efficiency. For this we were pumping with 400µW of 1590nm light, and illuminating the object with 1534.5nm light, the efficiency scales linearly with increased pump power for SFG, but in this case the power is in the order of microwatts, which recorded up to 10^6 counts/s at 780 nm. The pump can be further increased to supply several milliwatts of power, further increasing the conversion efficiency. The image generated for upconversion imaging for both these nonlinear processes can be seen in Figure 7.7.

7.1.3 Upconversion Imaging in 1950nm SFG Waveguides

The next stage was to increase the illumination wavelength, working towards the goal of using nonlinear waveguides for MIR upconversion imaging. An experiment was planned using PPLN waveguides developed for SFG of 2004nm with 1550nm, nominally designed for detection of CO_2 gas, as they offer higher conversion efficiencies than the current iteration of 3-3.5µm PPLN waveguides, and sources were available at both those wavelengths. Moreover, the proximity of the pump wavelengths reduces

the complexity of the system, as a wavelength division multiplexer (WDM) can be used to combine the two beams in fibre. However, this means the optical launch cannot be independently controlled, and the focal shift from the aspheric lens results in a non-optimal coupling efficiency of the laser beams into the waveguide.

7.1.3.1 2µm SFG Waveguide Characterisation

The nominal fabrication parameters for the 2µm SFG waveguide were a deposited Zn thickness of 200nm and an indiffusion temperature of 975°C. Based on the prism coupling measurements from the previous Chapter, the expected refractive index profile values are; a refractive index change δn=5.3$\pm$0.2 $\cdot$ 10^{-4}, and an indiffusion depth between 7.9µm and 9.2µm. Metricon measurements were taken at 532nm to compare, resulting in a calculated refractive index change δn = 4.9$\pm$0.05 $\cdot$ 10^{-4} and indiffusion depth σ = 8.4$\pm$0.2µm. Nominal ridge widths of 14-16µm, in 0.5µm steps, were diced to form the waveguides, based on the expected vertical MFD of 14.5µm at 2µm.

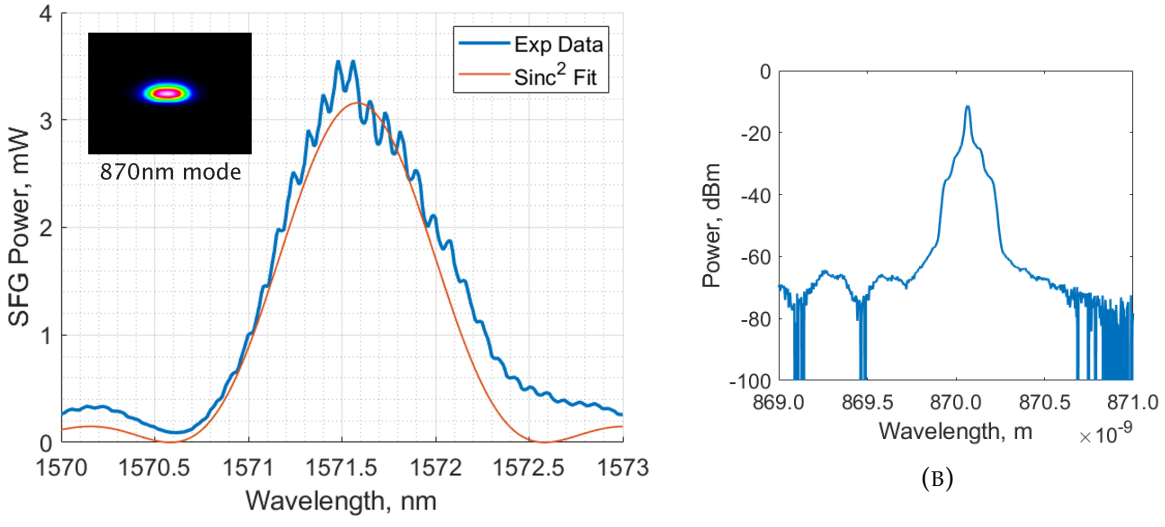

(A) (B)

FIGURE 7.8: (a) Phasematching spectra for the most efficient Zn-indiffused PPLN waveguide in a 40mm long chip. The orange line represents a theoretical sinc^2 for a bulk device the same length of the waveguide. This waveguide has a ridge width of 16µm, with a poling period of 23.5µm, and was characterised at 40°C, probed with 1950nm light and pumped with ~1560nm. (b) OSA trace of the ~870nm upconverted mode.

Optical characterisation of the 40mm long angle-cut PPLN waveguides was carried out to find the required pump wavelength. Using a similar system to that outlined in Section 3.3.5, the waveguides are characterised with a CW 1950nm thulium fibre laser and an EDFA seeded with a tunable 1560nm source combined in a WDM. The waveguide was determined to be multimode in the horizontal axis, thus to ensure maximum conversion into the fundamental upconverted mode, the launch was adjusted at the peak conversion efficiency wavelength. The resulting coupled power from the launched beams was 60mW for 1570nm and 50mW for 1950nm, approximate coupling efficiencies of 20% and 15% respectively. The highest conversion efficiency was found in the widest ridge. The waveguide was kept at a stable temperature of 40°C, and the resulting phasematching curve was found, presented in Figure 7.8, the inset shows the fundamental ∼870nm mode shape. The spectrum of the upconverted SFG mode is obtained with an optical spectrum analyser (OSA), with a peak at ∼870.1nm. The phasematching curve is fitted with the theoretical sinc^2 of bulk MgO:PPLN, and a comparison of the spectra shows good correspondence between bandwidths, indicating good quality ridges, as there are no significant broadening effects. The side-lobe's shape indicates a small parabolic width variation, as seen in Figure 5.13 from numerically solving the three-photon ODEs, and the non-zero crossing points at $\text{sinc}^2(\pm\pi)$ arise from absorption losses in the waveguide. This is because the zero crossing points occur when the generated power in the first half of the crystal is transferred back to the pump wavelength in the second half, which cannot happen if met with high absorption losses.

7.1.3.2 Direct Imaging with Pulsed 1570nm

Initially, the imaging system will be setup for illumination and direct detection at 1570nm. Recently the group has acquired a SNSPD (ID Quantique ID281) and a time-tagger (Swabian Time-Tagger X) with 16 channels; 8 channels at 1550nm, 4 channels at

1064nm, and 4 channels at 850nm, these offer high quantum efficiencies at all wavelengths (>80%), low jitter times and low dark counts. Due to the more sensitive detectors, and the available pulse modulation speeds, the imaging system was rebuilt with flood illumination, to avoid dead-time pileup and noise counts from illumination pulse back-reflection from the optics. The number of optical components in the system was decreased to further reduce losses by transmission and reflections on the interfaces. The whole image was illuminated with a collimated beam and backscattered light from the object was collected by a pair of CaF_2 relay lenses, using a Galvo mirror to raster scan across the image. The imaging setup is shown in Figure 7.9.

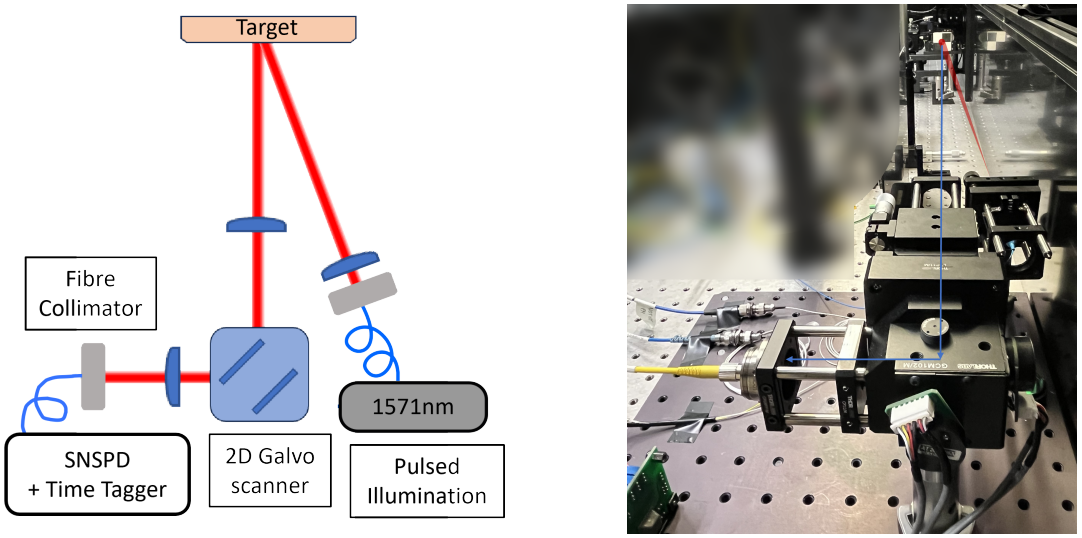

(A) (B)

FIGURE 7.9: 1571nm pulsed illumination imaging setup; (a) diagram, and (b) photo.

Pulsed operation was trialled as the waveguides will eventually be used in a 3D imaging system, an electro-optic modulator (EOM) was used to modulate the 1570nm beam of a tunable Agilent seed laser before injecting into an EDFA. A radio-frequency (RF) amplifier and bias tee were used in conjunction with a pattern generator to drive the EOM, generating 800ps long pulses with a 77.5MHz repetition rate. The existing LabVIEW programme was modified to interface with the time-tagger software and implement histogram measurements, this allows to measure time differences between received pulses for depth information. The clock output of the pattern generator was used as a start point for the histogram data acquisition.

Distance from the target to the first relay lens was ∼1m, the size of the collection spot at the target is measured by illuminating from the fibre collimator and using a knife edge technique at the focus, giving a 0.5mm spot size. The first relay lens collects a cone of light from the target, gets collimated by the second relay lens, and coupled by the Fibre Port collimator into a polarisation-maintaining fibre. The angular steps of the Galvo mirrors are small, so it is assumed no distortion occurs when passing through the first relay lens. Maximising backscattered collection was done by carefully collimating the Fibre Port output, placing the target at the focus of the first relay lens, and setting the Galvo mirrors so the beam from the Fibre Port is centred on the collection lens and normal to the target, switching back to flood illumination and using an iris to only allow light from the desired spot, the Fibre Port linear alignment was adjusted to maximise coupling. The target was raster scanned, the acquisition time for a whole image is ∼5 minutes, with photons being collected for a capture duration of 1s for each pixel. Summing the total counts over over the histogram from each pixel produces Figure 7.10.

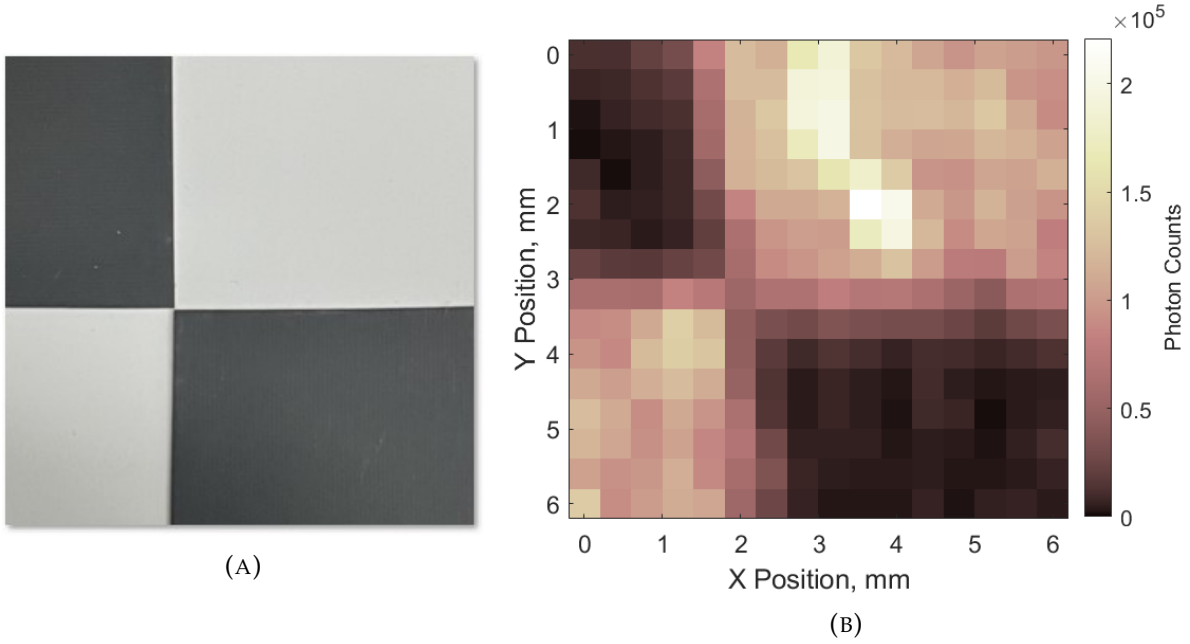

(A) (B)

FIGURE 7.10: (a) Photo of a checkerboard pattern, the illumination target, (b) raster-scanned 16x16 pixel image of a checkerboard pattern, illuminated with pulsed 1571nm light.

Image quality will be determined with contrast-to-noise (CTN) ratio, where the average dark area will be subtracted from the average bright area, then divided by the standard deviation of noise. The noise is determined by subtracting two consecutive images. The CTN ratio for Figure 7.10 is 18.4.

Figure 7.11 displays the histograms for a pixel in a bright and dark area. There are unanticipated background counts present when the pulse is expected to be off, much higher than the detector dark counts, which were 15 cps for the chosen detector channel. The EOM was checked with an oscilloscope and showed a 100:1 extinction ratio. The source of these counts has not been identified as of yet.

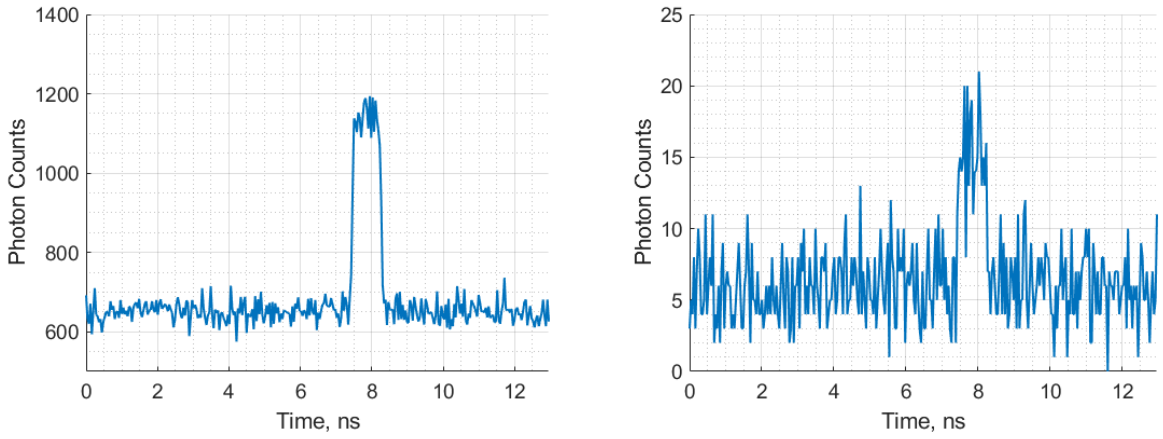

(A) (B)

FIGURE 7.11: Histogram of a single pixel in; (a) a bright area, and (b) a dark area. Total histogram collection time 1s.

7.1.3.3 CW 1950nm Upconversion Imaging

For upconversion imaging at wavelengths longer than telecommunications wavelenghts, the same setup as Figure 7.9 was used, where the pulsed illumination was swapped for a CW 1950nm source and the backscattered light collected from the Fibre Port is connected to the upconversion setup shown in Figure 7.12. The knife edge measurement was repeated, a spot size of 0.66mm was found, and the light collection re-optimised. The upconverted mode at the waveguide output was fibre-coupled to be sent to the

SNSPDs, a cylindrical lens was used to aid in the coupling due to the oval shape of the mode, an efficiency of ~30% was obtained. A narrowband bandpass filter was added after the EDFA to remove any amplified spontaneous emmission (ASE) that would contribute noise to the upconverted photon counts. The upconverted signal is passed through filtering to remove background noise.

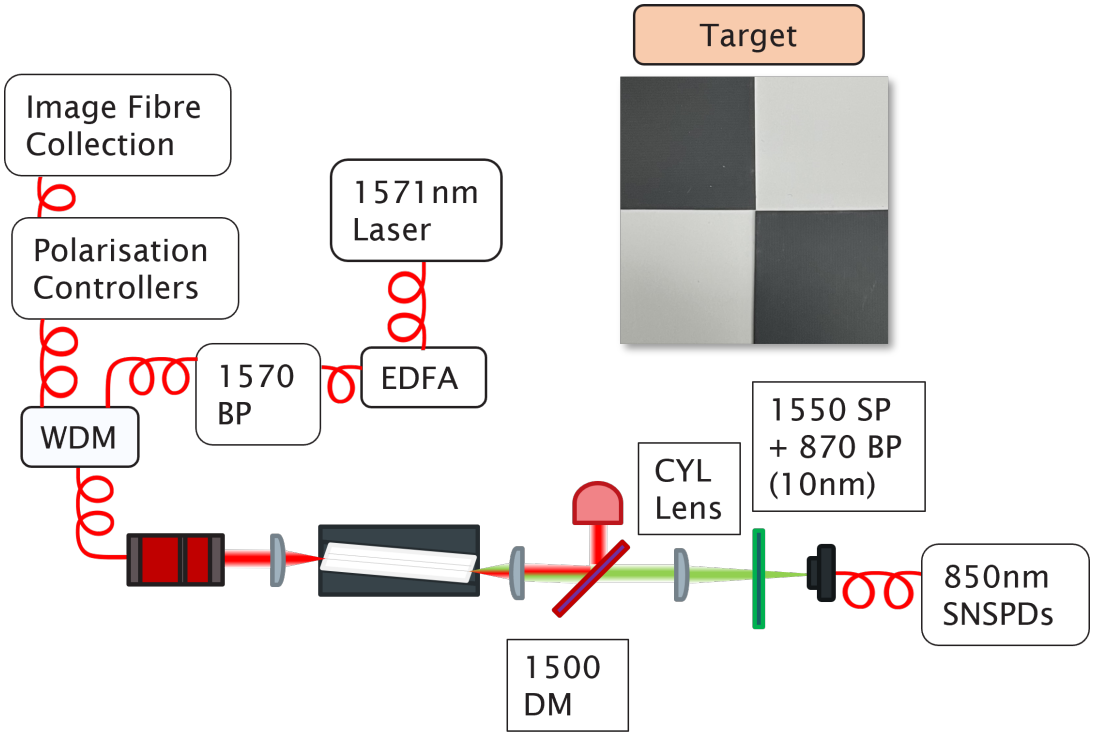

FIGURE 7.12: Upconversion setup connected to the imaging system.

The target is illuminated, and the galvo mirrors scanned over a 6x6mm area, the upconverted photons are collected for 1s each pixel, giving a total collection time of ~5 minutes. The image is displayed in Figure 7.13. The calculated CTN ratio for this image is 2.0, it is immediately apparent that the contrast is not as good as it was for 1570nm direct detection. As we are illuminating with longer wavelengths, the properties of the target are different.

The spatial resolution of the system was calculated from the full-width at half-maximum (FWHM) of the 2D cross-correlation between the upconverted image and the target, giving a value of 1.4mm, Figure 7.14. In upconversion imaging systems with bulk

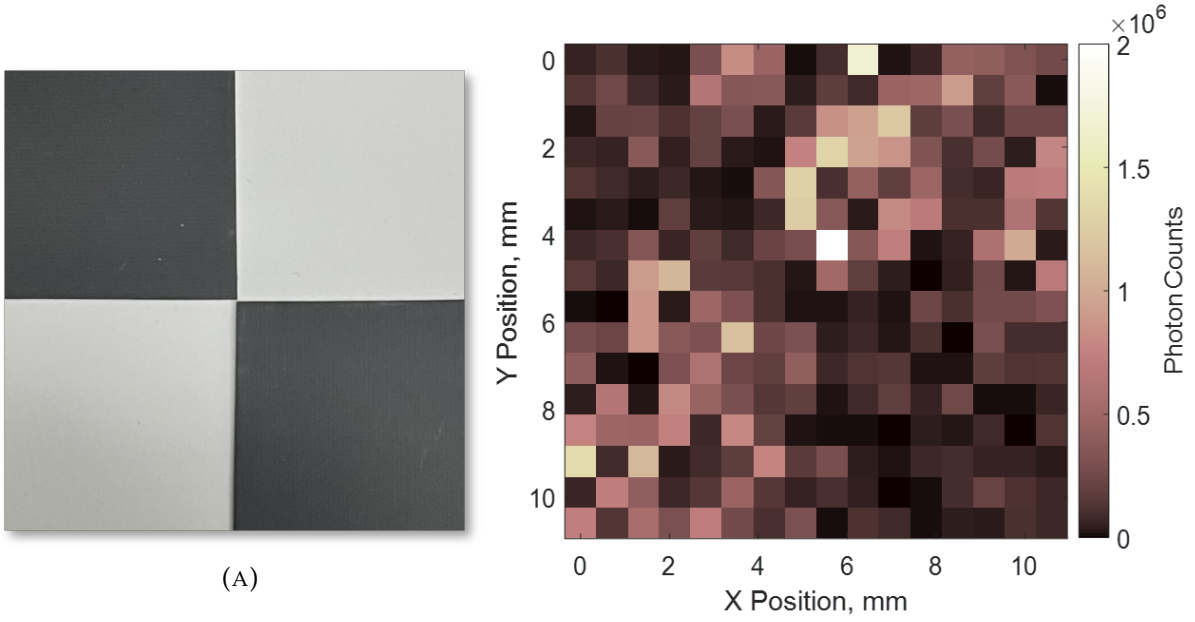

(A) (B)

FIGURE 7.13: Upconverted raster-scan image of a checkerboard pattern, illuminated with ∼100mW of 1950nm CW light, collected back-scatter coupled into a waveguide pumped with 1571.6nm, upconverted mode detected with SNPDs.

nonlinear crystals, the spatial resolution is determined by the aperture size of the crystal or the beam size of the pump, whichever is smallest. A balance is needed between larger pump size for large FOV with smaller pump size for better spatial resolution and conversion efficiency. Since this system uses waveguides instead of bulk crystals, the spatial resolution is limited by the spot size at the target, while our resolution is low compared to other upconversion imaging systems (typically <100µm), it does not have the same limitations.

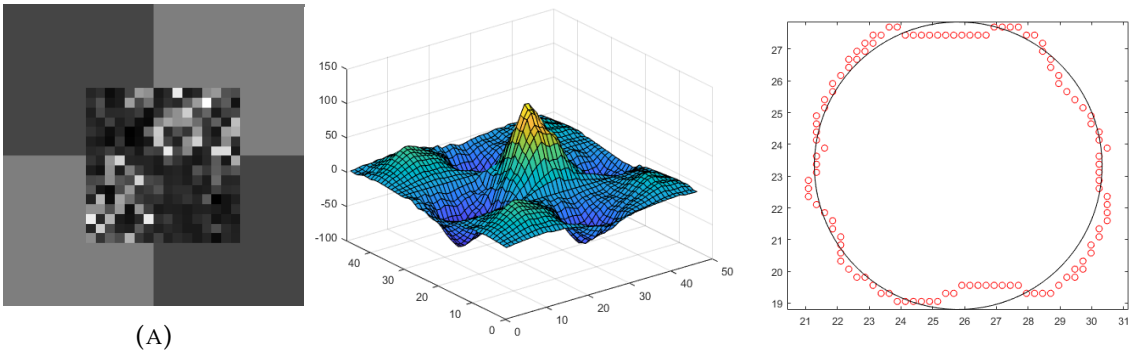

(A)

FIGURE 7.14: (a) Location of image relative to the target, recovered from (b) the cross-correlation of the 2µm upconverted image with the checkerboard pattern, (c) fitting the FWHM of the cross-correlation peak, spatial resolution calculated to be 1.4mm.

To improve the contrast, a stencil is used in place of the previous target, as seen in Figure 7.15. The CTN ratio is now 21.1.

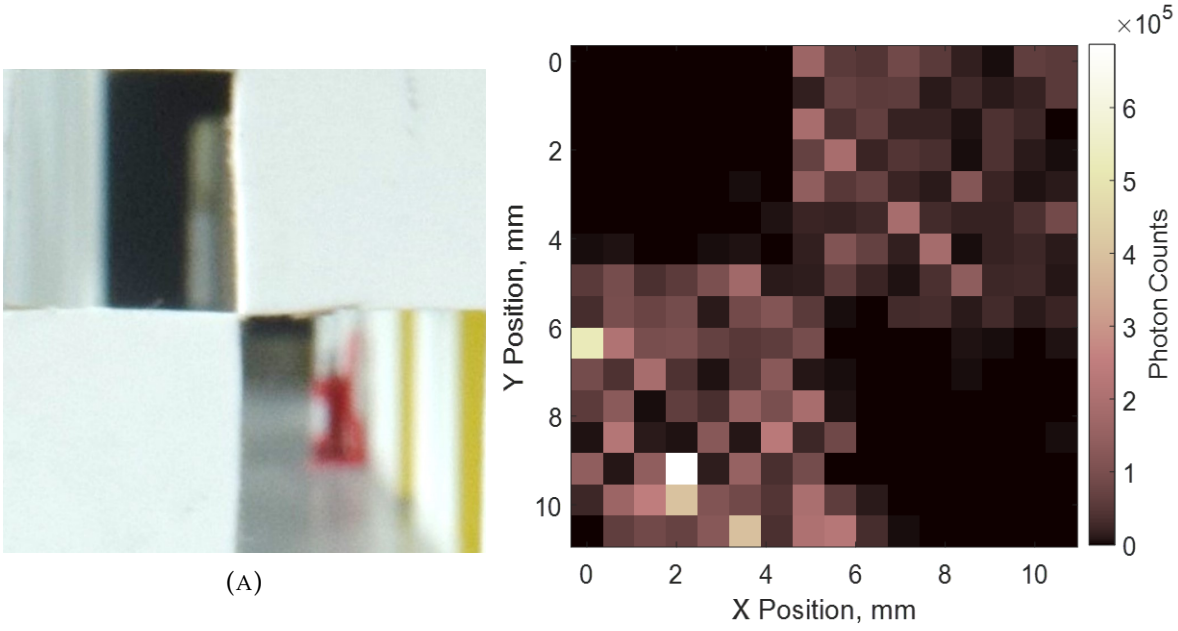

(A) (B)

FIGURE 7.15: Upconverted raster-scan image of a checkerboard stencil, illuminated with ∼100mW of 1950nm CW light, collected back-scatter coupled into a waveguide pumped with 1571.6nm, upconverted mode detected with SNPDs.

The image is scanned over a 10x10mm area, to match the step size of the beam to its spot size. The cross-correlation is once again calculated, Figure 7.16, this time it is 2.6mm. To note that this is due to the larger step size, the angular resolution for both images remains the same.

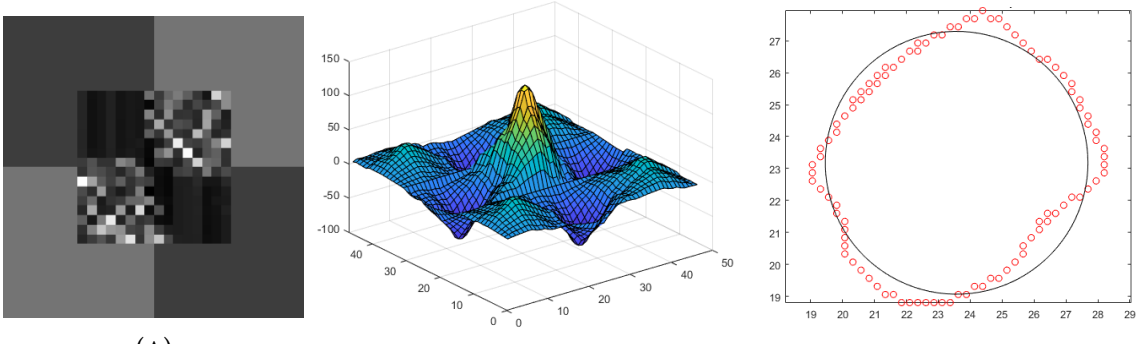

(A) (B) (C)

FIGURE 7.16: (a) Location of image relative to the target, recovered from (b) the cross-correlation of the 2µm upconverted image with the checkerboard pattern, (c) fitting the FWHM of the cross-correlation peak, spatial resolution calculated to be 2.6mm.

An image of the target was taken with the illumination laser off, shown in Figure 7.17, and the correlation coefficient of the image with the target was calculated. The correlation coefficient requires the data to be centered and normalised, and the strength of the correlation is given by the numeric value of the coefficient. A correlation coefficient of 0.33 was calculated, which indicates low correlation between the two, so there is target information in the image.

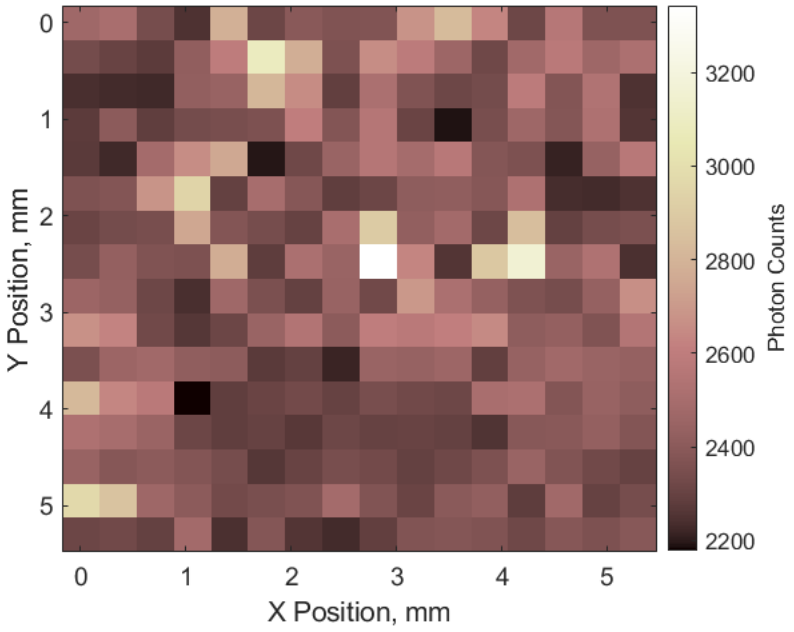

FIGURE 7.17: Upconverted raster-scan image of a checkerboard pattern, illuminated with scene light. Correlation value of 0.33 with the checkerboard pattern target.

To analyse the noise behaviour, the 1950nm laser was turned off and the upconverted counts measured as a function of pump power, shown in Figure 7.18. The data is well fit by a linear dependence on pump power as expected for a spontaneous scattering process. Since the upconversion system was pumped with a wavelength shorter than the illumination wavelength it will be subject to a spontaneous parametric down-conversion (SPDC) noise floor, arising from random duty-cycle errors in the QPM poling enhancing parasitic mixing processes, this is the dominant noise source in frequency conversion systems with short wavelength pumps far away from the signal [139].

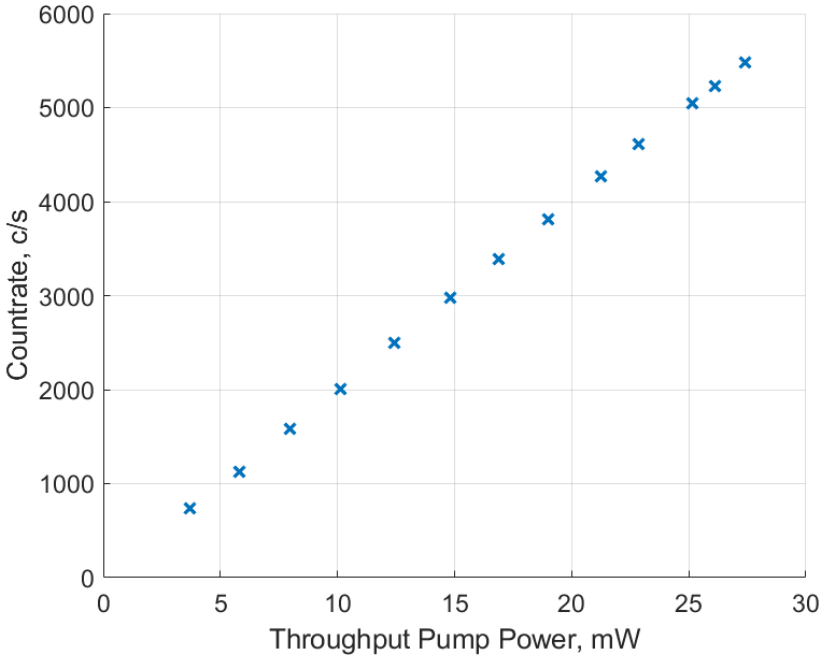

FIGURE 7.18: SNSPD upconverted photon counts at 870nm as a function of increasing 1571.6nm pump power in the SFG PPLN waveguide, with no 1950nm signal.

7.2 Summary

Chapter 7 integrates the developed PPLN waveguides into an upconversion imaging system to demonstrate their practical applications. Operating telecom (1550nm) and NIR (1950nm) wavelengths, the system uses commerically available 1560nm SHG PPLN waveguides, and a developed 1950nm SFG PPLN waveguide to generate visible light for detection with either standard silicon sensors (SPADs) or high-efficiency SNSPDs. The imaging setup includes a Galvo mirror scanning system, enabling raster-scanned images of illuminated objects. Upconverted images with good contrast-to-noise are achieved, with a spatial resolution of 2.6mm. It was also shown that image information was still present when not actively illuminating the target. The results show proof of concept for upconversion imaging at wavelengths longer than telecoms, and highlight the waveguides' potential for compact and cost-effective imaging systems in fields like environmental monitoring, quantum communications and defense applications. Future improvements, such as enhancing resolution and expanding wavelength range, are also discussed.

Chapter 8

Future Work

The goal of my PhD project was to create an IR upconversion system using PPLN waveguides for local and remote detection, and upconversion imaging. The key towards achieving efficient MIR to visible upconversion in PPLN waveguides is developing an in-depth understanding of how the refractive index profile and fabrication parameters must be changed to successfully support MIR modes. In order to generate a theoretical model for the refractive index profile of our PPLN waveguides, several simulations were run across a range of wavelengths, refractive index changes, diffusion depths and ridge widths, and have been presented. The conclusions drawn from the models have set the fabrication parameters for the next generation of MIR waveguides. Part of the work in my PhD was to support optical characterisation of these PPLN waveguides as they are developed. Several additions have been made to the characterisation process of the waveguides, such as Metricon measurements and beam profiling, which in conjunction with modelled phasematching curves, are supplementing our understanding of the effect of the fabrication process on the effective values in the waveguides. This work is a large part of being able to tailor waveguide periods for other projects of interest. While the temperature and wavelength dependence of LN doped with magnesium or zinc is known, expanding the understanding of this relationship in Zn-indiffused MgO:LN will be greatly beneficial to further refine the model

and streamline troubleshooting limitations in the waveguide fabrication process.

As a result of this work, the wavelength range of Zn-indiffused PPLN ridge waveguides being developed here at the University of Southampton has broadened. New waveguides have been created in the visible regime for third-order 780nm SHG and first-order 1064nm SHG, with conversion efficiencies of 3.65%W^{-1} and 100.7%W^{-1}, and generating optical powers of 1.8mW and 175mW respectively. Analysis of the model showed further improvements could be made to increase the efficiencies, which given the high-damage threshold these waveguides have, shows their potential as alternative laser sources, although both green-induced infrared absorption and blue light-induced infrared absorption will need to be taken into consideration. Wavelengths as low as 375nm were generated, the next step would be fabrication of devices for the 739 nm to 369.5 nm process required for application in Yb+ ion trapping technologies. Waveguide width variation was found to be limiting the efficiency when dicing 40mm long waveguides with small ridge widths, which was addressed by using thicker, more rigid blades when dicing. New waveguides in the IR regime included 1950nm SFG and 3.3µm SFG waveguides for conversion to visible wavelengths. For MIR support, high refractive index change and indiffusion depth is needed. Fabrication tests were carried out to further increase these parameters, however there was a saturation point for the refractive index change. Alternative routes to increasing this parameter should be investigated next, such as adding co-dopants.

A raster-scanning imaging system was built and characterised to demonstrate the viability of PPLN waveguides as a mechanism for MIR upconversion imaging. PPLN waveguides were successfully incorporated into the system and upconverted 1950nm backscattered photons from a targert $\sim$1m away, detected by SNSPD detectors at 870nm. This showed proof of concept, where suggested improvements for the current system include improve the image resoultion testing collinear methods of illumination to compare signal-to-noise values, as well as identifying other noise processes in the system.

Appendix A

Conference and journal publications

Publications

1. G. Tawy, **N. Palomar Davidson**, G. Churchill, M. J. Damzen, P. G. Smith, J. C. Gates, and C. B. E. Gawith, "Temperature-tunable UV generation using an alexandrite laser and PPLN waveguides", *Optics Express*, vol. 31 no.14, p. 22757-22765, 2023.

Conferences

1. G. Tawy, **N. Palomar Davidson**, P. L. Mennea, G.M. Topley, P.G. Smith, J.C. Gates, C.B. Gawith, A. Minassian, and M.J. Damzen, "High power alexandrite laser for tunable UV-blue generation", in *EPJ Web of Conferences*, vol. 267, p. 01020, EDP Sciences, 2022.

2. **N. Palomar Davidson**, G. Tawy, G. M. Churchill, P. L. Mennea, R. H. S. Bannerman, P. G. R. Smith, L. D. Wright, G. Blanchard-Emmerson, J. C. Gates, and C. B. E. Gawith, "Developing zinc-indiffused periodically poled lithium niobate ridge waveguides for quantum applications at visible wavelengths", in *Conference on*

Lasers and Electro-Optics Europe & European Quantum Electronics Conference, IEEE, 2023.

3. G. Tawy, **Palomar Davidson, N.**, P.L. Mennea, G. Churchill, L.D. Wright, R.H. Bannerman, P.G. Smith, J.C. Gates, M.J. Damzen, and C.B. Gawith, "375-400nm UV Generation via an Alexandrite laser and Zn-indiffused MgO-doped PPLN Waveguides", In *The European Conference on Lasers and Electro-Optics* p. ca_6_3, Optica Publishing Group, 2023.

4. **N. Palomar Davidson**, G. Tawy, G. M. Churchill, P. L. Mennea, L. D. Wright, G. Blanchard-Emmerson, J. C. Gates, and C. B. E. Gawith, "Developing zinc-indiffused PPLN ridge waveguides for UV, visible and MIR quantum applications", *Nonlinear Frequency Generation and Conversion: Materials and Devices XXIII*, p. PC128690A, SPIE, 2024. **Invited Talk**

5. G. Tawy, **N. Palomar Davidson**, L. D. Wright, P. L. Mennea, G. Churchill, P. G. R. Smith, J. C. Gates, and C. B. E. Gawith, "375-400nm SHG Alexandrite laser using Zn-indiffused MgO: PPLN ridge waveguides", *Solid State Lasers XXXIII: Technology and Devices*, vol. 12864, pp. 140-141. SPIE, 2024.

6. R. Smith, L. Wright, K. Pandiyan, I. Morland, S. McCarthy, A. Anwar, **N. Palomar Davidson**, C. Gawith, and L.J. McKnight, "Efficient Single-Photon Upconversion Detection from SWIR to SPAD using PPLN Waveguides", In *CLEO: Science and Innovations* pp. SF3J-6, Optica Publishing Group, 2024.

Appendix B

Multi-Variable Parameter Sweep

```
import time
import numpy as np
import fimmwavelib as fimm

app = fimm.connect_to_fimmwave('localhost',5101)

# Parameters to be set
N_modes = 12
dn = 0.004
sig = 4.6

param1name = "temp"
param2name = "lamb"
param3name = "width"

param1min = 20 # should be float
param1max = 200 # should be float
param1_steps = 181 # should be integer

param2min = 0.532 # should be float
param2max = 1.064 # should be float
param2_steps = 2 # should be integer

param3min = 5 # should be float
param3max = 8 # should be float
param3_steps = 7 # should be integer

var = app.subnodes[1].subnodes[1]
```

```
wg = app.subnodes[1].subnodes[4].subnodes[9]

param1values = np.linspace(param1min,param1max,param1_steps)
param2values = np.linspace(param2min,param2max,param2_steps)
param3values = np.linspace(param3min,param3max,param3_steps)

#set variables
var.setvariable("modes",str(N_modes))
var.setvariable("delta_n",str(dn))
var.setvariable("sigma",str(sig))
wg.evlist.mlp.maxtefrac=0 #only displays TM modes
wg.evlist.svp.solvid=79 #solver paramters, complex vectorial
# Quasi 2D (YZ) Solver
#wg.evlist.svp.buff="V1 1 250 2 2 0.0001 16 MeshPol 0 0 0.0001 0.0001 50 50 5.00 5.00"
# 3D Solver
wg.evlist.svp.buff="V1 500 250 0 2 0.0001 16 MeshPol 0 0 0.0001 0.0001 50 50 5.00 5.00"
wg.evlist.mlp.nx="ny*(xsize/50)" #sets nx resolution, needed when changing from 2D to 3D

# run scan
for param3 in param3values:

    var.setvariable("lW",-(param3/2))
    var.setvariable("rW",param3/2)
    print(str(param3name)+" = "+str(param3))

    results = []
    modeprf = []
    i = 0

    for param1 in param1values:
        var.setvariable(param1name,param1)
        results.append([])
        print(str(param1name)+" = "+str(param1))
        for param2 in param2values:
            var.setvariable(param2name,param2)
            wg.evlist.unalloc() #deletes old modes
            wg.evlist.update()
            values = ""
            j=1
            print(str(param2name)+" = "+str(param2))
            N_eval = wg.evlist.nevals()
            #print(N_eval)
            for mode_num in range(1,int(N_eval)+1):
                te_frac = wg.evlist.list[mode_num].modedata.tefrac
```

```
            #print(mode_num, te_frac)
            if te_frac == 0 : #only records TM modes
                params = "wav"+str(int(param2*1000))+"nm_temp"+str(int(param1))+
                    "C_width"+str(int(param3*10))+"e-1um_mode"+str(int(j))
                neff = wg.evlist.list[mode_num].neff()
                neff_img = neff.imag
                neff = neff.real
                wg.evlist.list[mode_num].profile.update() # updates MFD calc
                wg.evlist.list[mode_num].profile.calcmodewidth(0,2)
                # runs MFD calculation 0 = intensity, 2 = 1/e^2
                X_MFD_one_e2=wg.evlist.list[mode_num].profile.modewidthx
                Y_MFD_one_e2=wg.evlist.list[mode_num].profile.modewidthy
                values =  values+str(j)+" "+str(neff)+" "+str(neff_img)+" "+
                    str(X_MFD_one_e2)+" "+str(Y_MFD_one_e2)+"    "
                mp=wg.evlist.list[mode_num].profile.data.fielddata("Ey")
                #number corresponds to field component
                #1 for Ex, 2 for Ey, 3 for Ez, 4 for Hx, 5 for Hy, 6 for Hz, 7 for Int
                prf=mp.export("mp_Ey_wg9_"+params)
                #e = open("mp_Ey_wg9_"+params+".txt","w")
                #e.write(str(mp))
                #e.close()
                j=j+1
            else:
                pass
        results[i].append(values)
        #print(results)

    i = i+1

#display results

#change filename to match scan being run
f = open("ParamScan_temp_Gayer_MM_1064SHG_width"+str(int(param3*10))+
          "e-1um_dn40e-4_sigma46e-1um_wg9_indiff35nm_PLM1.txt","w")

strtemp = param2name
strtemp2 = param2name
for z in param1values:
    strtemp = strtemp + ", [" + param1name + "=" + str(z) + "] "
    strtemp2 = strtemp2 + ", mode neff neff(Img) XMFD YMFD"

f.write(strtemp + "\n")
f.write(strtemp2 + "\n")
```

```
    for x in range(0,param2_steps,1):
        strtemp = str(param2values[x])
        for y in range(0,param1_steps,1):
            strtemp = strtemp + "," + str(results[y][x])
        f.write(strtemp+ "\n")
    print("ParamScan_temp_Gayer_MM_1064SHG_width"+str(int(param3*10))+
          "e-1um_dn40e-4_sigma46e-1um_wg9_indiff35nm_PLM1.txt")

    f.close()

fimm.disconnect_fimmwave()
```

Bibliography

[1] J. M. Chalmers and P. R. Griffiths, "Handbook of Vibrational Spectroscopy: Theory and Instrumentation," *Journal of the American Chemical Society*, vol. 1, no. 33, 2002.

[2] D. Xu, S. Liang, L. Xu, K. N. Bourdakos, P. Johnson, J. Read, J. H. Price, S. Mahajan, and D. J. Richardson, "Widely-tunable synchronisation-free picosecond laser source for multimodal CARS, SHG, and two-photon microscopy," *Biomedical Optics Express*, vol. 12, no. 2, pp. 1010–1019, 2021.

[3] T. Encrenaz, "Infrared spectroscopy of exoplanets: observational constraints," *Philosophical Transactions of the Royal Society A: Mathematical, Physical and Engineering Sciences*, vol. 372, no. 2014, p. 20130083, 2014.

[4] A. Barh, P. J. Rodrigo, L. Meng, C. Pedersen, and P. Tidemand-Lichtenberg, "Parametric upconversion imaging and its applications," *Advances in Optics and Photonics*, vol. 11, no. 4, p. 952, 2019.

[5] U. Sharma, "Infrared detectors," in *Tech Credit Seminar Report, Electronic Systems Group, IIT Bombay*, 2004.

[6] R. W. Boyd, *Nonlinear Optics*. Springer, 2008.

[7] T. H. Maiman, "Stimulated optical radiation in ruby," *Nature*, vol. 187, no. 4736, pp. 493–494, 1960.

[8] P. A. Franken, A. E. Hill, C. W. Peters, and G. Weinreich, "Generation of optical harmonics," *Physical Review Letters*, vol. 7, no. 4, p. 118, 1961.

[9] J. A. Armstrong, N. Bloembergen, J. Ducuing, and P. S. Pershan, "Interactions between light waves in a nonlinear dielectric," *Physical Review*, vol. 127, no. 6, p. 1918, 1962.

[10] J. E. Midwinter, "Image conversion from 1.6μm to the visible in lithium niobate," *Applied Physics Letters*, vol. 12, no. 3, pp. 68–70, 1968.

[11] J. Falk and W. Tiffany, "Theory of parametric upconversion of thermal images," *Journal of Applied Physics*, vol. 43, no. 9, pp. 3762–3769, 1972.

[12] R. A. Andrews, "IR Image Parametric Up-Conversion," *IEEE Journal of Quantum Electronics*, vol. 6, no. 1, pp. 68–80, 1970.

[13] M. Yamada, N. Nada, M. Saitoh, and K. Watanabe, "First-order quasi-phase matched $LiNbO_3$ waveguide periodically poled by applying an external field for efficient blue second-harmonic generation," *Applied Physics Letters*, vol. 62, no. 5, pp. 435–436, 1993.

[14] G.-L. Shentu, J. S. Pelc, X.-D. Wang, Q.-C. Sun, M.-Y. Zheng, M. M. Fejer, Q. Zhang, and J.-W. Pan, "Ultralow noise up-conversion detector and spectrometer for the telecom band," *Optics Express*, vol. 21, no. 12, p. 13986, 2013.

[15] J. S. Dam, C. Pedersen, and P. Tidemand-Lichtenberg, "High-resolution two-dimensional image upconversion of incoherent light," *Optics Letters*, vol. 35, no. 22, p. 3796, 2010.

[16] G. B. Lemos, V. Borish, G. D. Cole, S. Ramelow, R. Lapkiewicz, and A. Zeilinger, "Quantum imaging with undetected photons," *Nature*, vol. 512, no. 7515, pp. 409–412, 2014.

[17] R. L. Pedersen, D. Hot, and Z. Li, "Comparison of an InSb Detector and Upconversion Detector for Infrared Polarization Spectroscopy," *Applied Spectroscopy*, vol. 72, no. 5, pp. 793–797, 2018.

[18] J. Warner, "Parametric up-conversion from the infra-red," *Opto-electronics*, vol. 3, pp. 37–48, 1971.

[19] J. S. Dam, C. Pedersen, and P. Tidemand-Lichtenberg, "Theory for upconversion of incoherent images," *Optics Express*, vol. 20, no. 2, 2012.

[20] J. S. Dam, P. Tidemand-Lichtenberg, and C. Pedersen, "Room-temperature mid-infrared single-photon spectral imaging," *Nature Photonics*, vol. 6, no. 11, pp. 788–793, 2012.

[21] B. E. A. Saleh and M. C. Teich, "Fundamentals of Photonics , 2nd Edition," 2007.

[22] K. Huang, J. Fang, M. Yan, E. Wu, and H. Zeng, "Wide-field mid-infrared single-photon upconversion imaging," *Nature Communications*, vol. 13, no. 1, p. 1077, 2022.

[23] S. Junaid, S. Chaitanya Kumar, M. Mathez, M. Hermes, N. Stone, N. Shepherd, M. Ebrahim-Zadeh, P. Tidemand-Lichtenberg, and C. Pedersen, "Video-rate, mid-infrared hyperspectral upconversion imaging," *Optica*, vol. 6, no. 6, p. 702, 2019.

[24] R. Demur, R. Garioud, A. Grisard, E. Lallier, L. Leviandier, L. Morvan, N. Treps, and C. Fabre, "Near-infrared to visible upconversion imaging using a broadband pump laser," *Optics Express*, vol. 26, no. 10, pp. 13252–13263, 2018.

[25] J. Fang, K. Huang, E. Wu, M. Yan, and H. Zeng, "Mid-infrared single-photon 3D imaging," *Light: Science & Applications*, vol. 12, no. 1, p. 144, 2023.

[26] J. Fang, K. Huang, R. Qin, Y. Liang, E. Wu, M. Yan, and H. Zeng, "Wide-field mid-infrared hyperspectral imaging beyond video rate," *Nature Communications*, vol. 15, no. 1, p. 1811, 2024.

[27] A. J. Torregrosa, E. Karamehmedović, H. Maestre, M. L. Rico, and J. Capmany, "Up-conversion sensing of 2D spatially-modulated infrared information-carrying beams with Si-based cameras," *Sensors*, vol. 20, no. 12, p. 3610, 2020.

[28] L. M. Kehlet, P. Tidemand-Lichtenberg, J. S. Dam, and C. Pedersen, "Infrared upconversion hyperspectral imaging," *Optics Letters*, vol. 40, no. 6, pp. 938–941, 2015.

[29] N. Sanders, J. S. Dam, O. B. Jensen, P. Tidemand-Lichtenberg, and C. Pedersen, "Multispectral mid-infrared imaging using frequency upconversion," in *Nonlinear Frequency Generation and Conversion: Materials, Devices, and Applications XII*, vol. 8604, pp. 111–116, SPIE, 2013.

[30] S. Tanzilli, W. Tittel, M. Halder, O. Alibart, P. Baldi, N. Gisin, and H. Zbinden, "A photonic quantum information interface," *Nature*, vol. 437, no. 7055, pp. 116–120, 2005.

[31] J. Zhang, M. A. Itzler, H. Zbinden, and J. W. Pan, "Advances in InGaAs/InP single-photon detector systems for quantum communication," *Light: Science and Applications*, vol. 4, no. 5, pp. e286–e286, 2015.

[32] O. Alibart, V. D'Auria, M. De Micheli, F. Doutre, F. Kaiser, L. Labonté, T. Lunghi, É. Picholle, and S. Tanzilli, "Quantum photonics at telecom wavelengths based on lithium niobate waveguides," *Journal of Optics*, vol. 18, no. 10, p. 104001, 2016.

[33] R. V. Roussev, C. Langrock, J. R. Kurz, and M. M. Fejer, "Periodically poled lithium niobate waveguide sum-frequency generator for efficient single-photon detection at communication wavelengths," *Optics Letters*, vol. 29, no. 13, pp. 1518–1520, 2004.

[34] C. Langrock, E. Diamanti, R. V. Roussev, Y. Yamamoto, M. M. Fejer, and H. Takesue, "Highly efficient single-photon detection at communication wavelengths by use of upconversion in reverse-proton-exchanged periodically poled $LiNbO_3$ waveguides," *Optics Letters*, vol. 30, no. 13, pp. 1725–1727, 2005.

[35] H. Xu, L. Ma, O. Slattery, and X. Tang, "Low-noise PPLN-based single-photon detector," in *Quantum Communications Realized*, vol. 6780, p. 67800U, International Society for Optics and Photonics, SPIE, 2007.

[36] N. Yao, Q. Yao, X.-P. Xie, Y. Liu, P. Xu, W. Fang, M.-Y. Zheng, J. Fan, Q. Zhang, L. Tong, and J.-W. Pan, "Optimizing up-conversion single-photon detectors for quantum key distribution," *Optics Express*, vol. 28, no. 17, pp. 25123–25133, 2020.

[37] K. Huang, Y. Wang, J. Fang, W. Kang, Y. Sun, Y. Liang, Q. Hao, M. Yan, and H. Zeng, "Mid-infrared photon counting and resolving via efficient frequency upconversion," *Photonics Research*, vol. 9, no. 2, pp. 259–265, 2021.

[38] L. Lehmann, L. Grossard, L. Delage, F. Reynaud, M. Chauvet, and F. Bassignot, "Single photon MIR upconversion detector at room temperature with a PPLN ridge waveguide," *Optics Express*, vol. 27, no. 14, p. 19233, 2019.

[39] W. P. Risk, T. R. Gosnell, and A. V. Nurmikko, *Compact blue-green lasers*. Cambridge University Press, 2003.

[40] P. S. Kuo, O. Slattery, Y.-S. Kim, J. S. Pelc, M. Fejer, and X. Tang, "Spectral response of an upconversion detector and spectrometer," *Optics Express*, vol. 21, no. 19, pp. 22523–22531, 2013.

[41] L. G. Carpenter, S. A. Berry, A. C. Gray, J. C. Gates, P. G. R. Smith, and C. B. E. Gawith, "CW demonstration of SHG spectral narrowing in a PPLN waveguide generating 25 W at 780 nm," *Optics Express*, vol. 28, no. 15, pp. 21382–21390, 2020.

[42] S. A. Berry, L. G. Carpenter, A. C. Gray, P. G. R. Smith, and C. B. E. Gawith, "Zn-indiffused diced ridge waveguides in MgO:PPLN generating 1 watt 780 nm SHG at 70% efficiency," *OSA Continuum*, vol. 2, no. 12, pp. 3456–3464, 2019.

[43] L. G. Carpenter, S. A. Berry, R. H. S. Bannerman, A. C. Gray, and C. B. E. Gawith, "ZnO indiffused MgO:PPLN ridge waveguides," *Optics Express*, vol. 27, no. 17, pp. 24538–24544, 2019.

[44] A. C. Gray, S. A. Berry, L. G. Carpenter, J. C. Gates, C. B. Gawith, and P. G. Smith, "Upconversion detection of 1.25 Gb/s mid-infrared telecommunications using a silicon avalanche photodiode," *Optics Express*, vol. 28, no. 23, pp. 34279–34289, 2020.

[45] J. Villarroel, J. Carnicero, F. Luedtke, M. Carrascosa, A. García-Cabañes, J. Cabrera, A. Alcazar, and B. Ramiro, "Analysis of photorefractive optical damage in lithium niobate: application to planar waveguides," *Optics express*, vol. 18, no. 20, pp. 20852–20861, 2010.

[46] W. Young, R. Feigelson, M. M. Fejer, M. J. Digonnet, and H. J. Shaw, "Photorefractive-damage-resistant Zn-diffused waveguides in MgO:$LiNbO_3$," *Optics letters*, vol. 16, no. 13, pp. 995–997, 1991.

[47] F. Schiller, B. Herreros, and G. Lifante, "Optical characterization of vapor zn-diffused waveguides in lithium niobate," *JOSA A*, vol. 14, no. 2, pp. 425–429, 1997.

[48] A. C. Gray, J. R. C. Woods, L. G. Carpenter, H. Kahle, S. A. Berry, A. C. Tropper, M. Guina, V. Apostolopoulos, P. G. R. Smith, and C. B. E. Gawith, "Zinc-indiffused MgO:PPLN waveguides for blue/UV generation via VECSEL pumping," *Applied Optics*, vol. 59, no. 16, p. 4921, 2020.

[49] G. Grinblat, H. Zhang, M. P. Nielsen, L. Krivitsky, R. Berté, Y. Li, B. Tilmann, E. Cortés, R. F. Oulton, A. I. Kuznetsov, *et al.*, "Efficient ultrafast all-optical modulation in a nonlinear crystalline gallium phosphide nanodisk at the anapole excitation," *Science Advances*, vol. 6, no. 34, p. eabb3123, 2020.

[50] L. Maidment, P. G. Schunemann, and D. T. Reid, "Molecular fingerprint-region spectroscopy from 5 to 12 µm using an orientation-patterned gallium phosphide optical parametric oscillator," *Optics Letters*, vol. 41, no. 18, pp. 4261–4264, 2016.

[51] D. A. Kleinman, "Nonlinear dielectric polarization in optical media," *Physical Review*, vol. 126, no. 6, pp. 1977–1978, 1962.

[52] J. Sherman, "Blue to UV laser stage, closeup," 2005. https://www.flickr.com/photos/fatllama/44883250 [Date Last Accessed 02/04/2022].

[53] T. Skauli, K. L. Vodopyanov, T. J. Pinguet, A. Schober, O. Levi, L. A. Eyres, M. M. Fejer, J. S. Harris, B. Gerard, L. Becouarn, E. Lallier, and G. Arisholm, "Measurement of the nonlinear coefficient of orientation-patterned GaAs and demonstration of highly efficient second-harmonic generation," *Optics Letters*, vol. 27, no. 8, pp. 628–630, 2002.

[54] I. Shoji, T. Kondo, A. Kitamoto, M. Shirane, and R. Ito, "Absolute scale of second-order nonlinear-optical coefficients," *Journal of the Optical Society of America B*, vol. 14, no. 9, pp. 2268–2294, 1997.

[55] D. S. Hum and M. M. Fejer, "Quasi-phasematching," *Comptes Rendus Physique*, vol. 8, no. 2, pp. 180–198, 2007. Recent advances in crystal optics.

[56] C. Pedersen, A. Ashik, and P. Tidemand-Lichtenberg, "Nonlinear crystals for imaging and detection of mid-IR radiation," in *Smart Photonic and Optoelectronic Integrated Circuits XXII*, vol. 11284, pp. 74–79, SPIE, 2020.

[57] T. Volk and M. Wöhlecke, *Lithium niobate: defects, photorefraction and ferroelectric switching*, vol. 115. Springer Science & Business Media, 2008.

[58] T. Volk, N. Rubinina, and M. Wöhlecke, "Optical-damage-resistant impurities in lithium niobate," *Journal of the Optical Society of America B*, vol. 11, no. 9, pp. 1681–1687, 1994.

[59] O. Gayer, Z. Sacks, E. Galun, and A. Arie, "Temperature and wavelength dependent refractive index equations for MgO-doped congruent and stoichiometric $LiNbO_3$," *Applied Physics B: Lasers and Optics*, vol. 91, no. 2, pp. 343–348, 2008.

[60] D. Xue, K. Betzler, and H. Hesse, "Second order nonlinear optical properties of in-doped lithium niobate," *Journal of Applied Physics*, vol. 89, no. 2, pp. 849–854, 2001.

[61] "Material properties of lithium niobate." https://covesion.com/en/resource/material-properties-of-lithium-niobate/ [Date Last Accessed 14/08/2024].

[62] C. R. Pollock and M. Lipson, *Integrated photonics*, vol. 20. Springer, 2003.

[63] A. Ghatak and K. Thyagarajan, *An Introduction to Fibre Optics*. Cambridge University Press, 1998.

[64] N. Uesugi and T. Kimura, "Efficient second-harmonic generation in three-dimensional $LiNbO_3$ optical waveguide," *Applied Physics Letters*, vol. 29, no. 9, pp. 572–574, 1976.

[65] M. Fukuma, J. Noda, and H. Iwasaki, "Optical properties in titanium-diffused $LiNbO_3$ strip waveguides," *Journal of Applied Physics*, vol. 49, no. 7, pp. 3693–3698, 1978.

[66] S. Fouchet, A. Carenco, C. Daguet, R. Guglielmi, and L. Riviere, "Wavelength dispersion of Ti induced refractive index change in $LiNbO_3$ as a function of diffusion parameters," *Journal of lightwave technology*, vol. 5, no. 5, pp. 700–708, 1987.

[67] W. Burns, P. Klein, E. West, and L. Plew, "Ti diffusion in Ti:$LiNbO_3$ planar and channel optical waveguides," *Journal of Applied Physics*, vol. 50, no. 10, pp. 6175–6182, 1979.

[68] R. Becker, ""thermal fixing"of ti-indiffused linbo3 channel waveguides for reduced photorefractive susceptibility," *Applied physics letters*, vol. 45, no. 2, pp. 121–123, 1984.

[69] M. Fejer, M. Digonnet, and R. Byer, "Generation of 22 mw of 532-nm radiation by frequency doubling in ti: Mgo: Linbo 3 waveguides," *Optics letters*, vol. 11, no. 4, pp. 230–232, 1986.

[70] J. L. Jackel, C. Rice, and J. Veselka, "Proton exchange for high-index waveguides in $LiNbO_3$," *Applied Physics Letters*, vol. 41, no. 7, pp. 607–608, 1982.

[71] J. Jackel, A. Glass, G. Peterson, C. Rice, D. Olson, and J. Veselka, "Damage-resistant $LiNbO_3$ waveguides," *Journal of applied physics*, vol. 55, no. 1, pp. 269–270, 1984.

[72] K. El Hadi, M. Sundheimer, P. Aschieri, P. Baldi, M. De Micheli, D. Ostrowsky, and F. Laurell, "Quasi-phase-matched parametric interactions in proton-exchanged lithium niobate waveguides," *JOSA B*, vol. 14, no. 11, pp. 3197–3203, 1997.

[73] L. Chanvillard, P. Aschieri, P. Baldi, D. Ostrowsky, M. De Micheli, L. Huang, and D. Bamford, "Soft proton exchange on periodically poled $LiNbO_3$: A simple waveguide fabrication process for highly efficient nonlinear interactions," *Applied Physics Letters*, vol. 76, no. 9, pp. 1089–1091, 2000.

[74] T. Kawaguchi, K. Mizuuchi, T. Yoshino, J. Kondo, A. Kondo, M. Imaeda, and K. Yamamoto, "New ridge-type waveguide QPM-SHG device fabricated by ultraprecision machining," in *International Symposium on Optical Memory. Technical Digest*, p. 66, 2000.

[75] T. Kawaguchi, T. Yoshino, J. Kondo, A. Kondo, S. Yamaguchi, K.-I. Noda, T. Nehagi, M. Imaeda, K. Mizuuchi, and Y. Kitaoka, "High-power blue/violet QPM-SHG laser using a new ridge-type waveguide," in *Technical Digest. Summaries of*

papers presented at the Conference on Lasers and Electro-Optics. Postconference Technical Digest (IEEE Cat. No.01CH37170), pp. 141–142, 2001.

[76] S. Suntsov, K. Hasse, and D. Kip, "Efficient watt-level 0.775 µm SHG and 3.3 µm DFG in annealed and reverse proton exchanged diced PPLN ridge waveguides," in *EPJ Web of Conferences*, vol. 255, p. 06001, EDP Sciences, 2021.

[77] A. Kadetova, O. Tokko, A. Prusskii, O. Spirin, and M. Palatnikov, "Effect of magnesium and zinc doping of lithium niobate crystals on nonlinear optical characteristics," *Optical Materials*, vol. 144, p. 114296, 2023.

[78] W. M. Young, M. M. Fejer, M. J. Digonnet, A. F. Marshall, and R. S. Feigelson, "Fabrication, Characterization and Index Profile Modeling of High-Damage Resistance Zn-Diffused Waveguides in Congruent and MgO: Lithium Niobate," *Journal of Lightwave Technology*, vol. 10, no. 9, pp. 1238–1246, 1992.

[79] R. Nevado and G. Lifante, "Characterization of index profiles of Zn-diffused $LiNbO_3$ waveguides," *Journal of the Optical Society of America*, vol. 16, no. 10, pp. 2574–2580, 1999.

[80] L. Ming, C. B. E. Gawith, K. Gallo, M. V. O'Connor, G. D. Emmerson, and P. G. R. Smith, "High conversion efficiency single-pass second harmonic generation in a zinc-diffused periodically poled lithium niobate waveguide," *Optics Express*, vol. 13, no. 13, pp. 4862–4868, 2005.

[81] C. Wang, C. Langrock, A. Marandi, M. Jankowski, M. Zhang, B. Desiatov, M. M. Fejer, and M. Lončar, "Ultrahigh-efficiency wavelength conversion in nanophotonic periodically poled lithium niobate waveguides," *Optica*, vol. 5, no. 11, pp. 1438–1441, 2018.

[82] A. C. Gray, S. A. Berry, L. G. Carpenter, J. C. Gates, P. G. Smith, and C. B. Gawith, "Investigation of PPLN waveguide uniformity via second harmonic generation spectra," *IEEE Photonics Technology Letters*, vol. 32, no. 1, pp. 63–66, 2019.

[83] L. G. Carpenter, S. A. Berry, T. H. Legg, M. C. Farries, C. J. Watson, R. H. Bannerman, A. C. Gray, C. Holmes, J. C. Gates, P. G. Smith, *et al.*, "Zn: Mgo: Ppln waveguides for rb cold atom trap based quantum gravitometry in a cubesat," in *2019 Conference on Lasers and Electro-Optics Europe & European Quantum Electronics Conference (CLEO/Europe-EQEC)*, pp. 1–1, IEEE, 2019.

[84] L. Carpenter, S. Berry, C. Gawith, and P. Smith, "Method for fabrication of ridge waveguides, GB2584877," tech. rep., 2019.

[85] L. G. Carpenter, S. A. Berry, and C. B. Gawith, "Ductile dicing of $LiNbO_3$ ridge waveguide facets to achieve 0.29 nm surface roughness in single process step," *Electronics Letters*, vol. 53, no. 25, 2017.

[86] G. D. Boyd and D. A. Kleinman, "Parametric interaction of focused Gaussian light beams," *Journal of Applied Physics*, vol. 39, no. 8, pp. 3597–3639, 1968.

[87] R. Nevado, C. Sada, F. Segato, F. Caccavale, A. Kling, J. C. Soares, E. Cantelar, F. Cussó, and G. Lifante, "Compositional characterisation of Zn-diffused lithium niobate waveguides," *Applied Physics B: Lasers and Optics*, vol. 73, no. 5, pp. 555–558, 2001.

[88] R. Nevado, G. Lifante, G. Torchia, J. Sanz-García, and F. Jaque, "Concentration dependence of refractive index in Zn-doped $LiNbO_3$ crystals," *Optical Materials*, vol. 11, no. 1, pp. 35–40, 1998.

[89] F. Caccavale, P. Chakraborty, A. Quaranta, I. Mansour, G. Gianello, S. Bosso, R. Corsini, and G. Mussi, "Secondary-ion-mass spectrometry and near-field studies of Ti:$LiNbO_3$ optical waveguides," *Journal of Applied Physics*, vol. 78, no. 9, pp. 5345–5350, 1995.

[90] J. Crank, *The mathematics of diffusion*. Oxford University Press, 1979.

[91] D. E. Zelmon, D. L. Small, and D. Jundt, "Infrared corrected Sellmeier coefficients for congruently grown lithium niobate and 5 mol. % magnesium oxide-doped lithium niobate," *Journal of the Optical Society of America B*, vol. 14, no. 12, pp. 3319–3322, 1997.

[92] K. S. Chiang, C. L. Wong, S. Y. Cheng, and H. P. Chan, "Refractive-index profiling of graded-index planar waveguides from effective indexes measured with different external refractive indexes," *Journal of Lightwave Technology*, vol. 18, no. 10, pp. 1412–1417, 2000.

[93] R. Bannerman, *Microfabrication of waveguide-based devices for quantum optics*. PhD thesis, University of Southampton, 2019.

[94] I. 11146-1:2021, "Lasers and laser-related equipment — Test methods for laser beam widths, divergence angles and beam propagation ratios - Part 1: Stigmatic and simple astigmatic beams," standard, International Organization for Standardization, Geneva, CH, 2021.

[95] S. A. Self, "Focusing of spherical gaussian beams," *Applied optics*, vol. 22, no. 5, pp. 658–661, 1983.

[96] S. Mulholland, H. Klein, G. Barwood, S. Donnellan, P. Nisbet-Jones, G. Huang, G. Walsh, P. Baird, and P. Gill, "Compact laser system for a laser-cooled ytterbium ion microwave frequency standard," *Review of Scientific Instruments*, vol. 90, no. 3, 2019.

[97] A. Anwar, C. Perumangatt, F. Steinlechner, T. Jennewein, and A. Ling, "Entangled photon-pair sources based on three-wave mixing in bulk crystals," *Review of Scientific Instruments*, vol. 92, no. 4, 2021.

[98] R. C. Sterling, H. Rattanasonti, S. Weidt, K. Lake, P. Srinivasan, S. Webster, M. Kraft, and W. K. Hensinger, "Fabrication and operation of a two-dimensional ion-trap lattice on a high-voltage microchip," *Nature communications*, vol. 5, no. 1, p. 3637, 2014.

[99] K. Mizuuchi, T. Sugita, K. Yamamoto, T. Kawaguchi, T. Yoshino, and M. Imaeda, "Efficient 340-nm light generation by a ridge-type waveguide in a first-order periodically poled MgO:$LiNbO_3$," *Optics letters*, vol. 28, no. 15, pp. 1344–1346, 2003.

[100] H. Kiriyama, M. Mori, Y. Nakai, T. Shimomura, M. Tanoue, A. Akutsu, S. Kondo, S. Kanazawa, H. Okada, T. Motomura, *et al.*, "High-contrast, high-intensity laser pulse generation using a nonlinear preamplifier in a ti: sapphire laser system," *Optics letters*, vol. 33, no. 7, pp. 645–647, 2008.

[101] J. Ye, L. S. Ma, and J. L. Hall, "Molecular iodine clock," *Physical review letters*, vol. 87, no. 27, p. 270801, 2001.

[102] M. P. D'Souza, G. Churchill, P. C. Gow, P. G. Smith, C. B. Gawith, and J. C. Gates, "Optimisation of dicing parameters for lithium niobate ridge waveguide fabrication," in *Advanced Fabrication Technologies for Micro/Nano Optics and Photonics XVII*, p. PC128980W, SPIE, 2024.

[103] X. Cheng, X. Feng, L. Ma, J. Chen, H. Chen, and W. Liang, "Fabrication and characterization of high-damage resistance Zn-diffused MgO:PPLN ridge waveguides," *Optoelectronics Letters*, vol. 20, no. 1, pp. 12–17, 2024.

[104] N. Ida and N. Meyendorf, *Handbook of advanced nondestructive evaluation*, vol. 10. Springer International Publishing Cham, Switzerland, 2019.

[105] K. G. Larkin, "Efficient nonlinear algorithm for envelope detection in white light interferometry," *JOSA A*, vol. 13, no. 4, pp. 832–843, 1996.

[106] G. Tawy, N. Palomar Davidson, G. Churchill, M. J. Damzen, P. G. Smith, J. C. Gates, and C. B. Gawith, "Temperature-tunable UV generation using an Alexandrite laser and PPLN waveguides," *Optics Express*, vol. 31, no. 14, pp. 22757–22765, 2023.

[107] M. Ebrahim-Zadeh and I. T. Sorokina, *Mid-infrared coherent sources and applications*. Springer Science & Business Media, 2008.

[108] K. L. Vodopyanov, *Laser-based mid-infrared sources and applications*. John Wiley & Sons, 2020.

[109] S. M. Mintenig, I. Int-Veen, M. G. Löder, S. Primpke, and G. Gerdts, "Identification of microplastic in effluents of waste water treatment plants using focal plane array-based micro-fourier-transform infrared imaging," *Water research*, vol. 108, pp. 365–372, 2017.

[110] Y. Ozaki, "Infrared spectroscopy—mid-infrared, near-infrared, and far-infrared/terahertz spectroscopy," *Analytical Sciences*, vol. 37, no. 9, pp. 1193–1212, 2021.

[111] T. P. Wrobel and R. Bhargava, "Infrared spectroscopic imaging advances as an analytical technology for biomedical sciences," *Analytical chemistry*, vol. 90, no. 3, pp. 1444–1463, 2018.

[112] O. Spitz, P. Didier, L. Durupt, D. A. Díaz-Thomas, A. N. Baranov, L. Cerutti, and F. Grillot, "Free-space communication with directly modulated mid-infrared quantum cascade devices," *IEEE Journal of Selected Topics in Quantum Electronics*, vol. 28, no. 1: Semiconductor Lasers, pp. 1–9, 2021.

[113] A. C. Dada, J. Kaniewski, C. Gawith, M. Lavery, R. H. Hadfield, D. Faccio, and M. Clerici, "Near-maximal two-photon entanglement for optical quantum communication at 2.1 μm," *Physical Review Applied*, vol. 16, no. 5, p. L051005, 2021.

[114] M. Mancinelli, A. Trenti, S. Piccione, G. Fontana, J. S. Dam, P. Tidemand-Lichtenberg, C. Pedersen, and L. Pavesi, "Mid-infrared coincidence measurements on twin photons at room temperature," *Nature Communications*, vol. 8, no. 1, p. 15184, 2017.

[115] M. Bock, A. Lenhard, C. Chunnilall, and C. Becher, "Highly efficient heralded single-photon source for telecom wavelengths based on a PPLN waveguide," *Optics Express*, vol. 24, no. 21, pp. 23992–24001, 2016.

[116] B. Wei, W.-H. Cai, C. Ding, G.-W. Deng, R. Shimizu, Q. Zhou, and R.-B. Jin, "Mid-infrared spectrally-uncorrelated biphotons generation from doped PPLN: a theoretical investigation," *Optics Express*, vol. 29, no. 1, pp. 256–271, 2021.

[117] S.-K. Liao, H.-L. Yong, C. Liu, G.-L. Shentu, D.-D. Li, J. Lin, H. Dai, S.-Q. Zhao, B. Li, J.-Y. Guan, *et al.*, "Long-distance free-space quantum key distribution in daylight towards inter-satellite communication," *Nature Photonics*, vol. 11, no. 8, pp. 509–513, 2017.

[118] R. W. Boyd and C. Townes, "An infrared upconverter for astronomical imaging," *Applied Physics Letters*, vol. 31, no. 7, pp. 440–442, 1977.

[119] D. Kleinman and G. Boyd, "Infrared detection by optical mixing," *Journal of Applied Physics*, vol. 40, no. 2, pp. 546–566, 1969.

[120] K. Karstad, A. Stefanov, M. Wegmuller, H. Zbinden, N. Gisin, T. Aellen, M. Beck, and J. Faist, "Detection of mid-IR radiation by sum frequency generation for free space optical communication," *Optics and Lasers in Engineering*, vol. 43, no. 3-5, pp. 537–544, 2005.

[121] A. Barh, C. Pedersen, and P. Tidemand-Lichtenberg, "Ultra-broadband mid-wave-IR upconversion detection," *Optics Letters*, vol. 42, no. 8, p. 1504, 2017.

[122] S. M. M. Friis and L. Høgstedt, "Upconversion-based mid-infrared spectrometer using intra-cavity $LiNbO_3$ crystals with chirped poling structure," *Optics Letters*, 2019.

[123] "S2050 Mid-Infrared Spectrometer." https://nlir.com/spectrometer-2-0-5-0-%c2%b5m/ [Date Last Accessed 07/12/2024].

[124] G. G. Taylor, D. Morozov, N. R. Gemmell, K. Erotokritou, S. Miki, H. Terai, and R. H. Hadfield, "Photon counting LIDAR at 2.3 µm wavelength with superconducting nanowires," *Optics Express*, vol. 27, no. 26, pp. 38147–38158, 2019.

[125] M. D. Eisaman, J. Fan, A. Migdall, and S. V. Polyakov, "Invited Review Article: Single-photon sources and detectors," 2011.

[126] F. Marsili, V. B. Verma, J. A. Stern, S. Harrington, A. E. Lita, T. Gerrits, I. Vayshenker, B. Baek, M. D. Shaw, R. P. Mirin, *et al.*, "Detecting single infrared photons with 93% system efficiency," *Nature Photonics*, vol. 7, no. 3, pp. 210–214, 2013.

[127] F. Marsili, F. Bellei, F. Najafi, A. E. Dane, E. A. Dauler, R. J. Molnar, and K. K. Berggren, "Efficient single photon detection from 500 nm to 5 µm wavelength," *Nano letters*, vol. 12, no. 9, pp. 4799–4804, 2012.

[128] "Methane, IR Spectrum." https://webbook.nist.gov/cgi/cbook.cgi?ID=C74828&Type=IR-SPEC&Index=1#IR-SPEC [Date Last Accessed 05/02/2025].

[129] M. Vollmer and K. P. Möllmann, *Infrared thermal imaging: Fundamentals, research and applications*. Wiley-VCH, 2017.

[130] A. Grisard, N. Treps, L. Morvan, R. Garioud, R. Demur, E. Lallier, C. Fabre, and L. Leviandier, "Near-infrared to visible upconversion imaging using a broadband pump laser," *Optics Express*, vol. 26, no. 10, pp. 1133–1144, 2018.

[131] P. Rehain, Y. M. Sua, S. Zhu, I. Dickson, B. Muthuswamy, J. Ramanathan, A. Shahverdi, and Y.-P. Huang, "Noise-tolerant single photon sensitive three-dimensional imager," *Nature communications*, vol. 11, no. 1, p. 921, 2020.

[132] Y. Chen, C. Jiang, Y. Liu, H. Su, X. Hu, and Y. Pan, "A Compact Upconversion Single-Photon Imager for Full-Range and Accurate 3-D Imaging," *IEEE Transactions on Instrumentation and Measurement*, vol. 72, pp. 1–9, 2023.

[133] B. Wang, M.-Y. Zheng, J.-J. Han, X. Huang, X.-P. Xie, F. Xu, Q. Zhang, and J.-W. Pan, "Non-line-of-sight imaging with picosecond temporal resolution," *Physical Review Letters*, vol. 127, no. 5, p. 053602, 2021.

[134] S. Zhu, Y. M. Sua, T. Bu, and Y.-P. Huang, "Compressive non-line-of-sight imaging with deep learning," *Physical Review Applied*, vol. 19, no. 3, p. 034090, 2023.

[135] R. Smith, B. Ndagano, G. Redonnet-Brown, A. Weaver, A. Astill, H. White, C. Gawith, and L. McKnight, "Single-photon infrared waveguide-based upconversion imaging," in *Electro-optical and Infrared Systems: Technology and Applications XIX*, vol. 12271, pp. 7–11, SPIE, 2022.

[136] I. Morland, R. Smith, J. Thomas, K. Pandiyan, C. Gawith, and L. McKnight, "Mid-infrared imaging and ranging with single-photon detectors using efficient upconversion in PPLN waveguides," in *Electro-Optical and Infrared Systems: Technology and Applications XXI*, vol. 13200, p. 132000H, SPIE, 2024.

[137] H. Kamada, M. Asobe, T. Honjo, H. Takesue, Y. Tokura, Y. Nishida, O. Tadanaga, and H. Miyazawa, "Efficient and low-noise single-photon detection in 1550 nm communication band by frequency upconversion in periodically poled $LiNbO_3$ waveguides," *Optics letters*, vol. 33, no. 7, pp. 639–641, 2008.

[138] J. S. Pelc, L. Ma, C. Phillips, Q. Zhang, C. Langrock, O. Slattery, X. Tang, and M. M. Fejer, "Long-wavelength-pumped upconversion single-photon detector at 1550nm: performance and noise analysis," *Optics Express*, vol. 19, no. 22, pp. 21445–21456, 2011.

[139] J. S. Pelc, C. Langrock, Q. Zhang, and M. M. Fejer, "Influence of domain disorder on parametric noise in quasi-phase-matched quantum frequency converters," *Optics letters*, vol. 35, no. 16, pp. 2804–2806, 2010.